Correlations of neutron star properties with the parameters of nuclear matter equation of state

By

NAOSAD ALAM

PHYS05201204007

Saha Institute of Nuclear Physics

A thesis submitted to the

Board of Studies in Physical Sciences

In partial fulfillment of requirements

For the Degree of

DOCTOR OF PHILOSOPHY

of

HOMI BHABHA NATIONAL INSTITUTE

November, 2017

Homi Bhabha National Institute

Recommendations of the Viva Voce Board

As members of the Viva Voce Board, we certify that we have read the dissertation prepared by **NAOSAD ALAM** entitled " **Correlations of neutron star properties with the parameters of nuclear matter equation of state** " and recommend that it maybe accepted as fulfilling the dissertation requirement for the Degree of Doctor of Philosophy.

Munshi ______ Date: 23/01/2018
Chair - Prof. Munshi Golam Mustafa

Bijay Agrawal ______ Date: 23.1.2018
Guide/Convener - Prof. Bijay Kumar Agrawal

Debades Bandyopadhyay ______ Date: 23.1.2018
Member 1 - Prof. Debades Bandyopadhyay

Maitreyee Saha Sarkar ______ Date: 23/1/18
Member 2 - Prof. Maitreyee Saha Sarkar

Subrata Pal ______ Date: January 23, 2018
External Examiner - Prof. Subrata Pal

Final approval and acceptance of this dissertation is contingent upon the candidate's submission of the final copies of the dissertation to HBNI.

I hereby certify that I have read this dissertation prepared under my direction and recommend that it may be accepted as fulfilling the dissertation requirement.

Date: 23/1/18

Place: Kolkata

Guide: Bijay Agrawal ______
Prof. Bijay Kumar Agrawal

STATEMENT BY AUTHOR

This dissertation has been submitted in partial fulfillment of requirements for an advanced degree at Homi Bhabha National Institute (HBNI) and is deposited in the Library to be made available to borrowers under rules of the HBNI.

Brief quotations from this dissertation are allowable without special permission, provided that accurate acknowledgement of source is made. Requests for permission for extended quotation from or reproduction of this manuscript in whole or in part may be granted by the Competent Authority of HBNI when in his or her judgment the proposed use of the material is in the interests of scholarship. In all other instances, however, permission must be obtained from the author.

Naosad Alam

DECLARATION

I, hereby declare that the investigation presented in the thesis has been carried out by me. The work is original and has not been submitted earlier as a whole or in part for a degree / diploma at this or any other Institution / University.

Naosad Alam

List of Publications (included in this thesis)

Journal

1. "Warm unstable asymmetric nuclear matter: Critical properties and the density dependence of the symmetry energy."
   N. Alam, H. Pais, C. Providência and B. K. Agrawal
   Phys. Rev. C 95, 055808 (2017), [arXiv:1705.02096 [nucl-th]].

2. "Strong correlations of neutron star radii with the slopes of nuclear matter incompressibility and symmetry energy at saturation."
   N. Alam, B. K. Agrawal, M. Fortin, H. Pais, C. Providência, Ad. R. Raduta, and A. Sulaksono
   Phys. Rev. C 94, 052801(R) (2016), [arXiv:1610.06344 [nucl-th]].

3. "Diversity of neutron star properties at the fixed neutron-skin thickness of ^{208}Pb."
   N. Alam, A. Sulaksono and B. K. Agrawal
   Phys Rev. C 92, 015804 (2015), [arXiv:1507.00837 [nucl-th]].

4. "Core-crust transition properties of neutron stars within systematically varied extended relativistic mean-field model."
   A. Sulaksono, Naosad Alam and B. K. Agrawal
   Int. J. Mod. Phys. E 23, 1450072 (2014), [arXiv:1411.0427 [nucl-th]].

Chapters in books and lectures notes : N. A.

Other Publications:

a. Conference/Symposium

1. "Emergence of new correlations between neutron star radii and nuclear matter properties."
   N. Alam, B. K. Agrawal, H. Pais, C. Providência and A. Sulaksono
   Proceedings of the DAE-BRNS Symp. on Nucl. Phys 61, 900, (2016)
2. "Effects of isovector cross-couplings on the properties of neutron stars."
   N. Alam, A. Sulaksono and B. K. Agrawal
   Proceedings of the DAE-BRNS Symp. on Nucl. Phys 60, 856, (2015)
3. "Probing the equation of state beyond the saturation density."
   N. Alam and B. K. Agrawal
   Proceedings of the DAE Symp. on Nucl. Phys 59, 820, (2014)

List of Publications (not included in this thesis)

Journal

1. "Equation of state of nuclear matter from empirical constraints."
   N. Alam, B. K. Agrawal, J. N. De, S.K. Samaddar and G. Colo
   Phys Rev. C 90, 054317 (2014), [arXiv:1411.0404 [nucl-th]].

Naosad Alam

DEDICATIONS

Dedicated to my family.

ACKNOWLEDGEMENTS

First of all, I would like to express my deepest gratitude to my supervisor Prof. Bijay Kumar Agrawal who has introduced me to the amazing world of neutron stars. I greatly appreciate him for his tireless support, constant encouragement and extraordinary mentorship throughout my PhD tenure. Our both academic and non-academic discussions over the years have been of great value to me. Without his ever present guidance, this work would not have been a reality.

I would like to sincerely thank my collaborators, Prof. Constança Providência, Dr. Helena Pais, Dr. Morgane Fortin, Prof. Anto Sulaksono, Prof. J. N. De and Prof. S.K. Samaddar, who have contributed in many different ways to the progress of this work. I am very grateful to them for their immense help and extremely valuable advices. I have enjoyed discussing and learned a lot from them. Prof. C. Providência has been a wonderful host during my visit at the University of Coimbra, Portugal, where the work related to the last chapter has been initiated. I would like to thank her for the nice hospitality. Special thanks also go to Dr. H. Pais and Dr. M. Fortin for the good times we had together during the visit.

I am also indebted to the members of my doctoral committee, Prof. Munshi Golam Mustafa , Prof. Debades Bandyopadhyay and Prof. Maitreyee Saha Sarkar for their encouraging words and thoughtful criticism.

I must thank Mrs. Tanuja Agrawal for the help with graph plotting software and preparing manuscript during my initial years in research.

A lot of thanks also goes to my friends, seniors, and juniors of Theory and APC division, as well as my other batchmates in the institute for many interesting conversations, valuable discussions, and fun experiences.

I thank all the members of faculty and staff of Theory Division for their support throughout these long five years.

Moreover, the financial support from Department of Atomic Energy is also gratefully acknowledged.

Last but definitely not the least, I want to thank my family for their unconditional support, love and patience.

Contents

Synopsis xv

List of Figures xix

List of Tables xxv

1 Introduction 1

1.1 Ordinary Star to Neutron Star . . . 2
1.2 History and Discovery . . . 4
1.3 Neutron Star Interior . . . 4
1.4 Equation of State and Neutron Star . . . 6
1.5 Correlations: Nuclear matter EoS and Neutron Star . . . 10
1.6 Organization of the Thesis . . . 13

2 Models for Neutron Star and Nuclear Matter 15

2.1 Stellar Structure equations . . . 16
2.2 EoS for Neutron Star . . . 23
  2.2.1 Relativistic Mean Field theory . . . 24
  2.2.2 Skyrme-Hartree-Fock theory . . . 30
2.3 Core-crust transition . . . 33
  2.3.1 Thermodynamical method . . . 33
  2.3.2 RRPA method . . . 34
  2.3.3 Spinodal instability and Critical parameters . . . 37

3 Core-crust transition properties and nuclear symmetry energy 41

3.1 Introduction 41

3.2 Systematically varied ERMF parameterizations 42

3.3 Results for Core-crust transition properties 44

3.4 Conclusions 54

4 Influence of nuclear symmetry energy on various neutron star properties 57

4.1 Introduction 57

4.2 Model parameters 59

4.3 Neutron-skin thickness and Neutron Stars properties 64

4.4 Conclusions 74

5 Correlations of EoS parameters with neutron star radii 77

5.1 Introduction 77

5.2 Nuclear models 78

5.3 Neutron star EoSs and Mass-radius results 80

5.4 Correlation results and Discussion 82

5.5 Conclusions 89

6 Warm asymmetric dilute matter and critical parameters 91

6.1 Introduction 91

6.2 Results 93

    6.2.1 Models 93

    6.2.2 Spinodal sections and Critical points 97

6.3 Conclusions 107

7 Summary and Conclusions 111

Bibliography 117

Synopsis

Neutron stars are born after the death of an ordinary star. An ordinary star undergoes gravitational collapse when it runs out of nuclear fuel. The process of collapse continues through several stages and ultimately a compact staller object like a white dwarf, a neutron star or a black hole is formed. The nature of compact object formed depends on the initial mass of the ordinary star. For instance, neutron stars are believed to be the endpoints of stellar evolution of massive stars ($M \gtrsim 8M_\odot$). Neutron star observed are as massive as $2M_\odot$ and the radii expected to be 10-15 km with central density to be $\sim 10^{15}$ gm/cm^3 [1, 2] which is a few times the normal nuclear density . Such dense objects are predominantly composed of neutrons along with small fractions of protons, electrons and muons to maintain the beta equilibrium and charge neutrality . However, the existence of exotic degrees of freedom like hyperons, bose condensates, and deconfined quark matter at the center can not be ruled out [3–9]. The presence of these exotic phases soften the equation of state (EoS) which reduces the maximum mass [10–17]. Recently, the observations of $\sim 2M_\odot$ neutron stars [18, 19] lead to a challenging problem whether such massive neutron star can have exotic components in the core region.

The knowledge of EoS for neutron star matter over a wide range of densities is essential to obtained the bulk properties of neutron star, e.g., mass, radius, moment of inertia, tidal deformability etc. [7, 20–23]. The EoS for the neutron star matter composed of neutrons, protons, electrons and muons readily satisfy the observational constrain of $2M_\odot$. In this thesis, we have concentrated on such EoSs. The nucleonic part of a EoS can be expanded around the saturation density in terms of various nuclear constants, like, nuclear incompressibility coefficient, symmetry energy and their slopes at that density [7, 24, 25]. The incompressibility coefficient and its slope govern EoS for symmetric nuclear matter, whereas one requires, in addition, the knowledge of symmetry energy and its slope in order to determine EoS for asymmetric nuclear matter. Since, neutron star matter is highly asymmetric, the knowledge of various symmetry energy elements is indispensable. The various nuclear constants or the key parameters of the EoS which characterize the properties of infinite nuclear matter are not directly accessible from terrestrial laboratory experiment. One can only realize them through their correlations with various finite nuclei and neutron star observables.

In recent years, a substantial amount of work has been done to investigate such correlations. For instance, the neutron skin thickness in heavy nucleus is found to be well correlated with the slope of symmetry energy [26–29]. However, the accurate measurement of neutron skin thickness even in a single heavy nucleus like ^{208}Pb is still awaited. In Refs. [30, 31], a strong correlation between the centroid of the giant monopole resonance (GMR) energy and the slope of nuclear incompressibility at sub-saturation density ($\rho \simeq 0.11$ fm^{-3}) is found. The slopes of nuclear matter incompressibility and symmetry energy coefficients are known only with in large uncertainties. Some preliminary investigations to find possible correlation of neutron star radii with the EoS parameters or the nuclear constants are also done [32, 33]. These correlations exhibit model dependence which does not allow one to draw a clear conclusion.

In this dissertation, our main focus is to explore the connection between the key EoS parameters and the neutron star properties in some detail. These neutron star properties may be both the crustal properties like crust-core transition density and the bulk properties like mass, radius, moments of inertia, tidal deformability etc.

We also investigate the sensitivity of critical parameters of hot asymmetric nuclear matter to the density dependence of symmetry energy. These critical parameters are vital in study of core-collapse supernova.

We have studied the dependence of the core-crust transition properties on various symmetry energy elements [34]. Three different families of systematically varied extended relativistic mean field (RMF) model [35–37] have been used for this study. Within each families several interactions are build, which have wide variations in the symmetry energy behaviour. The core-crust transition density is found to be strongly correlated, in a model independent manner, with the symmetry energy slope parameter evaluated at the saturation density. The pressure at the transition point dose not show any meaningful correlations with the symmetry energy parameters at the saturation density. At best, pressure at the transition point is correlated with the linear combination of symmetry energy slope and curvature parameters evaluated at some sub-saturation density.

We have studied the correlations of different neutron stars properties with the neutron skin thickness in heavy nucleus [38], since, the neutron skin thickness is an observable strongly correlated to the slope of symmetry energy. Two different families of RMF model corresponding to different nonlinear cross-coupling terms in the isovector part of the effective Lagrangian density have been constructed for these study. The neutron-star properties used for this analysis are core-crust transition density, radius and red shift at canonical mass, tidal deformability parameter, and threshold mass required for the enhanced cooling through the direct Urca process. Most of these neutron-star properties considered are showing strong dependence on the neutron skin thickness. We also demonstrate that some variations in the properties of neutron star, in particular at a smaller skin thickness, can be accounted by including various cross coupling terms and the coupling of delta mesons to the nucleons.

Most of the correlation paradigms existing between the properties of neutron star and the key EoS parameters manifest some model dependence. We have searched for the model independent correlations of neutron star properties with various key parameters of the EoS for a wide range of neutron star masses [25]. We have examined the correlations of neutron star radii of different masses with the key nuclear matter EoS parameter using a set of 44 models which includes non-relativistic mean field model based on Skyrme-type effective forces, relativistic mean field models and the models based on realistic interactions. Our investigation shows the existence of a strong correlation of the neutron star radii with the linear combination of the slopes of the nuclear matter incompressibility and the symmetry energy coefficients at the saturation density. These strong correlations are found to be almost independent of the neutron star masses. It may be reminded that the slopes of incompressibility and symmetry energy coefficients characterize the isoscalar and isovector parts of the EoS, respectively. The correlations of neutron star properties with linear combination of isoscalar and isovector properties of nuclear matter have never been considered earlier. Such correlations are shown to stem from the empirical relation existing between the star radius and the pressure at a nucleonic density between one and two times saturation density.

The sensitivity of critical parameters, in hot asymmetric nuclear matter, to the density dependence of symmetry energy is also examined [39]. The critical densities and proton fractions are more sensitive to the symmetry energy slope parameter at temperatures much below its critical value T_c. The spread in the critical proton fraction at a given symmetry energy slope parameter is noticeably larger near T_c , indicating that the equation of state of warm asymmetric nuclear matter at sub-saturation densities is not sufficiently constrained. The distillation effects are sensitive to the density dependence of the symmetry energy at low temperatures which tend to wash out with increasing temperature.

List of Figures

1.1 Schematic diagram for different layers composing a neutron star. . . . 5

1.2 The correlation coefficient between the neutron skin thickness of ^{208}Pb and several neutron star properties obtained in covariance analysis (figure from Ref. [68]). 11

1.3 Radii of neutron star as a function of symmetry energy slope L and incompressibility coefficient K for different masses obtained using a representative set of relativistic and non-relativistic models (figure from Ref. [33]). 12

3.1 Plots for the EoSs for the β-equilibrated matter obtained using the NL3, FSU, TM1 and GM1 parameterizations of the RMF model (lower panel). The filled circles represent core-crust transition density ρ_t and the corresponding pressure P_t calculated using RPA method. For the sake of comparison, the values of ρ_t and P_t obtained using thermo-dynamical (filled triangles) and dynamical methods(filled squares) of Ref. [70] are also shown. The P_t as a function of $L_1 - 0.343K_{\text{sym},1}$ are plotted in the upper panel, where, L_1 and $K_{\text{sym},1}$ represent the values of values of $L(\rho)$ and $K_{\text{sym}}(\rho)$ at $\rho = 0.01$ fm^{-3}, respectively. The dash line is taken from Ref. [70]. 45

3.2 The density dependence of the symmetry energy coefficient $S(\rho)$ for various ERMF models (left panel) and the variance Δ calculated using Eq. (3.5) (right panel). The labels F1, F2 and F3 represent three different families of the ERMF models, whereas, FA correspond to the results obtained by combining all the three families. In the inset, the high density behaviour of $S(\rho)$ are plotted for some selected forces from the F1,F2 and F3 families. 46

3.3 Plots for the EoSs for the β-equilibrated matter in terms of pressure verses density for the three different families of the ERMF model: F1 (red), F2 (blue) and F3 (green). The solid symbols mark the values of transition density ρ_t and the corresponding pressure P_t calculated within the RPA method. For the clarity, the results for only three forces for each of the families are plotted: BSR1, BSR8, BSR15 (dotted), BSR4, BSR11, BSR18 (dashed) and BSR7, BSR14, BSR21 (solid) lines (see text for details). 48

3.4 Plots for the ρ_t for neutron star matter as a function of symmetry energy J_0 (left panel) and its slope parameter L_0 (right panel) for 3 different families of the ERMF models. 49

3.5 Plots for the P_t, for neutron star matter, as a function of J_0 (left panel) and L_0 (right panel) for 3 different families of the ERMF models. . . 49

3.6 The correlation coefficients for the pressure P_t with $L(\rho)$ (lower panel), $K_{\text{sym}}(\rho)$ (middle panel) and the linear combination $L(\rho) - \alpha K_{\text{sym}}(\rho)$ (upper panel) as a function of the density for 3 different families of the ERMF models. 50

3.7 Plots for the pressure, P_t, at the transition density as a function of $K_{\mathrm{sym},1}$ (left panel) and $L_{09} - 1.31K_{\mathrm{sym},09}$ (right panel) for 3 different families of the ERMF models. 52

3.8 Plots for the ρ_t and P_t (left panel) as a function of J_1 and P_t verses ρ_t (right panel) that obtained using BSR1, FSU and NL3 type functional for the RMF model. The value of J_1 is varied at fixed $J_0 = 32.6$ MeV. 52

3.9 Same as that of 3.8, but, J_0 is varied at fixed $J_1 = 28.7$ MeV. 52

4.1 Colour coded contours in the $g_\delta - \eta_\rho$(left panel) and $g_\delta - \eta_{2\rho}$(right panel) planes corresponding to the F_ρ and $F_{2\rho}$ families, respectively. The value of g_ρ are colour coded according to the scale one the right side. 59

4.2 Same as Fig. 4.1, but, for the symmetry energy at the saturation density ($J_0 = S(\rho_0)$) (left panel) and the neutron-skin thickness Δr_{np} in the ^{208}Pb nucleus (right panel) fixed along the contour. The values of J_0 are in MeV. 61

4.3 The density dependence of symmetry energy $S(\rho)$ for some representative cases of F_ρ and $F_{2\rho}$ families of the models. The labels SET1 and SET2 correspond to the two different parameterizations for the F_ρ family, whereas, the SET3 and SET4 correspond to the $F_{2\rho}$ family. The SET1 and SET3 are associated with $\Delta r_{\mathrm{np}} = 0.22$fm and the SET2 and SET4 yield $\Delta r_{\mathrm{np}} = 0.15$fm (see also Tables 4.1 and 4.2). . 62

4.4 The variations of symmetry energy slope parameter L_0 with neutron-skin thickness Δr_{np} in the ^{208}Pb nucleus for the F_ρ and $F_{2\rho}$ families of models. The solid and hollow symbols represent the results obtained with ($g_\delta \neq 0$) and with ($g_\delta = 0$), respectively. 65

4.5 The variation of core-crust transition density and the corresponding pressure with the neutron-skin thickness $\Delta r_{\rm np}$ in ^{208}Pb nucleus for the F_ρ and $F_{2\rho}$ families of the extended RMF models. 66

4.6 The mass-radius relationship for the F_ρ and $F_{2\rho}$ families of the models. The solid squares represent the masses and the corresponding radii for the neutron stars with the central density to be $3\rho_0$. 67

4.7 Plots for the radius $R_{1.4}$ for the neutron stars with the canonical mass $1.4M_\odot$ (left panel) and the corresponding red shift (right panel) as a function of $\Delta r_{\rm np}$ in the ^{208}Pb nucleus obtained for the F_ρ and $F_{2\rho}$ families of models. 69

4.8 The dependence of the threshold neutron star mass M_{DU} on the neutron-skin thickness in ^{208}Pb nucleus. The neutron stars with mass equal to or larger than M_{DU} undergo enhanced cooling through direct Urca process for the cooling. 70

4.9 Variations in the tidal polarizability parameter λ with the neutron star mass for the different parameterizations of F_ρ and $F_{2\rho}$ families corresponding to neutron-skin thickness $\Delta r_{\rm np} = 0.15$ fm in the ^{208}Pb nucleus. 73

5.1 Neutron star mass in $M_\odot$ as a function of the radius in km (left) and central density in fm^{-3} (right) for a representative set of RMF (blue) and Skyrme (red) models, and microscopic (green) calculations. . . . 80

5.2 Radii $R_{1.0}$ (left) and $R_{1.4}$ (right) of a 1.0 and $1.4M_\odot$ neutron star versus the EoS parameters K_0, M_0 and L_0, obtained using our sets of RMF (blue triangles) and Skyrme (red diamonds) models, together with the BHF and the APR (green stars) calculations. 83

5.3 Neutron star radii $R_{1.0}$ (left) and $R_{1.4}$ (right) versus the linear correlations $K_0+\alpha L_0$ (top) and $M_0+\beta L_0$ (bottom), using a set of RMF (blue triangles), Skyrme (red diamonds), and BHF+APR (green stars) calculations. 85

5.4 Correlation coefficients between the neutron star radii and several EoS parameters as a function of the neutron star mass. The EoS parameters 'b' denote K_0, L_0, and the linear combination $K_0 + \alpha L_0$ in the top panel, and M_0, L_0, and $M_0 + \beta L_0$ in the bottom panel. . . 86

5.5 M_0 as a function of $R_{1.4}$ for L_0 = 40, 60 and 80 MeV, as obtained from the multiple linear regression. The gray shaded region indicates the constraint on M_0 derived in Ref. [170]. 88

6.1 Difference between the neutron matter pressure for the F$_\rho$ (left panels) and F$_{2\rho}$ (right panels) families and the average pressure obtained from a chiral EFT [210] (top) and Monte Carlo [211] (bottom) calculations, in units of the pressure uncertainty at each density, $\sigma = \Delta P$. The gray bands represent the calculation uncertainty (light) and twice this uncertainty (dark). 93

6.2 Symmetric matter pressure as a function of the density for the NL3 (solid), TM1 (dashed) , and BKA22 (dash-dotted) models. The colored bands are the experimental results obtained from collective flow data in heavy-ion collisions [47] (light gray) and from the KaoS experiment [48, 213] (dark gray). 95

6.3 Symmetry energy as a function of baryon density for the F$_\rho$1, F$_\rho$7, F$_{2\rho}$1, F$_{2\rho}$7 (solid), NL3, NL3$\sigma\rho$6, NL3$\omega\rho$6 (dashed), and TM1, TM1$\sigma\rho$6, TM1$\omega\rho$6 (dash-dotted) models. The DD2 (green) and DDME2 (orange) models are also represented for comparison. 96

6.4 Spinodal sections on the (ρ_n, ρ_p) plane for $F_\rho 1$ (top left), $F_\rho 7$ (top right), $F_{2\rho}1$ (bottom left) and $F_{2\rho}7$ (bottom right) models at $T = 0, 6, 12$ and 14 MeV. 97

6.5 Spinodal sections on the (ρ_n, ρ_p) plane for $F_\rho 1$, $F_\rho 7$, $F_{2\rho}1$ and $F_{2\rho}7$ models at $T = 0$ (top left), 6 (top right), 12 (bottom left) and 14 (bottom right) MeV. 98

6.6 Critical proton fraction, Y_{pc}, as a function of L_0 for several temperatures, and for all the models considered in this study. The right panel shows the results for $T = 0$ and 6 MeV only. 99

6.7 Critical density, ρ_c, as a function of L_0, for several temperatures, and for all the models considered in this study. 100

6.8 The fluctuations $\delta\rho_p^-/\delta\rho_n^-$ at $T = 0$ MeV as a function of the proton fraction Y_P (top panels) with $\rho = 0.06$ fm^{-3}, and as a function of ρ/ρ_0 (bottom panels), with $Y_p = 0.30$ (solid), and 0.05 (dashed). The calculations shown are for the models F_ρ and $F_{2\rho}$ (left), $NL3\omega\rho$ and $NL3\sigma\rho$ (middle) and $TM1\omega\rho$ and $TM1\sigma\rho$ (right panels). 104

6.9 The fluctuations $\delta\rho_p^-/\delta\rho_n^-$ as a function of the proton fraction, Y_P, for a fixed baryon density of $\rho = 0.04$ fm^{-3} at $T = 0$ MeV (top), $T = 6$ MeV (middle), and $T = 12$ MeV (bottom panels), for the F$_{x\rho}$ (left), NL3$x\rho$ (middle), and TM1$x\rho$ (right) families. 105

6.10 The fluctuations $\delta\rho_p^-/\delta\rho_n^-$ as a function of ρ/ρ_0, for a fixed proton fraction of $Y_p = 0.3$, at $T = 0$ MeV (top), $T = 6$ MeV (middle), and $T = 12$ MeV (bottom panels), for the F$_{x\rho}$ (left), NL3$x\rho$ (middle), and TM1$x\rho$ (right) families. 106

List of Tables

3.1 The values of correlation coefficients $C(A, B)$ with A and B being the core-crust transition density ρ_t, corresponding pressure P_t and various symmetry energy parameters at the saturation density. 53

3.2 Values for the various correlation coefficients obtained by varying J_0 or J_1 within a single model. Three different models, BSR1, FSU and NL3, are considered. The values of J_0 is varied by fixing $J_1 =$ 28.7 MeV , while, J_1 is varied by fixing $J_0 = 32.6$ MeV. The values of correlation coefficients obtained by combining the results from all the three models are presented in the last column. 54

4.1 The parameters of the isovector part of the Lagrangian density for some representative sets for the F_ρ and $F_{2\rho}$ families of models. In the bottom part, the values for the symmetry energy coefficient at the saturation density J_0, symmetry energy slope parameter L_0, effective mass for the protons and neutrons and their differences are also presented. All these quantities are in MeV. 60

4.2 The values of the total binding energy (E) in MeV, charge radii (r_c), neutron radii (r_n) and neutron-skin thickness $\Delta r_{\rm np}$ in fm for a few asymmetric spherical nuclei obtained for SET1 - SET4 parameters. Experimental values of their binding energy and charge radii are also presented. 60

4.3 Properties of neutron stars and the neutron-skin thickness in the ^{208}Pb nucleus obtained for SET1 -SET4 parameters. The values of tidal polarizability parameter $\lambda_{1.4}$, listed in the last row, correspond to the neutron star with mass $1.4M_{\odot}$. 73

5.1 EOS parameters calculated at saturation density for our representative sets of RMF, Skyrme, and microscopic calculations. The EOS parameters are the saturation density ρ_0 (in fm^{-3}), the binding energy per nucleon e_0, the nuclear matter incompressibility coefficient K_0, its skewness Q_0, the slope M_0, the symmetry energy coefficient J_0, its slope L_0, and the curvature parameter $K_{\rm sym,0}$ (all in MeV). . . 79

5.2 Maximum masses, $M_{\rm NS}^{\rm max}$, and radii, R_x, of neutron stars, for the RMF, Skyrme, and microscopic calculations used in this study. R_x denotes neutron star radii (in km) for a mass x (in $M_{\odot}$). 81

5.3 Correlation coefficients between the neutron star radii and the different EoS parameters obtained for a representative set of RMF, Skyrme and microscopic calculations. The EoS parameters are the nuclear matter incompressibility coefficient K_0, its skewness Q_0, and slope M_0, the symmetry energy coefficient J_0, its slope L_0, and curvature $K_{\rm sym,0}$, and the parameter $K_{\tau,0}$, calculated at the saturation density. R_x denotes the neutron star radius for a given mass x in units of $M_{\odot}$. 84

5.4 The correlation coefficients of neutron star radii with $K_0 + \alpha L_0$ and $M_0 + \beta L_0$, along with the values of α and β. 85

6.1 The values of the binding energy per particle (B/A), charge radii (r_c), neutron radii (r_n) and neutron skin thickness ($\Delta r_{\rm np}$) for ^{208}Pb nucleus along with the maximum mass (M_{max}) of neutron star and corresponding radius (R_{max}) obtained for some selected models. . . . 95

6.2 Critical temperatures, and their correspondent critical densities and pressures for all the models considered in this work. The proton fraction is 0.5. 99

6.3 Critical densities, ρ_c, and proton fractions, Y_{pc}, for different temperatures, and for all the models considered. The slope parameter L_0 and temperature T are in MeV. The critical density ρ_c is in fm^{-3}. 103

CHAPTER 1

Introduction

Neutron stars are one of the most interesting cosmic laboratories for the study of fundamental physics. They belong to a class of astrophysical objects known as compact stars. These compact stars have very small radius and a huge mass, which requires very high densities. Neutron stars have masses typically in the range of $\sim 1 - 2\mathrm{M}_{\odot}$ and radii $\sim 10 - 15$ km. As the name suggests, they are mainly composed of neutrons together with some small amount of protons and electrons, the composition of these constituent particles being determined by beta-stability and charge neutrality conditions. Normally, the densities in the central region of the neutron stars are a few times larger than that encountered in the center of a heavy nucleus which is $\rho_0 \sim 0.16$ fm^{-3} ($\simeq 2.7 \times 10^{14}$ g/cm^3). They are the densest known object in the universe which have an observable surface allowing astrophysicists to investigate many of their properties. In general, neutron stars are not only extreme with respect to their density and asymmetry, but, some of them also rotate very fast with a rotation period in the milli-second regime. These objects can also have huge magnetic fields ($B \sim 10^{15}$ Gauss) referred to as magnetars. Due to its extreme nature, a neutron star brings together all the four fundamental forces of nature: gravitational force, weak force, strong force and the electromagnetic force. Study of neutron star properties involves many areas of physics, like, nuclear physics, astrophysics, general relativity etc. If we look in terms of the length scale, it connects the physics of femtometer scale to the physics of kilometer scale. Therefore, the physics of neutron star is highly complex and mysterious, and it has been extensively researched since the last few decades.

1.1 Ordinary Star to Neutron Star

Ordinary stars are born from the gravitational collapse of dense regions within molecular clouds of interstellar matter. The gravitational collapse is triggered by density fluctuations in the interstellar clouds. Such stars are held up by thermal gradient pressure of the hot gas, which is created due to the nuclear energy generation in their central regions. A main sequence star spends its life by burning nuclear fuels, but when the star has exhausted all its nuclear fuel, the nuclear energy generation stops. In this situation, the gas pressure of the hot interior can not counterbalance the gravitational pull,therefore, the star expels most of its outer matter and the core of the star collapses to a dense stellar compact object. These compact objects are categorized into three different types: white dwarfs, neutron stars, and black holes.

The time evolution and ultimate fate of an ordinary star depend on the initial mass of the star. A main sequence star spends most of its life time in the burning of hydrogen to form helium. For low mass stars, the temperature in the core may not be sufficient to fuse helium into other heavier elements and the star ends its evolution as a helium white dwarf. However, there is no isolated helium white dwarf in today's universe, because, in low mass stars, the time spent in the nuclear burning process to exhaust the nuclear fuel is so long that it goes over the current age of the universe. For more massive stars, i.e. stars having masses up to a few solar masses, the nuclear burning process continues after formation of helium and it burns into carbon. The fusion process is faster in massive stars due to the high pressure at the centre of the star. In later stages, depending on the initial mass, the ignition process goes through the cycles of carbon, neon, oxygen and silicon burning, which produces other heavier elements. If the mass of the core does not exceed the Chandrasekhar mass limit (the maximum mass which can be held by electron degeneracy pressure $\sim 1.4\ \mathrm{M}_\odot$), the star ends its life as a white dwarf after the expulsion of the outer layer. The white dwarfs are supported by the electron degeneracy pressure and the composition of its core depends on how far the nuclear burning proceeds before reaching the stability against the gravitational collapse.

The stars with mass more than $M \gtrsim 8\mathrm{M}_\odot$ go through all the stages of nuclear burning up to the formation of iron, the most stable element in nature, beyond which nuclear fusion would be endothermic. When the mass of the iron core becomes bigger than the Chandrasekhar mass, electron degeneracy pressure can not support the gravitational pull and it starts collapsing. In this situation, the electrons are captured by protons and the matter becomes neutron rich. This inverse β-decay and the photo disintegration of iron group nuclei to alpha particles accelerate the process of collapse by removing the energy from the system. Finally, further compression of the star leads to the formation of a shock wave that ejects all the external layers leaving behind a proto-neutron star. In this process, a huge amount of energy is released creating a massive explosion known as core-collapse supernova. The newly born proto-neutron star is initially very hot with temperature larger than 10^{10} K. It then contracts and cools down via neutrino emission, and evolves to a neutron star. Unlike white dwarfs, the neutron stars are supported by the neutron degeneracy pressure. If mass of the progenitor star is very high, neutron degeneracy pressure can not hold the gravitational pull and it collapses to a black hole.

1.2 History and Discovery

The concept of a dense star was first introduced by Lev Landau a year before the discovery of the neutron by J. Chadwick in 1932 [2,40,41]. Two years later in 1934, Walter Baade and Fritz Zwicky first proposed that neutron stars are formed after a rapid release of a huge amount of energy in an event known as supernova explosion, and consisting mainly of neutrons [42].

In 1939, Oppenheimer and Volkoff constructed an equation of state of non interacting closely packed neutrons and calculated the maximum mass of neutron star to be $\sim 0.7\ \mathrm{M}_\odot$ [43]. But, the average mass of a neutron star is $\sim 1.4\ \mathrm{M}_\odot$, which indicates that there must be interactions between the neutrons. At that time it was believed that the observation of neutron stars would be extremely difficult, if at all possible, due to their tiny radii, and hence, low luminosities. Thus, the work with neutron stars was of lower priority.

However, in 1967, the first pulsar was detected by Jocelyn Bell, a graduate student supervised by Antony Hewish [44]. They observed a pulsating radio source with a period of around 1.377s. These pulsars were eventually realized as spinning neutron stars with magnetic fields of an order of magnitude of 10^{12} Gauss. The discovery of pulsars and their identification as spinning neutron stars led to a considerable interest in the physics of neutron stars.

1.3 Neutron Star Interior

Inside neutron stars, the matter density is highest at the centre and it decreases from the centre to the surface. Consequently, the phases and composition of matter are different at different regions of the star. Depending on its phase and composition, the theory describing matter and the behaviour of the corresponding equation of state

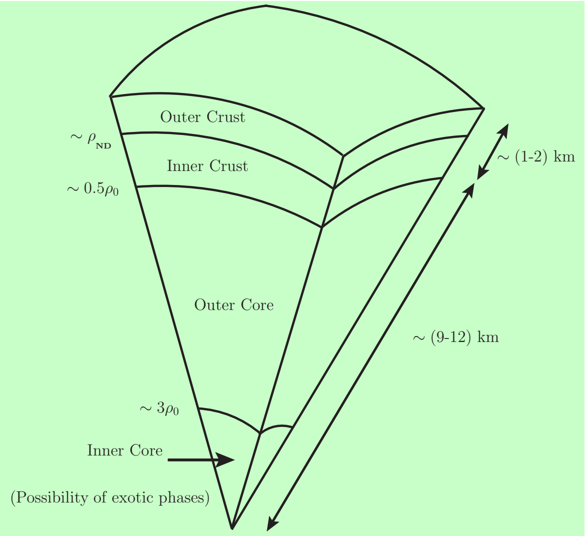

Figure 1.1: Schematic diagram for different layers composing a neutron star.

(EoS) are also different. Neutron star interior can be divided into four different regions (Fig. 1.1):

Outer crust

It is the outer part of the star. The density range of this region is from $\rho \sim 10^4$ g/cm^3 to $\rho_{\mathrm{ND}} \sim 4\times10^{11}$ g/cm^3 (neutron drip density). It is a solid region composed of heavy nuclei forming a Coulomb lattice embedded in a relativistic degenerate gas of electrons. The thickness of this layer is about several hundred meters. As the density increases, the energies of electrons become high enough for inverse beta decay, leading to increase in the neutron-rich nuclei via electron capture. However, such neutron-rich nuclei are unstable on earth environment.

Inner crust

The density range of the inner crust is from $\rho_{\mathrm{ND}} \sim 4 \times 10^{11}$ g/cm^3 to the core-crust interface density $\rho_t \simeq 1.3 \times 10^{14}$ g/cm^3 ($\sim 0.5\rho_0$). The accurate value of the core-crust interface density is model dependent. The matter describing this region of the crust consists of neutron-rich nuclei, degenerate relativistic electron gas and free degenerate neutrons. Close to core-crust interface, the nuclei can have complex non-spherical shapes known as “ nuclear pasta ”, however, the shapes also depend on the specific model.

Outer core

When the density is higher than the core-crust interface density, the matter inside the neutron star becomes uniform. The matter in this region consists of neutrons, protons, electrons, and muons. The composition of constituent particles is determined by charge neutrality and beta-equilibrium condition. The thickness of this part is ~ 10 km, which covers the maximum part of the star.

Inner core

The very centre part of the star. It is the most unknown region of a neutron star. There are many possibilities of composition within the inner core of neutron star. Different exotic phases like hyperons, Bose-Einstein condensate of mesons, quark matter etc. may exist at the central core. The physics of all of these exotic phases are very interesting, but none of them has been confirmed.

1.4 Equation of State and Neutron Star

Recent years have witnessed a great amount of research activity to accrue knowledge and understand the behaviour of dense nuclear matter for a wide range of densities and asymmetries. In this respect, neutron star, being extremely compact, has become one of the most essential tools and its properties are sensitive to the equation of state of cold asymmetric dense matter. Observational properties of neutron stars allow us to constrain the EoS of nuclear matter over a wide range of densities. For a given EoS, the bulk properties of neutron stars (such as mass, radius etc.) can be obtained theoretically from the solution to their structure equations. Then, by comparing these theoretical results to the observational data, one can obtain valuable information about the EoS.

Though the EoS of cold dense baryonic matter governs the bulk properties of neutron stars predominantly, its behaviour is not well understood for all densities and asymmetries. The EoS at a given density ρ and asymmetry δ can be decomposed, to a good approximation, into the EoS for symmetric nuclear matter $e(\rho, 0)$, and the density dependent symmetry energy $S(\rho)$ arising from the imbalance between neutrons and protons as

$$e(\rho, \delta) = e(\rho, 0) + S(\rho)\delta^2\,, \tag{1.1}$$

where $e(\rho, \delta)$ is the energy per nucleon at density $\rho = \rho_n + \rho_p$, and $\delta = (\rho_n - \rho_p)/\rho$ the asymmetry parameter, with ρ_n and ρ_p being the neutron and proton densities, respectively. The symmetry energy is given by

$$S(\rho) = \frac{1}{2}\left.\frac{d^2 e(\rho, \delta)}{d\delta^2}\right|_{\delta=0}. \tag{1.2}$$

The isoscalar part, $e(\rho, 0)$, can be expanded around the saturation density ρ_0 as

$$e(\rho, 0) = e(\rho_0) + \frac{K_0}{2}\left(\frac{\rho - \rho_0}{3\rho_0}\right)^2 + \frac{Q_0}{6}\left(\frac{\rho - \rho_0}{3\rho_0}\right)^3 + \mathcal{O}(4), \tag{1.3}$$

where the incompressibility K_0, the skewness coefficient Q_0, are defined as,

$$K_0 = 9\rho_0^2\left(\frac{\partial^2 e(\rho)}{\partial \rho^2}\right)_{\rho_0}, \tag{1.4}$$

and

$$Q_0 = 27\rho_0^3\left(\frac{\partial^3 e(\rho)}{\partial \rho^3}\right)_{\rho_0}. \tag{1.5}$$

In a similar way, the isovector part $S(\rho)$ can also be expanded as

$$S(\rho) = J_0 + L_0 \left(\frac{\rho - \rho_0}{3\rho_0}\right) + \frac{K_{sym,0}}{2}\left(\frac{\rho - \rho_0}{3\rho_0}\right)^2 + \mathcal{O}(3), \tag{1.6}$$

where $J_0 = S(\rho_0)$ is the symmetry energy coefficient. The slope L_0, and the curvature $K_{sym,0}$ of the symmetry energy are defined as [28]

$$L_0 = \quad 3\rho_0 \left(\frac{\partial S(\rho)}{\partial \rho}\right)_{\rho_0}, \tag{1.7}$$

and

$$K_{sym,0} = \quad 9\rho_0^2 \left(\frac{\partial^2 S(\rho)}{\partial \rho^2}\right)_{\rho_0}. \tag{1.8}$$

At saturation density, the slope of the incompressibility, M_0, and the symmetry incompressibility, $K_{\tau,0}$, can also be defined as [24]

$$M_0 = Q_0 + 12K_0\,, \tag{1.9}$$

$$K_{\tau,0} = K_{sym,0} - 6L_0 - \frac{Q_0}{K_0}L_0. \tag{1.10}$$

Behaviour of the EoS around the saturation density ρ_0 for the symmetric nuclear matter is reasonably known in terms of the empirical values for the energy per nucleon and incompressibility coefficient of the nuclear matter at ρ_0 extracted from the various bulk properties of the finite nuclei [45, 46]. The symmetry energy $S(\rho)$ is reasonably constrained only around the saturation density by the ground-state properties of finite nuclei. However, density dependence of $S(\rho)$ is poorly known, leading to a large uncertainty in the EoS for the asymmetric nuclear matter. The understanding of density dependence of the $S(\rho)$ is crucial as it controls the radii of neutron stars, the thicknesses of their crusts, the rate of cooling of neutron stars, and the properties of nuclei involved in r-process nucleosynthesis.

To probe the high density behaviour of the EoS, one needs to rely on the experimental data on the heavy-ion collisions and the various properties of highly dense objects. Collective flow and kaon productions in heavy-ion collisions experiments provides some reasonable constraints on the EoS for symmetric nuclear matter at supra-nuclear densities up to $4.5\rho_0$ [47–49]. But the EoS for asymmetric nuclear matter remains poorly constrained due to lack of knowledge of the density dependence of the nuclear symmetry energy. Several different observables such as π^-/π^+ ratio [50–52], neutron-proton differential collective flow [50], K^+/K^0 ratio [52, 53], the n/p ratio of squeezed-out nucleons [54], $t/^3\text{He}$ ratio [55, 56], Σ^-/Σ^+ ratio [57] have been suggested to probe the behaviour symmetry energy at supra-saturation densities. Some progress has been made along this direction. Nevertheless, knowledge of symmetry energy at high density is not yet conclusive. In fact, sometimes different investigations contradict each other. For example, the FOPI Collaboration at GSI, Darmstadt published a few years ago a complete set of pion data in heavy-ion collisions [58]. From analyzing the charge pion ratio with the Boltzmann-Uehling-Uhlenbeck (IBUU04) transport model [59, 60] a circumstantial evidence for a super-soft symmetry energy was reported [61]. However, an analysis of the same data using a version of the quantum molecular dynamics model gave an opposite conclusion [62]. More recent studies using the Boltzmann-Langevin approach [63] made a similar conclusion as in Ref. [61].

In exploring these uncertain properties of dense matter, compact objects like neutron stars also serve as astrophysical laboratories. The core-crust transition properties which affect the crust thickness of the neutron stars are governed by the low density behaviour of the EoS. The core region of the neutron stars are sensitive to the behaviour of the EoS at high densities. Therefore, the observable properties of neutron stars are expected to have good correlation with the important parameters connected to the EoS and the knowledge of the EoS can be extended by accurate determination of the EoS parameters through their correlations with the neutron star observable. The observations of neutron stars properties such as its maximum mass and radius, hence, provide good opportunities to gain deeper insight into the physics of dense matter EoS.

1.5 Correlations: Nuclear matter EoS and Neutron Star

Some investigations have already been done to study the correlation of different EoS parameters with the properties of finite nuclei and astrophysical observables. The neutron skin thickness in heavy nucleus is strongly correlated to the slope of symmetry energy at saturation density [64, 65]. But, such correlation can not constrain the symmetry energy slope parameter in a tighter bound as the neutron skin thickness is not yet precisely measured. Recently, E. Khan *et. al.* [30, 31] analyzed the correlation of the centroid of the giant monopole resonance (E_{GMR}) energy with the nuclear incompressibility and its slope. It was shown that the correlation of E_{GMR} with the slope of the incompressibility at sub-saturation density ($0.7\rho_0$) is well pronounced than that with the nuclear incompressibility at the saturation density ρ_0. Correlations among various bulk EoS parameters are also studied. For example, the correlation between saturation density and nuclear matter binding energy, commonly known as Coester line [66]. The relationship between finite nuclei spin-orbit splittings and Dirac effective mass of nucleon is shown in Ref. [67]. They found that such splittings are experimentally well reproduced if the range of $m*$ (the ratio between Dirac effective mass and rest mass of nucleon) is $0.58 \leqslant m* \leqslant 0.64$.

Preliminary calculations to analyze the correlations between EoS parameters and

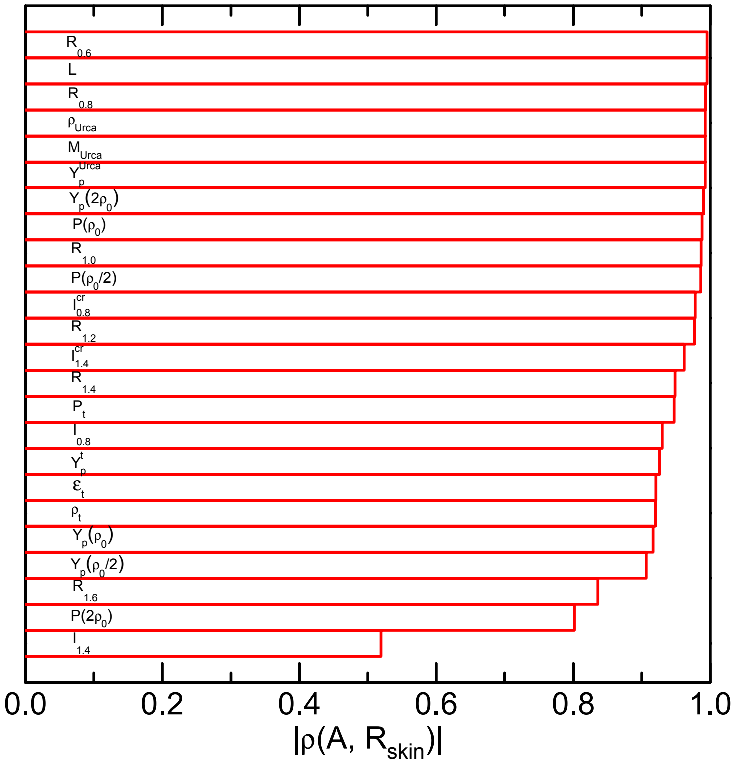

Figure 1.2: The correlation coefficient between the neutron skin thickness of ^{208}Pb and several neutron star properties obtained in covariance analysis (figure from Ref. [68]).

neutron star observables have also been performed. In Refs. [69, 70], a correlation analysis has been carried out to study the link between the core-crust transition properties and the isovector EoS parameters. It has been shown that the transition density ρ_t is mainly correlated with the symmetry energy slope L. The proton fraction at transition density is correlated with the symmetry energy and symmetry energy slope at saturation density and the correlation becomes even better with the same quantities evaluated at sub-saturation density $\rho = 0.1$ fm^{-3}. The transition pressure is found to be correlated with the linear combination of symmetry energy slope L and curvature K_{sym} at density $\rho = 0.1$ fm^{-3}. The correlation between the core-crust transition density and finite nuclei observable like neutron skin thickness of ^{208}Pb has also been established [71]. In Ref. [68], the authors have examined the correlation between the neutron skin thickness of ^{208}Pb and several neutron star properties using covariance analysis based on a single model. Strong correlations of

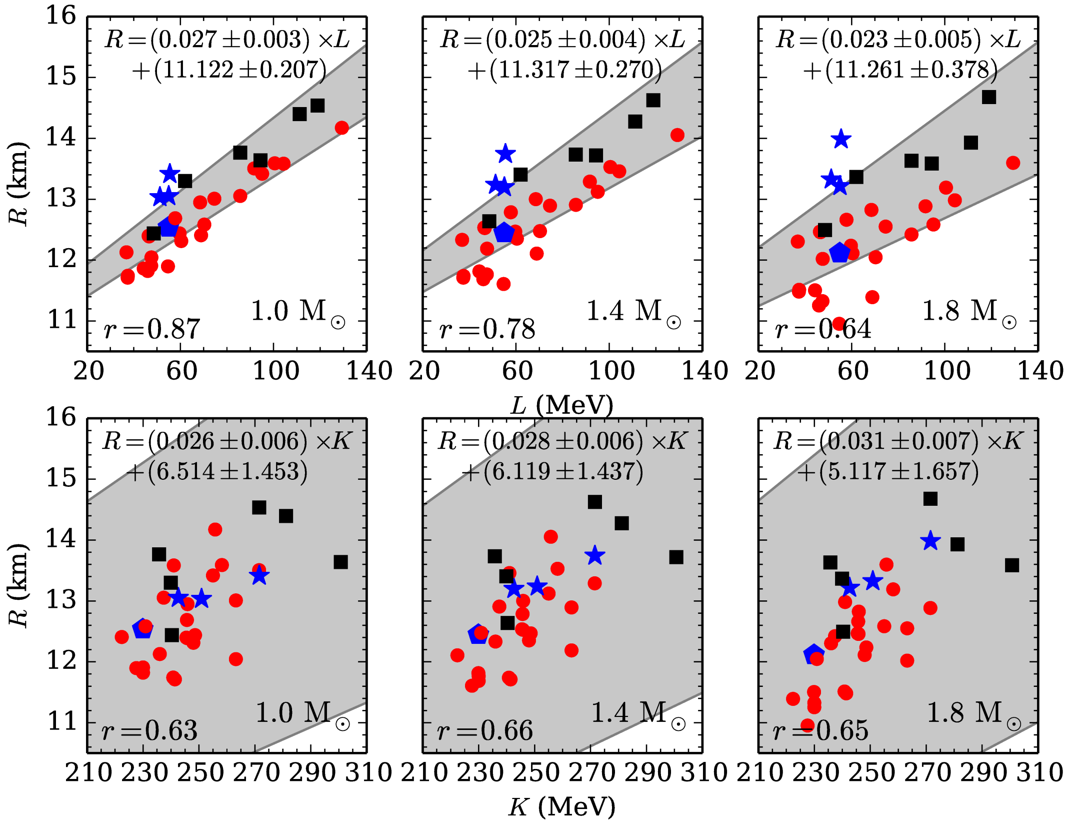

Figure 1.3: Radii of neutron star as a function of symmetry energy slope L and incompressibility coefficient K for different masses obtained using a representative set of relativistic and non-relativistic models (figure from Ref. [33]).

neutron skin thickness of ^{208}Pb with the radii, moment of inertia of low-mass neutron stars and the properties relevant to direct Urca process in neutron star have been found. Existence of strong correlations between the core-crust transition properties and neutron skin thickness in ^{208}Pb has also been reported in their work. Fig. 1.2 shows the correlation coefficients between various neutron star observables and the neutron skin thickness of ^{208}Pb obtained in their correlation analysis. Similar analysis to study the correlations between the radii of neutron stars with $L(\rho)$ as a function of density have been performed by Fattoyev *et. al.* [32]. This study also manifests a strong correlation between the neutron star radius and total $L(\rho)$ over a wide range of suprasaturation densities, but the correlation structures are found to be model dependent. Recently, correlations of neutron star radii with the symmetry energy slope parameter and the nuclear matter incompressibility coefficient have been examined using a large set of unified EoSs, based on Skyrme-type effective forces and relativistic mean field (RMF) models [33]. The results obtained for this correlation study are displayed in Fig. 1.3. The dependence of correlations on the neutron star mass is qualitatively similar to that obtained within the covariance analysis, but the correlations are, in general, somewhat weaker due to the interference of the other EoS parameters, which were kept fixed in the case of covariance analysis. All these investigations strongly motivate one for a rigorous analysis to pin down the existing universal and model independent correlations.

In this dissertation work, we would like to study the influence of the various bulk properties associated with the nuclear matter on some important properties of the neutron stars in a comprehensive manner. We investigate the correlations of various crustal and bulk properties of neutron stars with the key EoS parameters using representative sets of nuclear models which are commonly used in the literature for the description of neutron star matter. Although many experimental and theoretical efforts have been put into the determination of these key nuclear parameters, some of them are still very uncertain. On the other hand, there are several neutron star observables, e.g., radii, moment of inertia, which are also, in the present time, not measured precisely. Thus, these correlation studies, which provide the relationships among the observables, certainly help one to constrain the lesser known quantities from the knowledge of the other well known quantities.

1.6 Organization of the Thesis

The layout of this thesis is given below.

Brief overview of the theories of neutron star and nuclear matter EoS are given in chapter 2. The derivations of the stellar structure equations are discussed. We also review some selected nuclear models which are commonly used to calculate the

EoS for neutron star matter. We give a brief description of the methods which will be used to determine the core-crust transition density of neutron star and the critical parameters of hot asymmetric nuclear matter. In chapter 3, we investigate the correlation of crustal properties of neutron stars with several isovector key EoS parameters. We present results depicting the sensitivity of various neutron star properties to the density dependence of the symmetry energy in chapter 4. Correlations of neutron star radii with several isoscalar and isovector EoS parameters are discussed in chapter 5. In chapter 6, we explore the dependence of spinodal instabilities and critical parameters of hot asymmetric nuclear matter on the slope of symmetry energy. Finally, the summary and conclusions are presented in chapter 7.

CHAPTER 2

Models for Neutron Star and Nuclear Matter

The two most basic properties of a neutron star are its mass M and radius R. Several other important observables such as moment of inertia, minimum spin periods of rotation, surface red-shift, binding energy of a neutron star etc., are governed by these two observables. The mass and radius of a star can be obtained theoretically by solving its structure equations: the equation of hydrostatic equilibrium and the equation of mass of a spherical shell. Hydrostatic equilibrium describes the balance between gravity and internal pressure. The internal pressure is the thermal pressure for normal stars and the degeneracy pressure of fermions for white dwarfs and neutron stars. General relativistic treatment is needed for calculating the structure of superdense object like the neutron star. In this chapter, we discuss about the stellar structure equations in the framework of general relativity and the procedure to obtain mass and radius of a star by solving these equations. The important input for calculation of neutron star model is the equation of state (EoS) of matter inside the neutron star. We review some selective theoretical models which are commonly used for the calculation of EoS of neutron star matter. In addition, we review the methods which will be applied in our work for the calculation of crust-core transition density. We also discuss here the stability conditions of hot asymmetric nuclear matter.

2.1 Stellar Structure equations

The structure of the spherically symmetric static non rotating neutron star is determined by the Tolman-Oppenheimer-Volkoff (TOV) equations, the general relativistic equations of hydrostatic equilibrium. These TOV equations can be derived from solution to the Einstein's field equations by assuming the star to be made of perfect fluid i.e. non-viscous and stress free fluid. The general metric of such an object can be written as,

$$d\tau^2 = e^{2\nu(r)}dt^2 - e^{2\lambda(r)}dr^2 - r^2(d\theta + sin^2\theta d\phi^2) \ . \tag{2.1}$$

Einstein's field equation,

$$G^{\mu\nu} = \kappa T^{\mu\nu} + \Lambda g^{\mu\nu} \ , \tag{2.2}$$

where $G^{\mu\nu}$ is the Einstein curvature tensor, $T^{\mu\nu}$ represents the energy-momentum tensor, Λ is called cosmological constant and κ is a constant which will be determined later in this section. The value of cosmological constant Λ is very small, so one can neglect it in models of such compact objects. We can write the Einstein tensor in terms of the metric tensor $g^{\mu\nu}$, the Ricci tensor $R^{\mu\nu}$ and the Ricci scalar R as,

$$G^{\mu\nu} = R^{\mu\nu} - \frac{1}{2}g^{\mu\nu}R \quad . \tag{2.3}$$

Ricci tensor can be written as

$$R_{\mu\nu} = \frac{\partial}{\partial x^{\nu}}\Gamma^{\alpha}_{\mu\alpha} - \frac{\partial}{\partial x^{\alpha}}\Gamma^{\alpha}_{\mu\nu} - \Gamma^{\alpha}_{\mu\nu}\Gamma^{\beta}_{\alpha\beta} + \Gamma^{\alpha}_{\mu\beta}\Gamma^{\beta}_{\nu\alpha} \quad , \tag{2.4}$$

where

$$\Gamma^{\lambda}_{\mu\nu} = \frac{1}{2}g^{\lambda\alpha}\left(\frac{\partial g_{\alpha\nu}}{\partial x^{\mu}} + \frac{\partial g_{\alpha\mu}}{\partial x^{\nu}} - \frac{\partial g_{\mu\nu}}{\partial x^{\alpha}}\right). \tag{2.5}$$

For this particular metric in equation (2.1), the connection coefficients are

$$\begin{aligned}
\Gamma^{1}_{00} &= \nu' e^{2(\nu-\lambda)} \ , & \Gamma^{0}_{10} &= \nu' \ , \\
\Gamma^{1}_{11} &= \lambda' \ , & \Gamma^{2}_{12} &= \Gamma^{3}_{13} = r^{-1} \ , \\
\Gamma^{1}_{22} &= -re^{-2\lambda} \ , & \Gamma^{3}_{23} &= \cot\theta \ , \\
\Gamma^{1}_{33} &= -r\sin^2\theta \ e^{-2\lambda} \ , & \Gamma^{2}_{33} &= -\sin\theta\cos\theta \ ,
\end{aligned} \tag{2.6}$$

here, the prime denotes differentiation with respective to the co-ordinate r. For the same metric the components of Ricci tensor are given by

$$R_{00} = -\left(\nu'' - \lambda'\nu' + \nu'^2 + \frac{2\nu'}{r}\right) e^{2(\nu-\lambda)} \ , \tag{2.7}$$

$$R_{11} = \nu'' - \lambda'\nu' + \nu'^2 - \frac{2\lambda'}{r} \ , \tag{2.8}$$

$$R_{22} = (1 + r\nu' - r\lambda')e^{-2\lambda} - 1 \ , \tag{2.9}$$

$$R_{33} = R_{22}\sin^2\theta \ , \tag{2.10}$$

and the Ricci scalar R is

$$R = -\frac{2e^{-2\lambda}}{r^2}\left(r^2\nu'' + r^2\nu'^2 - r^2\nu'\lambda' + 2r\nu' - 2r\lambda' - e^{2\lambda} + 1\right). \tag{2.11}$$

The Einstein tensor in the mixed representation can be written as,

$$G_\nu{}^\mu = R_\nu{}^\mu - \frac{1}{2}\delta_\nu{}^\mu R \quad , \tag{2.12}$$

where the mixed Ricci tensor is

$$R_\nu{}^\mu = g^{\mu\tau} R_{\tau\nu}. \tag{2.13}$$

The components of Einstein tensor in the mixed representation are

$$\begin{aligned} G_0{}^0 &= \frac{e^{-2\lambda}}{r^2}(1 - 2r\lambda') - \frac{1}{r^2} \ , \\ G_1{}^1 &= \frac{e^{-2\lambda}}{r^2}(1 + 2r\nu') - \frac{1}{r^2} \ , \\ G_2{}^2 &= e^{-2\lambda}\left(\nu'' + \nu'^2 - \nu'\lambda' + \frac{\nu' - \lambda'}{r}\right) \ , \\ G_3{}^3 &= G_2{}^2 \ . \end{aligned} \tag{2.14}$$

Outside the star the energy-momentum tensor vanishes, so the Einstein's equation becomes

$$G_{\mu\nu} = 0 \ , \tag{2.15}$$

and from equation (2.3) it follows that

$$R_{\mu\nu} = \frac{1}{2} g_{\mu\nu} R. \tag{2.16}$$

Multiplying both side of the above equation by $g^{\alpha\mu}$, we get,

$$R_\nu{}^\alpha = \frac{1}{2}\delta_\nu{}^\alpha R \tag{2.17}$$

which on contraction for $\alpha = \nu$ gives,

$$R = \frac{1}{2}R \quad \Longrightarrow \quad R = 0. \tag{2.18}$$

Consequently, $R_{\mu\nu} = 0$. Therefore, in empty space the Ricci scalar and Ricci tensor both vanish.

Setting $R_{00} = R_{11} = 0$ and combining equations (2.7) and (2.8) leads to the following equation,

$$-\left(\frac{2\nu'}{r} + \frac{2\lambda'}{r}\right) e^{2(\nu-\lambda)} = 0. \tag{2.19}$$

From the above equation we find that

$$\lambda' + \nu' = 0. \tag{2.20}$$

It also implies,

$$\lambda + \nu = C, \tag{2.21}$$

where C is a constant of integration. Using $R_{22} = 0$ and the above results in equation (2.9), we get,

$$(1 - 2r\lambda')e^{-2\lambda} = \frac{d}{dr}(re^{-2\lambda}) = 1. \tag{2.22}$$

The integration of the above equation then yields

$$g_{11}(r) = -e^{2\lambda} = -\left(1 + \frac{C_1}{r}\right)^{-1}, \tag{2.23}$$

with C_1 being another constant of integration.

From these results the metric function $g_{00}(r)$ can be written as

$$g_{00}(r) = e^{2\nu} = e^{-2\lambda+2C} = C_2\left(1 + \frac{C_1}{r}\right), \tag{2.24}$$

where C_2 $(= e^{2C})$ must be unity in order to give the correct limit as $r \to \infty$. This condition gives the constant $C = 0$.

The result should also agree with Newtonian (or weak gravitational) limit

$$g_{00} = 1 + 2\Phi\ , \tag{2.25}$$

with potential

$$\Phi = -\frac{GM}{r}\ , \tag{2.26}$$

which gives the integration constant

$$C_1 = -2GM. \tag{2.27}$$

Therefore, the line element for Schwarzschild solution (outside the star) becomes

$$d\tau^2 = \left(1 - \frac{2GM}{r}\right) dt^2 - \left(1 - \frac{2GM}{r}\right)^{-1} dr^2 - r^2(d\theta + sin^2\theta d\phi^2). \tag{2.28}$$

Now, in a static star made of perfect fluid, the energy momentum tensor can be written as

$$T_0{}^0 = \epsilon, \quad \text{and} \qquad T_i{}^i = -p. \tag{2.29}$$

From equations (2.14) and (2.2), we can obtain the differential equations for the functions $\nu(r)$ and $\lambda(r)$ as

$$\begin{aligned} \frac{e^{-2\lambda(r)}}{r^2}[1-2r\lambda'(r)]-\frac{1}{r^2} &= \kappa\epsilon(r)\ , && (2.30)\\ \frac{e^{-2\lambda(r)}}{r^2}[1+2r\nu'(r)]-\frac{1}{r^2} &= -\kappa p(r)\ , && (2.31)\\ e^{-2\lambda(r)}\left[\nu''(r)+\nu'(r)^2-\nu'(r)\lambda'(r)+\frac{\nu'(r)-\lambda'(r)}{r}\right] &= -\kappa p(r)\ . && (2.32) \end{aligned}$$

Integrating the first equation (2.30) we get

$$e^{-2\lambda(r)} = 1+\frac{\kappa}{r}\int_0^r \tilde{r}^{\,2}\epsilon(\tilde{r})d\tilde{r}\ . \tag{2.33}$$

Let us introduce

$$M(r) \equiv 4\pi\int_0^r \tilde{r}^{\,2}\epsilon(\tilde{r})d\tilde{r}\ . \tag{2.34}$$

The metric is continuous at the surface of the star and this result matches Schwarzschild solution at $r = R$, where R denotes the radius of the star and the corresponding $M(R)$ is interpreted as the gravitational mass M of the star i. e. $M = M(R)$.

From the continuity of the metric at the surface of star we can write

$$e^{-2\lambda(R)} = 1+\frac{\kappa}{R}\int_0^R \tilde{r}^{\,2}\epsilon(\tilde{r})d\tilde{r} = 1-\frac{2GM}{R}. \tag{2.35}$$

Now, comparing both side of the above equation, one can easily obtain

$$\kappa = -8\pi G. \tag{2.36}$$

After rearranging, one may rewrite equations (2.30) and (2.31) as

$$\begin{aligned} 2r\lambda'(r) &= 1-e^{2\lambda(r)}[1+\kappa r^2\epsilon(r)], && (2.37)\\ 2r\nu'(r) &= -1+e^{2\lambda(r)}[1-\kappa r^2 p(r)]. && (2.38) \end{aligned}$$

The derivative of the latter equation gives

$$2\nu'(r) + 2r\nu''(r) = [2\lambda'(r)\{1 - \kappa r^2 p(r)\} - \kappa\{2rp(r) + r^2 p'(r)\}]e^{2\lambda(r)}. \tag{2.39}$$

Combining the last three equations (2.37), (2.38) and (2.39) one can easily get an expression for $\nu''(r)$ as

$$\begin{aligned} 2r^2\nu''(r) &= 1 - [2\kappa r^2 p(r) + \kappa r^3 p'(r)]e^{2\lambda(r)} \\ &\quad -[1 - \kappa r^2 p(r)][1 + \kappa r^2 \epsilon(r)]e^{4\lambda(r)}. \end{aligned} \tag{2.40}$$

Plugging the expression for $\lambda'(r)$ (2.37), $\nu'(r)$ (2.38), and $\nu''(r)$ (2.40) in equation (2.32) and using $\kappa = -8\pi G$, the differential equation for the pressure can be obtained as follows

$$\frac{dp}{dr} = -\frac{G[p(r) + \epsilon(r)][M(r) + 4\pi r^3 p(r)]}{r[r - 2GM(r)]}. \tag{2.41}$$

The above equation is the general relativistic equation of hydrostatic equilibrium for spherically symmetric objects, which is known as Tolman-Oppenheimer-Volkoff equation. The TOV equation (2.41) can be solved simultaneously with mass equation (2.34), which gives mass and radius of compact stellar object like neutron star. While solving, the mass at the centre is taken to be zero, i.e. $M(0) = 0$, and the pressure at the centre is denoted as $p(0) \equiv P_c$. The radius of the star R is defined as the value of r at which pressure vanishes ($p(R) = 0$) and mass of the star as $M = M(R)$. However, one thing to be noted that there are three variable $M(r)$, $p(r)$ and $\epsilon(r)$ but only two equations. Therefore, one must need another equation which provides the relation between pressure p and energy density ϵ, the equation of state, of the system in order to solve these equations. In other word, TOV equations are solved using equation of state as input to obtain the important bulk properties like mass and radius of stellar object.

2.2 EoS for Neutron Star

In the previous section, we have seen that the equation of state of neutron star matter is needed to solve the TOV equations. A complete description of neutron stars includes EoS for the interior region to the inner and outer crusts, covering a wide range of density and asymmetry. Several phases and compositions of matter appear at different sectors of neutron star matter. The phase transition from uniform matter to non-uniform matter occurs at density around $0.06-0.09$ fm^{-3}. Therefore, different theoretical methods are required to obtain the EoS for different density regions of a neutron star. Generally, for the crust region, one employs the EoS by Baym-Pethick-Sutherland (BPS) [72] together with the Baym-Bethe-Pethick (BBP) [73], the NegeleVautherin (NV) [74] or the Douchin-Haensel (DH) [75]. And for the high density homogeneous part, many non-relativistic and relativistic approaches have been used. The differences in the models used for the different segments of neutron star matter usually lead to some discontinuity and inconsistency in the matching of the composite EoSs, which affects neutron star radii significantly. Therefore, recently considerable effort has been put to construct *unified* EoS, i.e. all segments of the EoS are calculated within the same nuclear model.

Here, in this section, we will concentrate on the theory for interior homogeneous part of the neutron star. It has been believed that the interior bulk part of neutron stars are composed of highly asymmetric dense nuclear matter. The EoS for neutron star matter has been calculated with $T = 0$ approximation, as the Fermi energy of the nucleons are much larger than the thermal energy associated with the internal temperatures ($\sim 10^7 - 10^9$ K) of the star. There are several competing models which describe the unknown equation of state of ultra-dense matter. But many of them are ruled out due to their inability to satisfy the constraints coming from different experimental data and the observations of massive ($\sim 2M_{\odot}$) neutron stars. Still, various models, which are successfully pass through these constraints, are available in the literature. The models generally used to calculate the EoS of neutron star matter in recent days, can be broadly categorized into two groups: (1) non-relativistic and relativistic potential models and (2) relativistic field theoretical models. These different nuclear models give quite different masses and radii of neutron stars, although their saturation properties are similar. In the following section, we give an overview of the nuclear models, Relativistic mean field theory and Skyrme-Hartree-Fock approach, which are mainly used in this thesis to calculate the core part of the neutron star EoS.

2.2.1 Relativistic Mean Field theory

Relativistic mean field (RMF) model is one of the most successful models for the description of nuclear matter as well as finite nuclei [36, 76–82]. It is a relativistic description of nuclear matter within field theoretical framework. In the conventional RMF theory nucleons are treated as elementary particles and interaction between the nucleons are mediated by the exchange of σ, ω and ρ mesons. The σ mesons give rise to the strong attractive force, while the ω mesons cause the strong repulsive force between the nucleons. In addition to this, we have taken into account the contributions from the delta mesons in a minimal way through the linear coupling to nucleons, which has significant effect on the bulk properties of finite nuclei. Several self and cross interaction terms between the mesons are also considered to yield the saturation properties correctly and vary the density dependence of symmetry energy. The Lagrangian density for the extended RMF model can be written as,

$$\mathcal{L} = \mathcal{L}_{\mathcal{NM}} + \mathcal{L}_{\sigma} + \mathcal{L}_{\omega} + \mathcal{L}_{\rho} + \mathcal{L}_{\delta} + \mathcal{L}_{\sigma\omega\rho} \ , \tag{2.42}$$

where the Lagrangian $\mathcal{L}_{\mathcal{NM}}$ describing the interactions of the nucleons through the mesons is,

$$\mathcal{L}_{\mathcal{NM}} = \sum_{J=n,p} \overline{\Psi}_J[i\gamma^\mu\partial_\mu - (M - g_\sigma\sigma - g_\delta\delta.\tau) - (g_\omega\gamma^\mu\omega_\mu + \frac{1}{2}g_\rho\gamma^\mu\tau.\rho_\mu)]\Psi_J. \quad (2.43)$$

Here, the sum is taken over the neutrons and protons and τ are the isospin matrices. The Lagrangian describing self interactions for σ, ω, and ρ mesons can be written as,

$$\begin{aligned}
\mathcal{L}_\sigma &= \frac{1}{2}(\partial_\mu\sigma\partial^\mu\sigma - m_\sigma^2\sigma^2) - \frac{\kappa_3}{6M}g_\sigma m_\sigma^2\sigma^3 - \frac{\kappa_4}{24M^2}g_\sigma^2 m_\sigma^2\sigma^4, \\
\mathcal{L}_\omega &= -\frac{1}{4}\omega_{\mu\nu}\omega^{\mu\nu} + \frac{1}{2}m_\omega^2\omega_\mu\omega^\mu + \frac{1}{24}\zeta_0 g_\omega^2(\omega_\mu\omega^\mu)^2, \\
\mathcal{L}_\rho &= -\frac{1}{4}\rho_{\mu\nu}\rho^{\mu\nu} + \frac{1}{2}m_\rho^2\rho_\mu\rho^\mu, \\
\mathcal{L}_\delta &= \frac{1}{2}(\partial_\mu\delta\partial^\mu\delta - m_\delta^2\delta^2). \quad (2.44)
\end{aligned}$$

The $\omega^{\mu\nu}$, $\rho^{\mu\nu}$ are field tensors corresponding to the ω and ρ mesons, and can be defined as $\omega^{\mu\nu} = \partial^\mu\omega^\nu - \partial^\nu\omega^\mu$ and $\rho^{\mu\nu} = \partial^\mu\rho^\nu - \partial^\nu\rho^\mu$. The cross interactions of σ, ω, and ρ mesons are described by $\mathcal{L}_{\sigma\omega\rho}$ which can be written as,

$$\begin{aligned}
\mathcal{L}_{\sigma\omega\rho} &= \frac{\eta_1}{2M}g_\sigma m_\omega^2\sigma\omega_\mu\omega^\mu + \frac{\eta_2}{4M^2}g_\sigma^2 m_\omega^2\sigma^2\omega_\mu\omega^\mu + \frac{\eta_\rho}{2M}g_\sigma m_\rho^2\sigma\rho_\mu\rho^\mu \\
&\quad + \frac{\eta_{1\rho}}{4M^2}g_\sigma^2 m_\rho^2\sigma^2\rho_\mu\rho^\mu + \frac{\eta_{2\rho}}{4M^2}g_\omega^2 m_\rho^2\omega_\mu\omega^\mu\rho_\mu\rho^\mu\ . \quad (2.45)
\end{aligned}$$

From the Lagrangian density, one can derive a set of field equations by using the Euler-Lagrange equation

$$\frac{\partial}{\partial x^\mu}\left(\frac{\partial\mathcal{L}}{\partial(\partial\phi_\alpha/\partial x^\mu)}\right) - \frac{\partial\mathcal{L}}{\partial\phi_\alpha} = 0\ , \quad (2.46)$$

where ϕ_α are different fields involved in the theory. The Dirac equation for the nucleon field is given by

$$\left[i\gamma^{\mu}\partial_{\mu} - (M - g_{\sigma}\sigma - g_{\delta}\delta.\tau) - (g_{\omega}\gamma^{\mu}\omega_{\mu} + \frac{1}{2}g_{\rho}\gamma^{\mu}\tau.\rho_{\mu})\right]\Psi_J = 0, \tag{2.47}$$

and the Klein-Gordon equations for the meson fields are given by

$$\begin{aligned}
\partial_{\mu}\partial^{\mu}\sigma + m_{\sigma}^2\sigma &= -g_{\sigma}\bar{\psi}\psi - \frac{\kappa_3}{2M}g_{\sigma}m_{\sigma}^2\sigma^2 - \frac{\kappa_4}{6M^2}g_{\sigma}^2m_{\sigma}^2\sigma^3 + \frac{\eta_1}{2M}g_{\sigma}m_{\omega}^2\omega_{\mu}\omega^{\mu} \\
&\quad + \frac{\eta_2}{2M^2}g_{\sigma}^2m_{\omega}^2\sigma\omega_{\mu}\omega^{\mu} + \frac{\eta_{\rho}}{2M}g_{\sigma}m_{\rho}^2\rho_{\mu}\rho^{\mu} \\
&\quad + \frac{\eta_{1\rho}}{2M^2}g_{\sigma}^2m_{\rho}^2\sigma\rho_{\mu}\rho^{\mu} \ , \qquad (2.48) \\
\partial_{\mu}\omega^{\mu\nu} + m_{\omega}^2\omega^{\nu} &= g_{\omega}\bar{\psi}\gamma^{\nu}\psi - \frac{1}{6}\zeta_0g_{\omega}^2(\omega_{\mu}\omega^{\mu})\omega^{\nu} + \frac{\eta_1}{M}g_{\sigma}m_{\omega}^2\sigma\omega^{\nu} \\
&\quad + \frac{\eta_2}{2M^2}g_{\sigma}^2m_{\omega}^2\sigma^2\omega^{\nu} + \frac{\eta_{2\rho}}{2M^2}g_{\omega}^2m_{\rho}^2(\rho_{\mu}\rho^{\mu})\omega^{\nu} \ , \qquad (2.49) \\
\partial_{\mu}\rho^{\mu\nu} + m_{\rho}^2\rho^{\nu} &= g_{\rho}\bar{\psi}\tau\gamma^{\nu}\psi + \frac{\eta_{\rho}}{M}g_{\sigma}m_{\rho}^2\sigma\rho^{\nu} + \frac{\eta_{1\rho}}{2M^2}g_{\sigma}^2m_{\rho}^2\sigma^2\rho^{\nu} \\
&\quad + \frac{\eta_{2\rho}}{2M^2}g_{\omega}^2m_{\rho}^2(\omega_{\mu}\omega^{\mu})\rho^{\nu} \ , \qquad (2.50) \\
\partial_{\mu}\partial^{\mu}\delta + m_{\sigma}^2\delta &= -g_{\delta}\bar{\psi}\tau\psi. \qquad (2.51)
\end{aligned}$$

The above field equations are non-linear coupled equations and very hard to solve exactly. However, these equations can be simplified by adopting the relativistic mean field approximation. In this approximation, the meson fields are treated as classical fields, and the field operators σ, ω^{μ}, and ρ^{μ} are replaced by their expectation values $\langle\sigma\rangle, \langle\omega^{\mu}\rangle$, and $\langle\rho^{\mu}\rangle$. The translational invariance of infinite nuclear matter makes the equations more simplified by removing the derivative terms. The spatial components of the vector meson fields also vanish under the rotational symmetry. For the isovector-vector meson field ρ^{μ}, only the third component of isospin has a nonvanishing value due to the charge conservation. After all these simplifications, the field equations for mesons are reduced to

$$\begin{aligned}
\sigma_0 \;&\equiv\; \langle\sigma\rangle = -\frac{g_\sigma}{m_\sigma^2}\langle\bar{\psi}\psi\rangle - \frac{1}{m_\sigma^2}\Big[\frac{\kappa_3}{2M}g_\sigma m_\sigma^2\sigma_0^2 + \frac{\kappa_4}{6M^2}g_\sigma^2 m_\sigma^2\sigma_0^3 - \frac{\eta_1}{2M}g_\sigma m_\omega^2\omega_0^2 \\
&\quad -\frac{\eta_2}{2M^2}g_\sigma^2 m_\omega^2\sigma_0\omega_0^2 - \frac{\eta_\rho}{2M}g_\sigma m_\rho^2\rho_0^2 - \frac{\eta_{1\rho}}{2M^2}g_\sigma^2 m_\rho^2\sigma_0\rho_0^2\Big]\ , && (2.52) \\
\omega_0 \;&\equiv\; \langle\omega^0\rangle = \frac{g_\omega}{m_\omega^2}\langle\bar{\psi}\gamma^0\psi\rangle - \frac{1}{m_\omega^2}\Big[\frac{1}{6}\zeta_0 g_\omega^2\omega_0^3 - \frac{\eta_1}{M}g_\sigma m_\omega^2\sigma_0\omega_0 \\
&\quad -\frac{\eta_2}{2M^2}g_\sigma^2 m_\omega^2\sigma_0^2\omega_0 - \frac{\eta_{2\rho}}{2M^2}g_\omega^2 m_\rho^2\rho_0^2\omega_0\Big]\ , && (2.53) \\
\rho_0 \;&\equiv\; \langle\rho^{30}\rangle = \frac{g_\rho}{m_\rho^2}\langle\bar{\psi}\tau_3\gamma^0\psi\rangle + \frac{1}{m_\rho^2}\Big[\frac{\eta_\rho}{M}g_\sigma m_\rho^2\sigma_0\rho_0 + \frac{\eta_{1\rho}}{2M^2}g_\sigma^2 m_\rho^2\sigma_0^2\rho_0 \\
&\quad +\frac{\eta_{2\rho}}{2M^2}g_\omega^2 m_\rho^2\omega_0^2\rho_0\Big]\ , && (2.54) \\
\delta_0 \;&\equiv\; \langle\delta^3\rangle = \frac{g_\delta}{m_\delta^2}\langle\bar{\psi}\tau_3\psi\rangle. && (2.55)
\end{aligned}$$

and the Dirac equation then becomes

$$\left(-i\alpha_k\nabla^k + \beta M_i^* + g_\omega\omega_0 + g_\rho\tau_3\rho_0\right)\psi_i = \varepsilon_i\psi_i, \tag{2.56}$$

where $M_i^* = M - g_\sigma\sigma_0 + g_\delta\tau_3\delta_0$ is the effective mass and ε_i is the single-particle energy of the nucleons. The index i denotes the isospin degree of freedom of the nucleons i.e. $i = p$ for protons and $i = n$ for neutrons.

The ground-state expectation values of the nucleon currents appearing in Eqs.(2.52)-(2.55) can be evaluated by using the Dirac theory as

$$\begin{aligned}
\langle\bar{\psi}\psi\rangle &= n_{s,n} + n_{s,p}\ , && (2.57) \\
\langle\bar{\psi}\gamma^0\psi\rangle &= n_n + n_p\ , && (2.58) \\
\langle\bar{\psi}\tau_3\gamma^0\psi\rangle &= n_n - n_p\ , && (2.59) \\
\langle\bar{\psi}\tau_3\psi\rangle &= n_{s,n} - n_{s,p}\ , && (2.60)
\end{aligned}$$

where n_i and $n_{s,i}$ represent the number density and the scalar density of the nucleons, respectively. And their explicit forms are given by

$$
\begin{aligned}
n_i &= \frac{1}{\pi^2}\int_0^\infty dk\, k^2\, \left(f_{i+}+f_{i-}\right), \qquad (2.61)\\
n_{s,i} &= \frac{1}{\pi^2}\int_0^\infty dk\, k^2\, \frac{M_i^*}{\sqrt{k^2+M_i^{*2}}}\left(f_{i+}+f_{i-}\right). \qquad (2.62)
\end{aligned}
$$

Nucleons occupy single-particle orbits with the occupation probability $f_{i\pm}$. The $(+)$ and $(-)$ signs in the $f_{i\pm}$ correspond to the nucleons and anti-nucleons, respectively. For finite temperature, the occupation probability is given by Fermi-Dirac distribution,

$$
\begin{aligned}
f_{i+} &= \frac{1}{1+\exp\left[\left(\sqrt{k^2+M_i^{*2}}-\nu_i\right)/T\right]}, \qquad (2.63)\\
f_{i-} &= \frac{1}{1+\exp\left[\left(\sqrt{k^2+M_i^{*2}}+\nu_i\right)/T\right]}, \qquad (2.64)
\end{aligned}
$$

with effective chemical potential

$$
\nu_i = \mu_i - g_\omega\omega_0 - g_\rho\tau_3\rho_0. \qquad (2.65)
$$

where τ_3 is the third component of the isospin operator. At $T = 0$ MeV, we consider no anti-nucleons, and the distribution function for nucleons $f_{i+} = 1$ under Fermi surface and $f_{i+} = 0$ above Fermi surface.

Plugging the ground-state expectation values of the nucleon source currents, the equations for meson fields can be rewritten as

$$
\begin{aligned}
\sigma_0 &= -\frac{g_\sigma}{m_\sigma^2}\sum_i \frac{1}{\pi^2}\int_0^\infty dk\, k^2\, \frac{M_i^*}{\sqrt{k^2+M_i^{*2}}}\left(f_{i+}+f_{i-}\right) - \frac{1}{m_\sigma^2}\Big[\frac{\kappa_3}{2M} g_\sigma m_\sigma^2 \sigma_0^2 \\
&\quad + \frac{\kappa_4}{6M^2} g_\sigma^2 m_\sigma^2 \sigma_0^3 - \frac{\eta_1}{2M} g_\sigma m_\omega^2 \omega_0^2 - \frac{\eta_2}{2M^2} g_\sigma^2 m_\omega^2 \sigma_0 \omega_0^2 \\
&\quad - \frac{\eta_\rho}{2M} g_\sigma m_\rho^2 \rho_0^2 - \frac{\eta_{1\rho}}{2M^2} g_\sigma^2 m_\rho^2 \sigma_0 \rho_0^2\Big] \ , \qquad (2.66)
\end{aligned}
$$

$$
\begin{aligned}
\omega_0 &= \frac{g_\omega}{m_\omega^2}\left(n_p+n_n\right) - \frac{1}{m_\omega^2}\Big[\frac{1}{6}\zeta_0 g_\omega^2 \omega_0^3 - \frac{\eta_1}{M} g_\sigma m_\omega^2 \sigma_0 \omega_0 \\
&\quad - \frac{\eta_2}{2M^2} g_\sigma^2 m_\omega^2 \sigma_0^2 \omega_0 - \frac{\eta_{2\rho}}{2M^2} g_\omega^2 m_\rho^2 \rho_0^2 \omega_0\Big], \qquad (2.67)
\end{aligned}
$$

$$
\begin{aligned}
\rho_0 &= \frac{g_\rho}{m_\rho^2}\left(n_p-n_n\right) + \frac{1}{m_\rho^2}\Big[\frac{\eta_\rho}{M} g_\sigma m_\rho^2 \sigma_0 \rho_0 + \frac{\eta_{1\rho}}{2M^2} g_\sigma^2 m_\rho^2 \sigma_0^2 \rho_0 \\
&\quad + \frac{\eta_{2\rho}}{2M^2} g_\omega^2 m_\rho^2 \omega_0^2 \rho_0\Big], \qquad (2.68)
\end{aligned}
$$

$$
\begin{aligned}
\delta_0 &= -\frac{g_\sigma}{m_\sigma^2}\frac{1}{\pi^2}\Big[\int_0^\infty dk\, k^2\, \frac{M_n^*}{\sqrt{k^2+M^{*2}}}\left(f_{nk}+f_{\bar{n}k}\right) \\
&\quad - \int_0^\infty dk\, k^2\, \frac{M_p^*}{\sqrt{k^2+M^{*2}}}\left(f_{pk}+f_{\bar{p}k}\right)\Big]. \qquad (2.69)
\end{aligned}
$$

Now, these field equations can be solved self-consistently. A detailed description of this theory and different thermodynamical quantities can be found in Ref. [78]. The energy density of nuclear matter is given by

$$
\begin{aligned}
\epsilon &= \sum_i \frac{1}{\pi^2}\int_0^\infty dk\, k^2 \sqrt{k^2+M_i^{*2}}\left(f_{i+}+f_{i-}\right) + \frac{1}{2} m_\sigma^2 \sigma_0^2 + \frac{\kappa_3}{6M} g_\sigma m_\sigma^2 \sigma_0^3 + \frac{\kappa_4}{24M^2} g_\sigma^2 m_\sigma^2 \sigma_0^4 \\
&\quad + g_\omega \omega_0 \left(n_p+n_n\right) - \frac{1}{2} m_\omega^2 \omega_0^2 - \frac{1}{24}\zeta_0 g_\omega^2 \omega_0^4 + g_\rho \rho_0 \left(n_p-n_n\right) - \frac{1}{2} m_\rho^2 \rho_0^2 + \frac{1}{2} m_\delta^2 \delta_0^2 \\
&\quad - \frac{\eta_1}{2M} g_\sigma m_\omega^2 \sigma_0 \omega_0^2 - \frac{\eta_2}{4M^2} g_\sigma^2 m_\omega^2 \sigma_0^2 \omega_0^2 - \frac{\eta_\rho}{2M} g_\sigma m_\rho^2 \sigma_0 \rho_0^2 \qquad (2.70) \\
&\quad - \frac{\eta_{1\rho}}{4M^2} g_\sigma^2 m_\rho^2 \sigma_0^2 \rho_0^2 - \frac{\eta_{2\rho}}{4M^2} g_\omega^2 m_\rho^2 \omega_0^2 \rho_0^2 \ ,
\end{aligned}
$$

the pressure of nuclear matter is given by

$$\begin{aligned}
p &= \sum_i \frac{1}{3\pi^2}\int_0^\infty dk\, k^2 \frac{k^2}{\sqrt{k^2+M_i^{*2}}}\left(f_{i+}+f_{i-}\right) - \frac{1}{2}m_\sigma^2\sigma_0^2 + \frac{\kappa_3}{6M}g_\sigma m_\sigma^2\sigma_0^3 \\
&+\frac{\kappa_4}{24M^2}g_\sigma^2 m_\sigma^2\sigma_0^4 + \frac{1}{2}m_\omega^2\omega_0^2 + \frac{1}{24}\zeta_0 g_\omega^2\omega_0^4 + \frac{1}{2}m_\rho^2\rho_0^2 - \frac{1}{2}m_\delta^2\delta_0^2 \\
&+\frac{\eta_1}{2M}g_\sigma m_\omega^2\sigma_0\omega_0^2 + \frac{\eta_2}{4M^2}g_\sigma^2 m_\omega^2\sigma_0^2\omega_0^2 + \frac{\eta_\rho}{2M}g_\sigma m_\rho^2\sigma_0\rho_0^2 \qquad (2.71)\\
&+\frac{\eta_{1\rho}}{4M^2}g_\sigma^2 m_\rho^2\sigma_0^2\rho_0^2 + \frac{\eta_{2\rho}}{4M^2}g_\omega^2 m_\rho^2\omega_0^2\rho_0^2.
\end{aligned}$$

The entropy density $\mathcal{S}$ is calculated considering the nucleons as quasiparticles

$$\mathcal{S} = -\sum_{i=n,p}\int\frac{d^3p}{4\pi^3}\left[f_{i+}\ln f_{i+} + \left(1-f_{i+}\right)\ln\left(1-f_{i+}\right) + \left(f_{i+}\leftrightarrow f_{i-}\right)\right]. \quad (2.72)$$

It may be noted from equations (2.71) and (2.72) that to calculate the EoS in terms of ϵ versus ρ or p versus ρ, we need the values of fields and different coupling constants involved in the model. The values of these coupling constants are determined in such a way that they yield appropriate values for finite nuclei properties (e.g. binding energy, charge radii) and various quantities associated with the nuclear matter at the saturation density.

2.2.2 Skyrme-Hartree-Fock theory

Skyrme force is an effective nucleon-nucleon interaction which was originally introduced by Skyrme in 1959 [83]. It is a zero-range, momentum dependent, non-relativistic nuclear interaction widely used in the mean-field Hartree-Fock calculations and successfully describe the gross properties of finite nuclei. This zero-range interaction is easy to handle in the Hartree-Fock calculation. However, the momentum dependence of the zero-range force accounts for the finite-range effect between the nucleons. In the Skyrme force, the effects of many-body interaction are also included through the density dependent two body interaction. The Skyrme interaction between two nucleons in the configuration space can be expressed as

$$\begin{aligned} v_{\rm Sk}(\mathbf{r}_i, \mathbf{r}_j) &= t_0(1+x_0\hat{P}_\sigma)\delta(\mathbf{r}_i-\mathbf{r}_j) + \frac{t_1}{2}(1+x_1\hat{P}_\sigma)\left[\delta(\mathbf{r}_i-\mathbf{r}_j)\hat{\mathbf{k}}^2 + \hat{\mathbf{k}}^{\dagger 2}\delta(\mathbf{r}_i-\mathbf{r}_j)\right] \\ &\quad + t_2(1+x_2\hat{P}_\sigma)\hat{\mathbf{k}}^\dagger\cdot\delta(\mathbf{r}_i-\mathbf{r}_j)\hat{\mathbf{k}} + \frac{1}{6}t_3(1+x_3\hat{P}_\sigma)n^\alpha\delta(\mathbf{r}_i-\mathbf{r}_j) \\ &\quad + iW_0\hat{\mathbf{k}}^\dagger\delta(\mathbf{r}_i-\mathbf{r}_j)\times\hat{\mathbf{k}}\cdot(\hat{\boldsymbol{\sigma}}_i+\hat{\boldsymbol{\sigma}}_j)\,, \end{aligned} \tag{2.73}$$

where $\hat{P}_\sigma = \frac{1}{2}(1+\hat{\boldsymbol{\sigma}}_i\cdot\hat{\boldsymbol{\sigma}}_j)$ is the spin-exchange operator, and $\hat{\mathbf{k}}$ is defined as

$$\hat{\mathbf{k}} = \frac{1}{2i}(\nabla_i - \nabla_j). \tag{2.74}$$

t_i, x_i and α are the parameters of the interactions which are determined by fitting some static properties of nuclei and nuclear matter obtained from the finite nuclei experiments (e.g. binding energy, root mean square radius of spherical nucleus and incompressibility, energy per nucleon of nuclear matter, etc.) and W_0-term gives the spin-orbit interaction which is important to explain the structure of finite nuclei.

In the Hartree-Fock theory with Skyrme interaction, the total binding energy of the nuclear system is given by

$$E = \int d^3r\,\mathcal{E} = \int d^3r\,(\mathcal{E}_B + \mathcal{E}_C + \mathcal{E}_J + \mathcal{E}_g), \tag{2.75}$$

where $\mathcal{E}_B$ is the bulk part contribution, $\mathcal{E}_C$ is the Coulomb contribution, $\mathcal{E}_J$ is the contribution from the spin-orbit term, and $\mathcal{E}_g$ is the contribution from the density gradient term. For the homogeneous bulk nuclear matter in the neutron star core the energy density functional can be written as [84–86]

$$\begin{aligned}\mathcal{E} \simeq \mathcal{E}_B \;&=\; \frac{\hbar^2}{2m_n}\tau_n + \frac{\hbar^2}{2m_p}\tau_p + n(\tau_n+\tau_p)\left[\frac{t_1}{4}\left(1+\frac{x_1}{2}\right) + \frac{t_2}{4}\left(1+\frac{x_2}{2}\right)\right] \\ &\quad + (\tau_n n_n + \tau_p n_p)\left[\frac{t_2}{4}\left(\frac{1}{2}+x_2\right) - \frac{t_1}{4}\left(\frac{1}{2}+x_1\right)\right] \\ &\quad + \frac{t_0}{2}\left[\left(1+\frac{x_0}{2}\right)n^2 - \left(\frac{1}{2}+x_0\right)(n_n^2+n_p^2)\right] \\ &\quad + \frac{t_3}{12}\left[\left(1+\frac{x_3}{2}\right)n^2 - \left(\frac{1}{2}+x_3\right)(n_n^2+n_p^2)\right]n^\alpha\,, \end{aligned} \tag{2.76}$$

where m_n and m_p are neutron and proton masses, n_n and n_p are the number densities of neutrons and protons, the total baryon number density $n = n_n + n_p$, and τ_n and τ_p are kinetic energy densities of neutrons and protons, respectively. This Skyrme functional has often been employed to calculate the EoS for nuclear matter inside the neutron star.

We consider the neutron star composed of nucleons, electrons and muons which are $\beta-$stable. Further, the matter is charge neutral. The fraction of each of the species of the particle at a fixed density ρ can be determined by the $\beta-$equilibrium and charge neutrality conditions as follows,

$$\mu_n = \mu_p + \mu_e = \mu_p + \mu_\mu \ , \tag{2.77}$$

and

$$\rho_p = \rho_e + \rho_\mu \ , \tag{2.78}$$

where, μ_i and ρ_i with $i = n, p, e$ and μ, indicate the chemical potential and the density of different species, respectively.

2.3 Core-crust transition

The core-crust transition corresponds to the phase transition from homogeneous matter at high densities to the inhomogeneous matter at low densities. The core-crust transition density ρ_t is estimated by the density at which the homogeneous matter becomes unstable against small amplitude density fluctuations, indicating formations of nuclear clusters. There are several methods used widely in literature to study the instability due to small density fluctuations in low density matter. In the present section, we review the methods that will be applied in this thesis work to determine the crust-core transition density: the Thermodynamical method, and the RPA formalism. We also discuss the method to obtain the spinodal section and critical parameters for asymmetric nuclear matter.

2.3.1 Thermodynamical method

The uniform matter inside the neutron star is in equilibrium under the beta decay process. These weak-interaction processes conserve both the baryon number and charge. For a system which conserves baryon number and charge, the first law of thermodynamics at zero temperature can be written as,

$$du = -Pdv - \hat{\mu}dq \tag{2.79}$$

Here u is the internal energy per baryon, $P = P_b + P_e$ is the total pressure of the baryons and electrons, v and q_c are the volume and charge per baryon. In β-equilibrium the chemical potential $\hat{\mu}$ is defined as $\hat{\mu} = \mu_n - \mu_p = \mu_e$.

The system will be stable (in uniform phase) against small density fluctuations, if and only if the internal energy per baryon $u(v, q)$ is a convex function of its variable

v and q. This condition then leads to the following inequalities [7,87,88],

$$-\left(\frac{\partial P}{\partial v}\right)_{\hat{\mu}} > 0, \tag{2.80}$$

$$-\left(\frac{\partial \hat{\mu}}{\partial q_c}\right)_{v} > 0. \tag{2.81}$$

Since the system under consideration is in β-equilibrium, the electron pressure P_e is the only function of $\hat{\mu}$. Eq. (2.80) becomes

$$-\left(\frac{\partial P_b}{\partial v}\right)_{\hat{\mu}} > 0. \tag{2.82}$$

Eqs. (2.81, 2.82) can be expressed in terms of the energy per nucleon $E_b(\rho, x_p)$ at a given density ρ and proton fraction x_p as

$$-\left(\frac{\partial P_b}{\partial v}\right)_{\hat{\mu}} = \rho^2 \left[2\rho\frac{\partial E_b(\rho,x_p)}{\partial \rho} + \rho^2\frac{\partial^2 E_b(\rho,x_p)}{\partial \rho^2} - \frac{\left(\frac{\partial^2 E_b(\rho,x_p)}{\partial\rho\partial x_p}\rho\right)^2}{\frac{\partial^2 E_b(\rho,x_p)}{\partial x_p^2}}\right] > 0\ , \tag{2.83}$$

$$-\left(\frac{\partial q_c}{\partial \hat{\mu}}\right)_{v} = \left(\frac{\partial^2 E_b(\rho,x_p)}{\partial x_p^2}\right)^{-1} + \frac{\mu_e^2}{\pi^2\hbar^3\rho} > 0\ . \tag{2.84}$$

Eq. (2.84) is usually valid, thus, the crust-core transition density is determined by using the inequality of Eq. (2.83).

2.3.2 RRPA method

In relativistic random phase approximation (RRPA), the stability of the uniform ground state is determined by the longitudinal dielectric function ε_L, which can be written as [89],

$$\varepsilon_L = \det\left[1 - D_L(q)\Pi_L(q, q_0 = 0)\right]. \tag{2.85}$$

where, q_0 is the time-component of the four-momentum transfer $q^\mu = (q_0, \vec{q})$ and $q = |\vec{q}|$. The uniform system becomes unstable to small-amplitude density fluctuations with momentum transfer q, when $\varepsilon_L \leq 0$. The transition density between the non-uniform inner crust and the uniform outer core , ρ_t, corresponds to the largest density for which the above condition has a solution. For matter that in general consists of protons, neutrons, electrons and muons, the longitudinal meson propagator D_L, which includes the nonlinear meson couplings, is given by

$$D_L = \begin{pmatrix} d_g & d_g & 0 & -d_g & 0 \\ d_g & d_g & 0 & -d_g & 0 \\ 0 & 0 & -d_s & d^+_{sv\rho} & d^-_{sv\rho} \\ -d_g & -d_g & d^+_{sv\rho} & d_{33} & d^-_{v\rho} \\ 0 & 0 & d^-_{sv\rho} & d^-_{v\rho} & d_{44} \end{pmatrix}, \tag{2.86}$$

where $d^+_{sv\rho} = -(d_{sv} + d_{s\rho})$, $d^-_{sv\rho} = -(d_{sv} - d_{s\rho})$, $d^-_{v\rho} = d_v - d_\rho$, $d_{33} = d_g + d_v + d_\rho + 2d_{v\rho}$ and $d_{44} = d_v + d_\rho - 2d_{v\rho}$. The cross-coupling terms between the mesons in the RMF Lagrangian leads to the appearance of off-diagonal mixing propagators between isoscalar-scalar and isoscalar-vector (d_{sv}), isoscalar-vector and isovector-vector ($d_{v\rho}$), isoscalar-scalar and isovector-vector ($d_{s\rho}$) in Eq. (2.86), in addition to the γ, ω, σ and ρ propagators (d_g, d_v, d_s and d_ρ). These propagators have been derived from the quadratic fluctuations around the static solutions which are generated by the second derivatives of energy density ($\partial^2\epsilon/\partial\phi_i\partial\phi_j$), where ϕ_i and ϕ_j are the involved meson fields. The explicit forms of the σ, ω, and ρ propagators are

$$\begin{aligned}
d_s &= \frac{g_\sigma^2(q^2+m_\omega^{*\,2})(q^2+m_\rho^{*\,2})}{(q^2+m_\omega^{*\,2})(q^2+m_\rho^{*\,2})(q^2+m_\sigma^{*\,2})+(\Pi^0_{\sigma\omega})^2(q^2+m_\rho^{*\,2})+(\Pi^0_{\sigma\rho})^2(q^2+m_\omega^{*\,2})}\ ,\\
d_v &= \frac{g_\omega^2(q^2+m_\sigma^{*\,2})(q^2+m_\rho^{*\,2})}{(q^2+m_\omega^{*\,2})(q^2+m_\rho^{*\,2})(q^2+m_\sigma^{*\,2})+(\Pi^0_{\sigma\omega})^2(q^2+m_\rho^{*\,2})-(\Pi^{00}_{\omega\rho})^2(q^2+m_\sigma^{*\,2})}\ ,\\
d_\rho &= \frac{1/4g_\rho^2(q^2+m_\sigma^{*\,2})(q^2+m_\omega^{*\,2})}{(q^2+m_\omega^{*\,2})(q^2+m_\rho^{*\,2})(q^2+m_\sigma^{*\,2})+(\Pi^0_{\sigma\rho})^2(q^2+m_\omega^{*\,2})-(\Pi^{00}_{\omega\rho})^2(q^2+m_\sigma^{*\,2})}\ ,
\end{aligned} \tag{2.87}$$

and the meson mixing propagators take the following form

$$d_{sv} = \frac{g_\sigma g_\omega \Pi^0_{\omega\sigma}(q^2+m_\rho^{*\,2})}{H(q,q_0=0)}\ , \tag{2.88}$$

$$d_{s\rho} = \frac{1/2g_\rho g_\sigma \Pi^0_{\sigma\rho}(q^2+m_\omega^{*\,2})}{H(q,q_0=0)}\ , \tag{2.89}$$

$$d_{v\rho} = \frac{1/2g_\rho g_\omega \Pi^{00}_{\omega\rho}(q^2+m_\sigma^{*\,2})}{H(q,q_0=0)}\ , \tag{2.90}$$

where the explicit form of $H(q,q_0=0)$ can be written as

$$\begin{aligned}
H(q,q_0=0) &= (q^2+m_\omega^{*\,2})(q^2+m_\rho^{*\,2})(q^2+m_\sigma^{*\,2})\\
&+ (\Pi^0_{\sigma\omega})^2(q^2+m_\rho^{*\,2})+(\Pi^0_{\sigma\rho})^2(q^2+m_\omega^{*\,2})\\
&- (\Pi^{00}_{\omega\rho})^2(q^2+m_\sigma^{*\,2})\ ,
\end{aligned} \tag{2.91}$$

and the meson effective masses in Eq. (2.91) are defined as

$$m_\sigma^{*\,2} = \frac{\partial^2\epsilon}{\partial^2\sigma} = m_\sigma^2+\frac{g_\sigma m_\sigma^2\kappa_3}{M}\sigma+\frac{g_\sigma^2 m_\sigma^2\kappa_4}{2M^2}\sigma^2-\frac{g_\sigma^2 m_\omega^2\eta_2}{2M^2}\omega_0^2-\frac{g_\sigma^2 m_\rho^2\eta_{1\rho}}{2M^2}\rho_0^2\ , \tag{2.92}$$

$$m_\omega^{*\,2} = -\frac{\partial^2\epsilon}{\partial^2\omega_0} = m_\omega^2+\frac{g_\sigma m_\omega^2\eta_1}{M}\sigma+\frac{g_\sigma^2 m_\omega^2\eta_2}{2M^2}\sigma^2+\frac{\zeta_0 g_\omega^2}{2}\omega_0^2+\frac{g_\omega^2 m_\rho^2\eta_{2\rho}}{2M^2}\rho_0^2\ , \tag{2.93}$$

$$m_\rho^{*\,2} = -\frac{\partial^2\epsilon}{\partial^2\rho_0} = m_\rho^2+\frac{g_\sigma m_\rho^2\eta_\rho}{M}\sigma+\frac{g_\sigma^2 m_\rho^2\eta_{1\rho}}{2M^2}\sigma^2+\frac{g_\omega^2 m_\rho^2\eta_{2\rho}}{2M^2}\omega_0^2\ , \tag{2.94}$$

while the polarization due to mesons mixing self-interaction nonlinear terms in Eq. (2.45) (Mix Polarizations) are

$$\begin{aligned}
\Pi^{0}_{\sigma\omega} &= -\frac{\partial^2\epsilon}{\partial\sigma\partial\omega_0} = \frac{g_\sigma m_\omega^2\eta_1}{M}\omega_0 + \frac{g_\sigma^2 m_\omega^2\eta_2}{M^2}\sigma\omega_0 \ , \\
\Pi^{0}_{\sigma\rho} &= -\frac{\partial^2\epsilon}{\partial\sigma\partial\rho_0} = \frac{g_\sigma m_\rho^2\eta_\rho}{M}\rho_0 + \frac{g_\sigma^2 m_\rho^2\eta_{1\rho}}{M^2}\sigma\rho_0 \ , \\
\Pi^{00}_{\omega\rho} &= \frac{\partial^2\epsilon}{\partial\omega_0\partial\rho_0} = -\frac{g_\omega^2 m_\rho^2\eta_{2\rho}}{M^2}\omega_0\rho_0 \ ,
\end{aligned} \tag{2.95}$$

whereas the propagator of photon takes a standard form i.e.,

$$d_g = \frac{e^2}{q^2} \ . \tag{2.96}$$

The longitudinal polarization matrix given in Eq. (2.85) reads

$$\Pi_L = \begin{pmatrix} \Pi^e_{00} & 0 & 0 & 0 & 0 \\ 0 & \Pi^\mu_{00} & 0 & 0 & 0 \\ 0 & 0 & \Pi_s & \Pi^p_m & \Pi^n_m \\ 0 & 0 & \Pi^p_m & \Pi^p_{00} & 0 \\ 0 & 0 & \Pi^n_m & 0 & \Pi^n_{00} \end{pmatrix} . \tag{2.97}$$

The formulas for polarization elements in Π_L are given in, e.g., Ref. [90].

In the crust-core region, usually the muons have not yet appeared, so that Π^μ_{00} can be set to zero, and if we consider the case without electrons, then Π^e_{00} is also set to zero.

2.3.3 Spinodal instability and Critical parameters

We determine the region of instability of nuclear matter constituted by protons and neutrons by calculating the spinodal surface in the (ρ_p, ρ_n, T) space. Stability conditions for asymmetric matter impose that the curvature matrix of the free energy density [91–93]

$$\mathcal{C}_{ij} = \left(\frac{\partial^2 \mathcal{F}}{\partial \rho_i \partial \rho_j} \right)_T , \tag{2.98}$$

is positive. Eq. (2.98) can be rewritten in the form

$$\mathcal{C} = \begin{pmatrix} \frac{\partial \mu_n}{\partial \rho_n} & \frac{\partial \mu_n}{\partial \rho_p} \\ \frac{\partial \mu_p}{\partial \rho_n} & \frac{\partial \mu_p}{\partial \rho_p} \end{pmatrix} , \tag{2.99}$$

imposing

$$\mathrm{Tr}(\mathcal{C}) > 0, \tag{2.100}$$

$$\mathrm{Det}(\mathcal{C}) > 0, \tag{2.101}$$

to fulfil the stability conditions. This is equivalent to requiring that the two eigenvalues

$$\lambda_\pm = \frac{1}{2} \left(\mathrm{Tr}(\mathcal{C}) \pm \sqrt{\mathrm{Tr}(\mathcal{C})^2 - 4\mathrm{Det}(\mathcal{C})} \right) , \tag{2.102}$$

are positive. The largest eigenvalue is always positive and the instability region is delimited by the surface $\lambda_- = 0$. Interesting information is given by the associated eigenvectors $\boldsymbol{\delta\rho}^{\pm}$, defined as

$$\frac{\delta\rho^\pm}{\delta\rho_n^\pm} = \frac{\lambda^\pm - \frac{\partial \mu_n}{\partial \rho_n}}{\frac{\partial \mu_n}{\partial \rho_p}} .$$

In particular, the eigenvector associated with the eigenvalue that defines the spinodal surface determines the instability direction, i.e. the direction along which the free energy decreases. We will also calculate the critical points for each temperature T, which are important to define under which conditions the system is expected to be clusterized. These points satisfy simultaneously [93, 94]

$$
\begin{aligned}
\mathrm{Det}(\mathcal{C}) &= 0 \quad (2.103)\\
\mathrm{Det}(\mathcal{M}) &= 0, \quad (2.104)
\end{aligned}
$$

with

$$
\mathcal{M} = \begin{pmatrix} \mathcal{C}_{11} & \mathcal{C}_{12} \\ \frac{\partial|\mathcal{C}|}{\partial\rho_p} & \frac{\partial|\mathcal{C}|}{\partial\rho_n} \end{pmatrix}. \quad (2.105)
$$

The thermodynamical spinodals and respective critical points will be calculated for several models using the above conditions.

CHAPTER 3

Core-crust transition properties and nuclear symmetry energy

3.1 Introduction

The knowledge of the core-crust transition properties in neutron star matter is very important in understanding the pulsar glitches, crust relaxation in cooling and accreting neutron stars and asteroseismology from giant magnetar flares [95]. The values of core-crust transition density and the corresponding pressure depend crucially on the behaviour of nuclear symmetry energy around the sub-saturation densities. However, density dependence of the nuclear symmetry energy is known with large uncertainties. Some progress in this direction has been made in the last few years [27, 86, 96–100]. In the mean while, several investigations are carried out to study the effects of the variations in the symmetry energy on the core-crust transition properties. The variations in the symmetry energy were achieved either within a single model or by using large set of randomly selected models of different types. The core crust transition density is found to be strongly correlated with the various symmetry energy parameters evaluated at the saturation density. But, results for the correlations between the pressure at the transition point and the symmetry energy obtained from different investigations are at variance.

In the present work, we investigate the correlations between core-crust transition properties and the density dependence of the nuclear symmetry energy for the neutron star matter using three different families of extended relativistic mean-field (ERMF) model. We consider several parameterizations for each of the families of the models which were obtained by systematic variations in such way that they yield wide variations in the values of J_0 and its slope parameter L_0 at the saturation density [101, 102]. The ERMF model includes the contributions from self- and mixed-interaction terms for isoscalar-scalar σ, isoscalar-vector ω and isovector-vector ρ mesons up to the quartic order [101, 103, 104]. The presence of $\sigma - \rho$ and $\omega - \rho$ mixed interaction terms might alter the correlation of various core-crust transition properties to the density dependence of the nuclear symmetry energy. Such investigations are not performed previously in detail [68, 70, 105, 106]. The transition density is calculated using the relativistic random phase approximation (RPA) method. For sake of comparison, we also present some results for core-crust transition density and the corresponding pressure obtained by commonly used RMF parameter sets such as NL3, FSU, GM1 and TM1. We also compare our results with those obtained from dynamical and thermo-dynamical methods.

In the next Sec. 3.2 we discuss in some detail the choices for the different families of the systematically varied ERMF models.

3.2 Systematically varied ERMF parameterizations

We study the core-crust transition density and the corresponding pressure in the neutron star for the three different families of the extended RMF models. These different families are originally obtained in Ref. [102]. They correspond to different choices of the coupling strength, ζ_0, for the self-interaction of the ω-mesons (Eq. (2.44)). The value of ζ_0 were considered to be $\zeta_0 = 0.0, 0.03g_\omega^2$ and $0.06g_\omega^2$. For each of the family, the remaining parameters of the model were systematically varied to yield different values of the neutron-skin thickness in ^{208}Pb nucleus [101, 102]. In other words, for a given ζ_0, the remaining parameter of the model were optimized using exactly same set of the protocol except for the neutron-skin thickness in ^{208}Pb. The fitting protocol comprised of the experimental data for the total binding energies and charge rms radii for many closed shell normal and exotic nuclei [102]. The value of neutron-skin thickness in ^{208}Pb nucleus was also considered one of the fit data. The value of neutron-skin thickness in ^{208}Pb was varied over a wide range of $0.16-0.28$ fm as it is not yet well constrained. In total, there are twenty-one parameter sets, seven parameter sets for each of the families of the ERMF model corresponding to different values of neutron-skin thickness in ^{208}Pb. These parameter sets were named as BSR1, BSR2,...,BSR21 [101, 102]. The various properties of the symmetric nuclear matter associated with the BSR1 - BSR21 forces lie in a narrow range. For instance, the binding energy per nucleon for the symmetric nuclear matter $B/A = 16.11 \pm 0.04$ MeV, the nuclear matter incompressibility $K_0 = 230.24 \pm 9.80$ MeV, the nucleon effective mass $M^*/M = 0.605 \pm 0.004$ and the saturation density $\rho_0 = 0.148 \pm 0.003$ fm^{-3}. The quality of the fit to the bulk properties of the finite nuclei are also nearly the same for all the BSR forces; the rms errors on the total binding energy and the charge radii are 1.5 - 1.8 MeV and $0.025 - 0.04$fm, respectively, for the nuclei considered in the fit. Hereafter, the parameter sets BSR1 - BSR7 with $\zeta_0 = 0$, BSR8 - BSR14 with $\zeta_0 = 0.03g_\omega^2$ and BSR15 - BSR21 with $\zeta_0 = 0.06g_\omega^2$, will be referred to as F1, F2 and F3 families of the ERMF models, respectively. The maximum mass for the neutron star for these three families of interaction lie in the range of 1.7 - 2.4 $M_\odot$. The highest (lowest) values of maximum mass are obtained for F1(F3) families. The variation in the maximum mass of the neutron star across the families is predominantly due to the change in the values for the self-coupling of the ω-mesons. The maximum mass increases only by $\sim 0.03M_\odot$ is due to the change in the density dependence of the symmetry energy caused by the increase in neutron-skin thickness from 0.16 to 0.28 fm for the ^{208}Pb nucleus. As the neutron-skin thickness of ^{208}Pb nucleus is strongly correlated with the symmetry energy slope parameter [27], the different families of systematically varied parameterizations can be used to assess the model dependence and the symmetry energy dependence on the core-crust transition properties. For the sake of comparison, we also consider commonly used RMF parameterizations such as NL3 [79], FSU [107], TM1 [108] and GM1 [3]. To this end, we would like to mention that the predictions for the finite nuclei and nuclear matter around saturation density for the non-linear RMF model considered here are more or less the same as those for the other variant, like, point coupling and density dependent meson exchange models [109–111]. We have considered the RMF model which includes cross-coupling between various mesons and the self-coupling of ω-mesons in addition to the conventionally present cubic and quartic terms for the self-coupling of the σ-mesons. The results for such RMF models [112] are consistent with the trends obtained by Dirac-Brueckner-Hartree-Fock calculations at densities away from the saturation region.

3.3 Results for Core-crust transition properties

The values of the core-crust transition density are calculated in the present work using the RPA method as described briefly in Sec. 2.3.2. The symmetry energy $S(\rho)$, slope $L(\rho)$ and curvature $K_{\rm sym}(\rho)$ can be defined as,

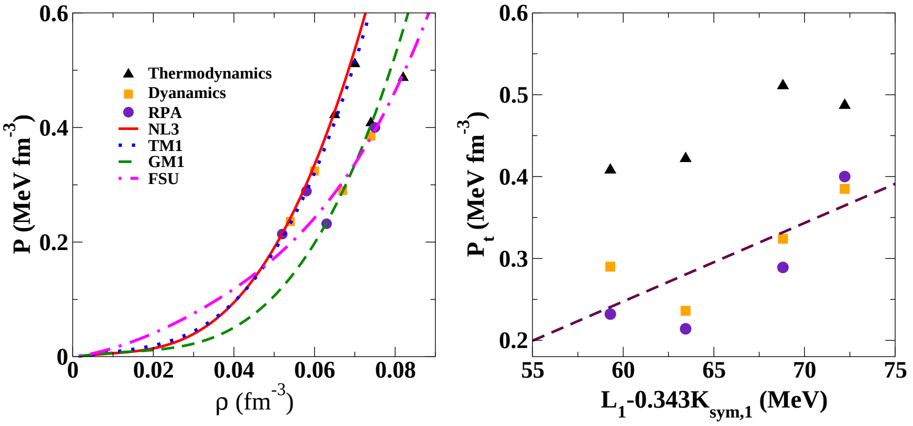

Figure 3.1: Plots for the EoSs for the β-equilibrated matter obtained using the NL3, FSU, TM1 and GM1 parameterizations of the RMF model (lower panel). The filled circles represent core-crust transition density ρ_t and the corresponding pressure P_t calculated using RPA method. For the sake of comparison, the values of ρ_t and P_t obtained using thermo-dynamical (filled triangles) and dynamical methods(filled squares) of Ref. [70] are also shown. The P_t as a function of $L_1 - 0.343K_{\mathrm{sym},1}$ are plotted in the upper panel, where, L_1 and $K_{\mathrm{sym},1}$ represent the values of values of $L(\rho)$ and $K_{\mathrm{sym}}(\rho)$ at $\rho = 0.01$ fm^{-3}, respectively. The dash line is taken from Ref. [70].

$$S(\rho) = \frac{1}{2}\left.\frac{d^2 e(\rho,\delta)}{d\delta^2}\right|_{\delta=0}, \tag{3.1}$$

$$L(\rho) = 3\rho\frac{dS(\rho)}{d\rho}, \tag{3.2}$$

$$K_{\mathrm{sym}}(\rho) = 9\rho^2\frac{d^2S(\rho)}{d\rho^2}, \tag{3.3}$$

$$\tag{3.4}$$

where, $e(\rho, \delta)$ is the energy per nucleon at a given density ρ and asymmetry $\delta = (\rho_n - \rho_p)/\rho$. In the following discussions, the J_0, L_0 and $K_{\mathrm{sym},0}$ represent the symmetry energy $S(\rho)$, its slope $L(\rho)$ and curvature parameter $K_{\mathrm{sym}}(\rho)$ evaluated at the saturation density ρ_0, whereas, J_X, L_X and $K_{\mathrm{sym,X}}$ denote their values at $\rho = 0.X$ fm^{-3}.

The fractions of the particles of different species in the neutron star matter are determined by charge neutrality and beta equilibrium conditions.

It is instructive to compare the core-crust transition properties calculated within

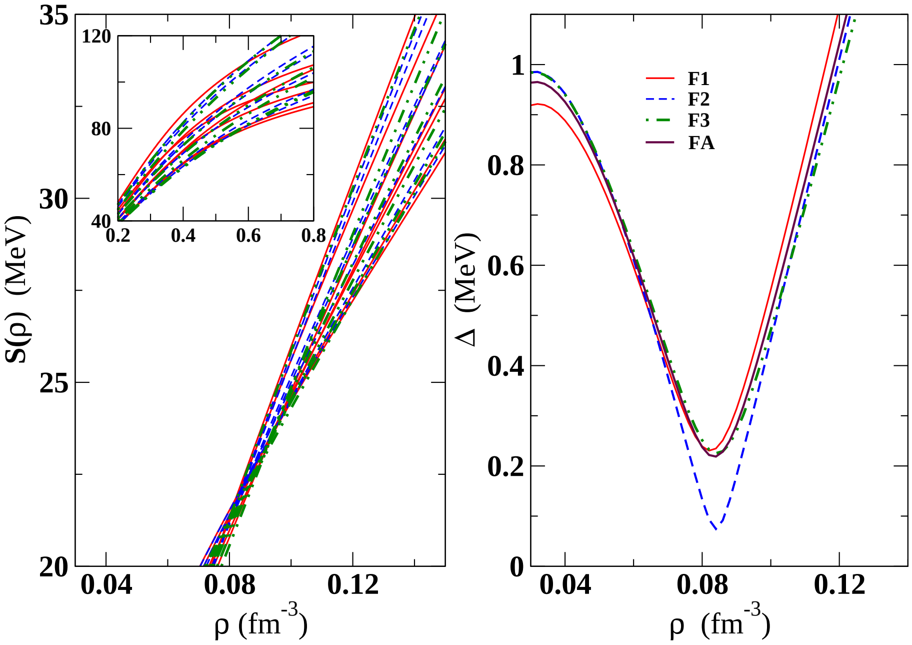

Figure 3.2: The density dependence of the symmetry energy coefficient $S(\rho)$ for various ERMF models (left panel) and the variance Δ calculated using Eq. (3.5) (right panel). The labels F1, F2 and F3 represent three different families of the ERMF models, whereas, FA correspond to the results obtained by combining all the three families. In the inset, the high density behaviour of $S(\rho)$ are plotted for some selected forces from the F1,F2 and F3 families.

the RPA method with those obtained from commonly used thermo-dynamical and dynamical methods. We plot in Fig. 3.1, the low density behavior for the EoS for β-equilibrated matter (lower panel) obtained using NL3, FSU, TM1 and GM1 parameterizations of the RMF model. The solid symbols mark the values of the core-crust transition density ρ_t and the corresponding pressure P_t which are obtained using dynamical (squares), thermo-dynamical (triangles) and RPA (circles) methods. The values of ρ_t and P_t calculated within the RPA method seem to be close to the ones obtained within the dynamical method. The values of ρ_t and P_t calculated using the thermo-dynamical method are somewhat higher. The values of P_t are plotted as a function of $L_1 - 0.343K_{\text{sym},1}$ in the upper panel. The dash line is taken from Ref. [70], which is obtained by using the values of P_t calculated from dynamical method. It can be seen that our values of P_t calculated within the RPA method are more or less consistent with the linear correlation as shown by the dashed line.

Before embarking on our main results, let us look into the general trends of the density dependence of symmetry energy for the various ERMF models considered. In the left panel of Fig. 3.2, we plot the symmetry energy as a function of density. For the sake of completeness, the high density behaviour of $S(\rho)$ are plotted for some selected forces from the F1,F2 and F3 families is plotted in the inset. These selected forces correspond to the neutron-skin thickness around 0.16, 0.22 and 0.28 fm in ^{208}Pb nucleus. The variance Δ for $S(\rho)$ is plotted in the right panel. The labels $F1$, $F2$ and $F3$ denote three different families, while, FA corresponds to the results obtained by combing all the three families. The values of $S(\rho)$ at densities in the range of $0.08 - 0.09$ fm^{-3} seems to be more or less same for all the different models. The variance Δ at a given density is obtained using,

$$\Delta^2 = \frac{1}{n} \sum (S(\rho) - \bar{S}(\rho))^2 \tag{3.5}$$

where, n is the number of models and $\bar{S}(\rho)$ is the average value at a density ρ. The variance has a minimum at $\rho \approx 0.08$fm^{-3} which is smaller than 0.11fm^{-3} as obtained for a set of SHF and RMF forces [70].

We now consider the core-crust transition properties obtained using three different families of the ERMF models. In Fig. 3.3, we display the low density behavior of the EoS for β-equilibrated matter for these ERMF models. For the sake of clarity we plot the results only for a few selected forces for each of the families. The dotted lines correspond to the results for the BSR1, BSR8 and BSR15 forces belonging to the F1 (red), F2 (blue) and F3 (green) families. Likewise, the dashed correspond to BSR4, BSR11, BSR18 and solid lines are for BSR7, BSR14, BSR21. All the dotted, dashed and solid lines correspond to the forces associated with the neutron-skin thickness in ^{208}Pb to be around 0.16, 0.22 and 0.28 fm, respectively. At low densities, $\rho \sim 0.03$ fm^{-3}, the behavior of the EoS is more or less independent of the choice of the model

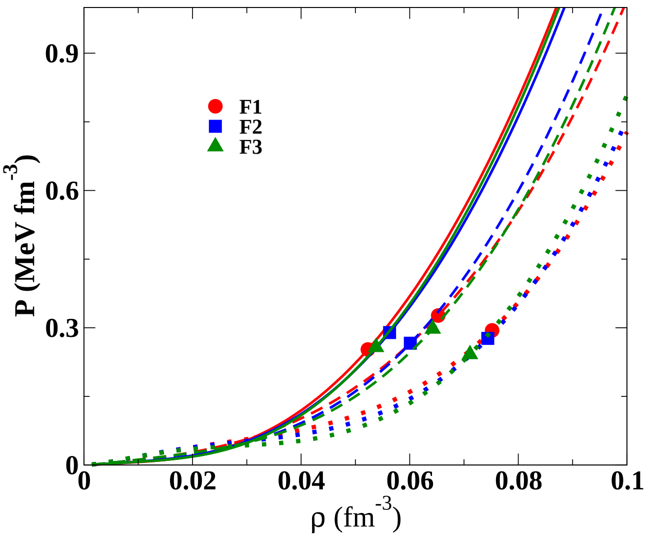

Figure 3.3: Plots for the EoSs for the β-equilibrated matter in terms of pressure verses density for the three different families of the ERMF model: F1 (red), F2 (blue) and F3 (green). The solid symbols mark the values of transition density ρ_t and the corresponding pressure P_t calculated within the RPA method. For the clarity, the results for only three forces for each of the families are plotted: BSR1, BSR8, BSR15 (dotted), BSR4, BSR11, BSR18 (dashed) and BSR7, BSR14, BSR21 (solid) lines (see text for details).

and neutron-skin thickness in ^{208}Pb. With further increase in the density, the EoS show stronger dependence on the choice of the neutron-skin thickness. For instance, BSR1, BSR8 and BSR15 (dotted lines) correspond to the different families but have almost the similar values of J_0, L_0 and neutron-skin thickness. We see that the EoSs associated with similar neutron-skin thickness depend weakly on the choice of the families of the models. One may thus expect the values of ρ_t and P_t depend not only on the J_0 and L_0, but, also on the choice of the models. In other words, the core-crust transition properties may show some model dependence in addition to their dependence on the symmetry energy parameters J_0 and L_0.

The values of ρ_t obtained using ERMF models are shown in Fig. 3.4 as a function of J_0 (left panel) and slope parameter L_0 (right panel). The values of ρ_t are correlated with the J_0 and L_0. The $\rho_t - L_0$ correlations is stronger than the $\rho_t - J_0$ correlations. The $\rho_t - J_0$ correlation is stronger within the same family. But, $\rho_t - L_0$ correlations are almost model independent. This is in conformity with the earlier works [70,105].

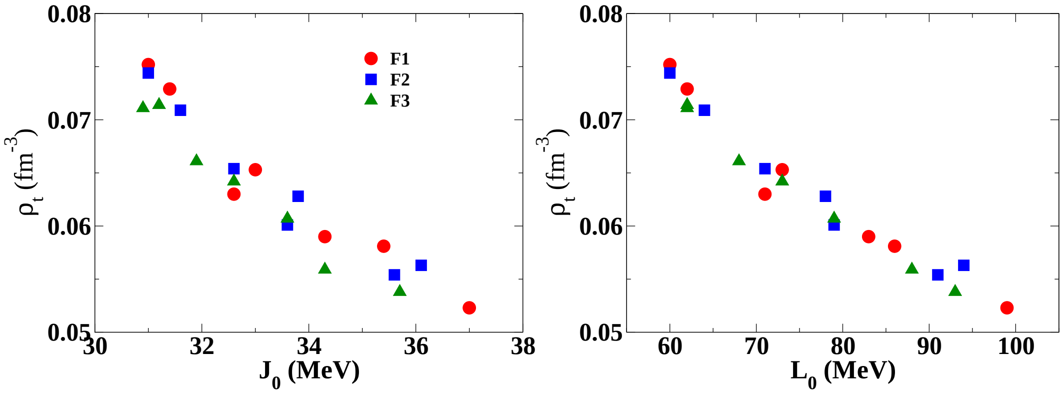

Figure 3.4: Plots for the ρ_t for neutron star matter as a function of symmetry energy J_0 (left panel) and its slope parameter L_0 (right panel) for 3 different families of the ERMF models.

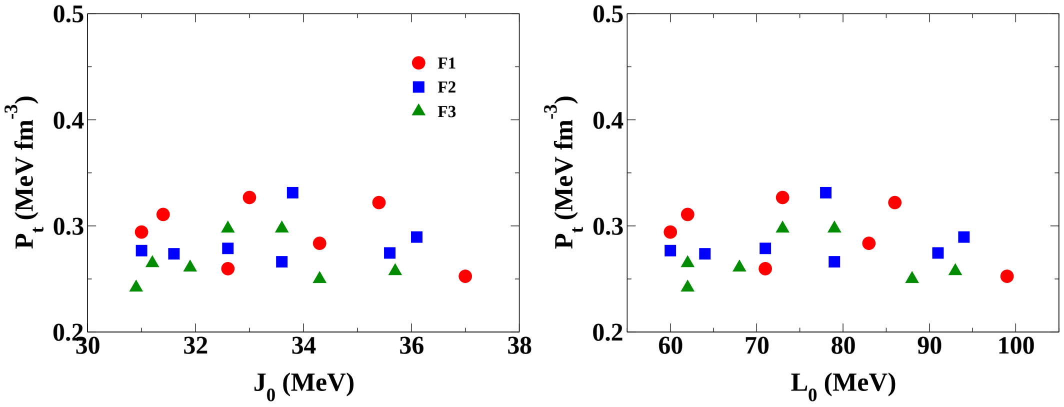

Figure 3.5: Plots for the P_t, for neutron star matter, as a function of J_0 (left panel) and L_0 (right panel) for 3 different families of the ERMF models.

In Fig. 3.5, we plot P_t for neutron star matter as a function of J_0 (left) and L_0 (right) panels for the ERMF models. Our results indicate P_t is not well correlated with J_0 and L_0. Consequently, P_t is not correlated with ρ_t. For the completeness, we list the values of correlation coefficient for ρ_t and P_t with J_0, L_0 and $K_{\text{sym},0}$ in Table 3.1. The J_0, L_0 and $K_{\text{sym}}, 0$ refer to their values at the saturation density. It is little too surprising that the $P_t - L_0$ correlations are weak even within the same family of the ERMF model, though, the various forces within the same family differ only in the density dependence of the $S(\rho)$. On the other hand, the calculations in Refs. [68, 105] based on a single model yield strong $P_t - L_0$ correlations.

We now explore the possibility of existence of strong correlations of P_t with $L(\rho)$,

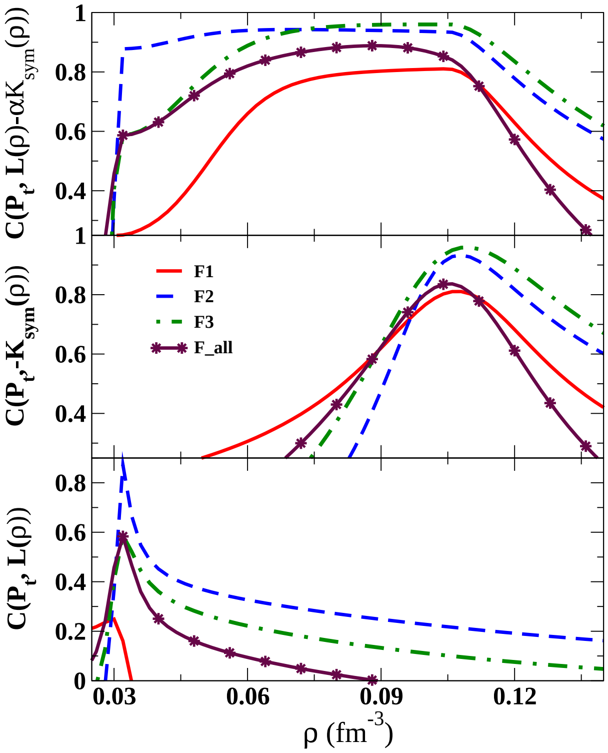

Figure 3.6: The correlation coefficients for the pressure P_t with $L(\rho)$ (lower panel), $K_{\rm sym}(\rho)$ (middle panel) and the linear combination $L(\rho) - \alpha K_{\rm sym}(\rho)$ (upper panel) as a function of the density for 3 different families of the ERMF models.

$K_{\rm sym}(\rho)$ and the linear combination $L(\rho) - \alpha K_{sym}(\rho)$ at sub-saturation densities ($\rho < \rho_0$). For the quantitative assessment, the Pearson's correlation coefficients between P_t and the various symmetry energy parameters are calculated as a function of density. Pearson's correlation coefficient $C(a, b)$ for a pair of variables a and b calculated for n number of different models is given as,

$$C(a,b) = \frac{\sigma_{ab}}{\sqrt{\sigma_{aa}\sigma_{bb}}} \tag{3.6}$$

where,

$$\sigma_{ab} = \frac{1}{n}\sum_i a_i b_i - \left(\frac{1}{n}\sum_i a_i\right)\left(\frac{1}{n}\sum_i b_i\right). \tag{3.7}$$

The values of $C(a, b)$ lie in the range of -1 to 1. If $|C(a, b)| = 1$ then, the variables a and b are fully linearly correlated, where as $C(a, b) = 0$ means, variables a and b

are uncorrelated or statistically independent.

It has been suggested in Ref. [70] that P_t is reasonably correlated with the linear combination of $L(\rho)$ and $K_{\rm sym}(\rho)$, with $\rho = 0.1 {\rm fm}^{-3}$. In Fig. 3.6 the correlations of P_t with $L(\rho)$ (lower), $K_{\rm sym}(\rho)$ (middle) and $L(\rho) - \alpha K_{sym}(\rho)$ (upper panels) are plotted as a function of density. The value of α is adjusted at a given density to maximize the correlation coefficient. The $P_t - L(\rho)$ correlations are strong at quite low densities for the F2 family of the ERMF models. These correlations become weak, once the results from all the different families of the models are combined. The P_t seems reasonably correlated with $K_{\rm sym}(\rho)$ as well as $L(\rho) - \alpha K_{\rm sym}(\rho)$ at some sub-saturation densities. The correlation coefficient $C(P_t, -K_{\rm sym})$ peaks at $\rho = 0.1$ fm^{-3}, whereas, $C(P_t, L(\rho) - \alpha K_{\rm sym}(\rho))$ peaks at $\rho = 0.09$ fm^{-3} for $\alpha = 1.31$. It is to be noted that the peaks in plots for the $C(P_t, L(\rho) - \alpha K_{\rm sym}(\rho))$ verses ρ are much wider than those for the $C(P_t, -K_{\rm sym}(\rho))$ verses ρ. The strong correlations of P_t with $K_{\rm sym}(\rho)$ at $\rho = 0.1$ fm^{-3} may be due the use of systematically varied models. In Fig. 3.7, we plot the values of P_t verses $K_{\rm sym}(\rho)$ (left panel) and P_t verses $L(\rho) - 1.31 K_{\rm sym}(\rho)$ (right panel), the values of $L(\rho)$ and $K_{sym}(\rho)$ are evaluated at the densities for which the $C(P_t, -K_{\rm sym})$ and $C(P_t, L - \alpha K_{\rm sym})$ correspond to their maximum values. Our results for the correlations of P_t with the linear combination of $L(\rho)$ and $K_{\rm sym}(\rho)$ agree only qualitatively with the ones obtained in Ref. [70]. Our values for the correlation coefficient $C(P_t, L(\rho) - \alpha K_{\rm sym}(\rho))$ is maximum at $\rho = 0.09 {\rm fm}^{-3}$, while, its value at $\rho = 0.1 {\rm fm}^{-3}$ is significantly smaller than those of Ref. [70]. We also observe that the variance or the spread in the values of $S(\rho)$ for the ERMF models considered in the present work is minimum at $\rho \sim 0.08 {\rm fm}^{-3}$ (see Fig. 3.2). Whereas, the variance of $S(\rho)$ for the set of SHF and RMF forces employed in Ref. [70] is minimum around $\rho = 0.11 {\rm fm}^{-3}$. Thus, it seems that the P_t is not correlated with the symmetry energy parameters in a model independent manner.

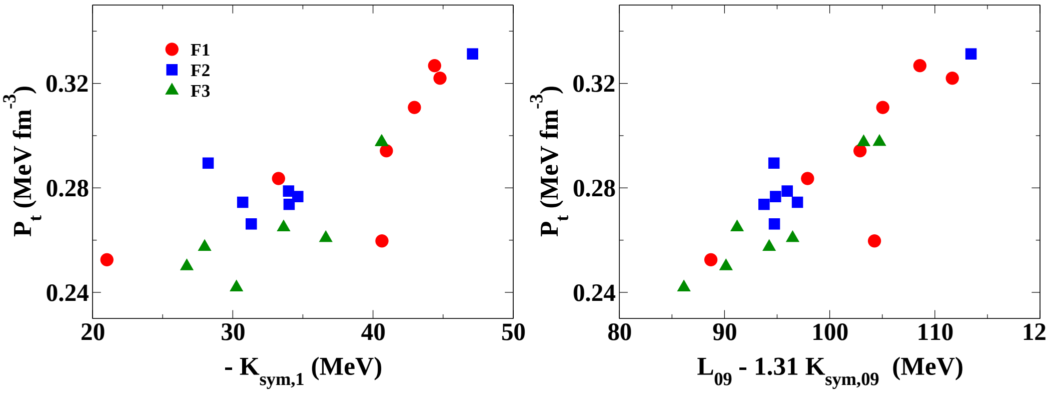

Figure 3.7: Plots for the pressure, P_t, at the transition density as a function of $K_{\rm sym,1}$ (left panel) and $L_{09} - 1.31K_{\rm sym,09}$ (right panel) for 3 different families of the ERMF models.

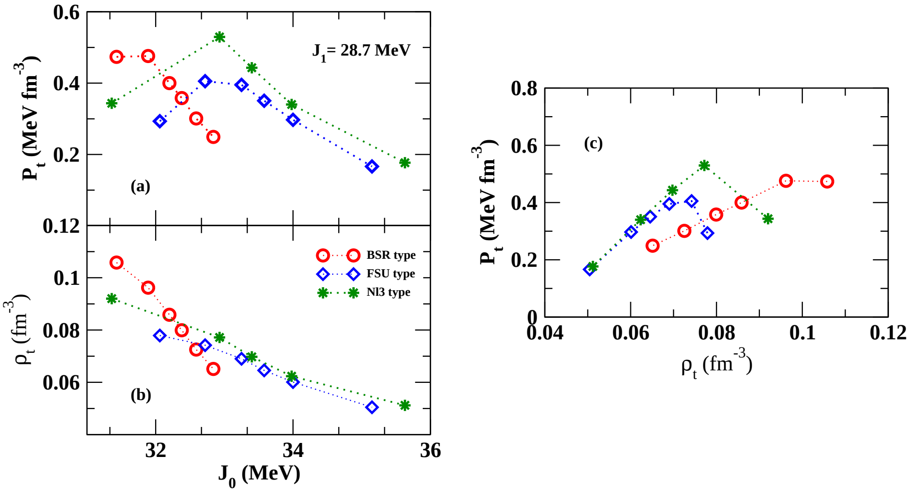

Figure 3.8: Plots for the ρ_t and P_t (left panel) as a function of J_1 and P_t verses ρ_t (right panel) that obtained using BSR1, FSU and NL3 type functional for the RMF model. The value of J_1 is varied at fixed $J_0 = 32.6$ MeV.

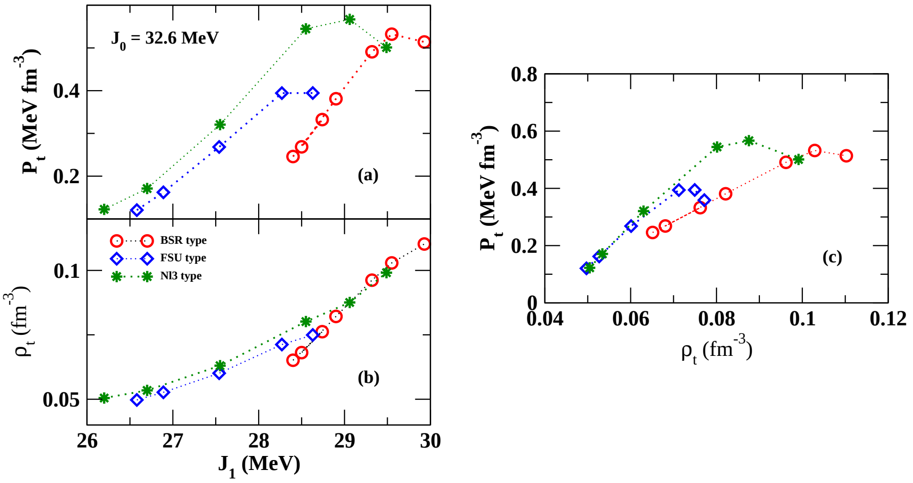

Figure 3.9: Same as that of 3.8, but, J_0 is varied at fixed $J_1 = 28.7$ MeV.

Table 3.1: The values of correlation coefficients $C(A, B)$ with A and B being the core-crust transition density ρ_t, corresponding pressure P_t and various symmetry energy parameters at the saturation density.

	F1	F2	F3	FA
$C(\rho_t, L_0)$	-0.970	-0.975	-0.994	-0.975
$C(\rho_t, J_0)$	-0.963	0.966	-0.985	-0.954
$C(\rho_t, K_{sym,0})$	0.645	0.879	0.813	0.643
$C(P_t, L_0)$	-0.363	0.157	0.049	-0.065
$C(P_t, J_0)$	-0.317	0.208	0.090	0.017
$C(P_t, K_{sym,0})$	-0.355	-0.545	-0.624	-0.130
$C(P_t, \rho_t)$	0.416	-0.108	-0.071	0.128

So far we have studied the correlations of ρ_t and P_t with J_0, $L(\rho)$ and $K_{\rm sym}(\rho)$ using different families of parameterizations of the ERMF model. Each of the parameterizations were obtained by fitting exactly same set of the experimental data for the bulk properties of finite nuclei except for the neutron-skin thickness. We shall now study the variations of ρ_t and P_t with J_0 and J_1 ($S(\rho)$ evaluated at $\rho = 0.1$ fm^{-3}) within a single model as it was done for DD-PC1 model [105]. For Our investigation, we have considered the BSR1, NL3 and FSU type of functionals for the RMF model. The desired values of J_0 and J_1 are obtained by adjusting the coupling parameters g_ρ and $\eta_{2\rho}$ appearing in Eqs. (2.43) and (2.45). In Fig. 3.8, we display the variations of ρ_t and P_t with J_1 for a fixed $a_{\rm sym} = 32.6$ MeV for the BSR1, NL3 and FSU parameterizations. Similarly, in Fig. 3.9, the variations of ρ_t and P_t with $a_{\rm sym}$ for a fixed $J_1 = 28.7$ MeV are displayed. In Table 3.2, we list the values of the correlation coefficient for ρ_t and P_t with J_0, and J_1. It is evident from the Figs. 3.8 and 3.9 and Table 3.2 that the ρ_t is correlated with J_0 as well as with J_1 , irrespective of the model used. Whereas P_t is strongly correlated only with J_1 in a model independent manner. The $P_t - J_0$ correlations are model dependent. For instance, the value of $|C(P_t, J_0)| \sim 0.95$ for the BSR1 type of model which reduces to ~ 0.6 for the NL3 and FSU type of models. We can thus say once again that the pressure at the transition density is correlated with the symmetry energy parameter

Table 3.2: Values for the various correlation coefficients obtained by varying J_0 or J_1 within a single model. Three different models, BSR1, FSU and NL3, are considered. The values of J_0 is varied by fixing $J_1 = 28.7$ MeV , while, J_1 is varied by fixing $J_0 = 32.6$ MeV. The values of correlation coefficients obtained by combining the results from all the three models are presented in the last column.

	BSR1	FSU	NL3	All
		J_0= 32.6 MeV		
$C(\rho_t, J_1)$	0.996	0.997	0.988	0.942
$C(P_t, J_1)$	0.956	0.947	0.952	0.879
$C(P_t, \rho_t)$	0.979	0.960	0.914	0.906
		J_1= 28.7 MeV		
$C(\rho_t, J_0)$	-0.995	-0.995	-0.983	-0.917
$C(P_t, J_0)$	-0.946	-0.659	-0.570	-0.612
$C(P_t, \rho_t)$	0.973	0.704	0.543	0.703

only at some sub-saturation density. We have also repeated our calculations for the variations of ρ_t and P_t with $J_0(J_1)$ by fixing $J_1(J_0)$ to different values. The results are qualitatively the same; $P_t - J_0$ correlations are model dependent.

3.4 Conclusions

The variations of core-crust transition properties in the neutron star with symmetry energy parameters are investigated using three different families of the systematically varied ERMF model. These families of the ERMF model mainly differ in the choice of the strength for the ω-meson self-coupling. Several parameterizations for each of the families are so considered that they yield wide variations in the density dependence of the symmetry energy.

Our results indicate that the transition density ρ_t is strongly correlated with the symmetry energy slope parameter L_0 at the saturation density which is in harmony with the earlier studies [70,105]. The ρ_t is also correlated with the symmetry energy at the saturation density, but, the correlations are marginally model dependent.

The pressure P_t at the transition density, however, does not show any meaningful correlations with the values of various symmetry energy parameters at the saturation density. The possibility of existence of strong correlations between the pressure at the transition point and the symmetry energy parameters evaluated at the sub-saturation density are explored. It is found that P_t is better correlated with the curvature parameter $K_{\rm sym}$ alone or with the linear combination of L and $K_{\rm sym}$, both the quantities calculated at some sub-saturation density. We observe that the density $\rho = 0.09$ fm^{-3} at which the correlation coefficient $C(P_t, L(\rho) - \alpha K_{\rm sym}(\rho))$ peaks is quite close to the one at which the variance of $S(\rho)$ is minimum. The strong correlations between P_t and linear combination of $L(\rho)$ and $K_{\rm sym}(\rho)$ at $\rho = 0.1$ fm^{-3} for a set of SHF and RMF models [70] for which the variance of $S(\rho)$ is minimum at $\rho = 0.11$fm^{-3} also supports our observation. Though, the pressure at the transition point is correlated with linear combination of the symmetry energy slope and the curvature parameters evaluated at a sub-saturation density, such correlations show some degree of model dependence.

We also study the dependence of core-crust transition properties on various symmetry energy parameters using a single model. In this case, the symmetry energy parameters are varied by modifying the values of the model parameters around their optimal values. Two different kinds of variations in the symmetry energy parameter $S(\rho)$ are considered. The values of $S(\rho)$ are varied at the saturation density by keeping its value fixed at the density $\rho = 0.1$ fm^{-3}. Another type of variations in $S(\rho)$ is obtained by changing its value at the density $\rho = 0.1$ fm^{-3}, but, keeping it fixed at the saturation density. The calculations are performed for the BSR1, NL3 and FSU type of the RMF model. The transition density is found to be strongly correlated with the values of $S(\rho)$ calculated at the saturation density as well as those at $\rho = 0.1$ fm^{-3}, irrespective of the model used. The pressure at the transition density is correlated in the model independent manner only with the $S(\rho)$ at the $\rho = 0.1$fm^{-3}. The correlations of pressure at the transition density with the

$S(\rho)$ at the saturation density are highly model dependent. It thus appears once again that the pressure at the transition density is at best correlated with symmetry energy parameters at some sub-saturation density.

CHAPTER 4

Influence of nuclear symmetry energy on various neutron star properties

4.1 Introduction

The matter inside the neutron star is highly asymmetric, thus, various properties of neutron stars depend strongly on the density dependence of nuclear symmetry energy. In this chapter, our main aim is to study the effects on the properties of neutron stars arising due to the isovector cross-coupling terms which determine the behaviour of symmetry energy in the extended relativistic mean field (ERMF) model. Towards this purpose, two different families of extended RMF models are obtained which mainly differ from each other in the choice for the cross-coupling term in the isovector part of the effective Lagrangian density. One of the families of models includes $\sigma - \rho$ cross-coupling while the other includes $\omega - \rho$ cross-coupling term in addition to the various linear and non-linear interaction terms already present in the commonly used RMF models. The contributions due the coupling of the δ mesons to the nucleons are also considered. These models give different behaviour in the density dependence of symmetry energy leading to different values in the neutron-skin thickness in ^{208}Pb nucleus, since, the neutron-skin thickness in a heavy nucleus ,which can be experimentally measured, is found to be strongly correlated to density dependence of the symmetry energy around the saturation density . The neutron-skin thickness $\Delta r_{\rm np}$ ($\equiv \langle r^2\rangle_n^{1/2} - \langle r^2\rangle_p^{1/2}$) is the difference between the rms radii for density distributions of the neutrons and protons in a nucleus. Recently [68, 113], the correlations of the neutron-skin thickness in ^{208}Pb nucleus with several bulk properties of neutron stars have been examined for the TOV-min and FSU type models. The energy density functional for the TOV-min corresponds to the Skyrme type effective force and that for FSU is based on the extended RMF model. The correlation between neutron-skin thickness in ^{208}Pb nucleus and the neutron star radius $R_{1.4}$ for TOV-min is noticeably smaller than the one obtained for the FSU model. Consequently, for the case of TOV-min the properties of neutron stars can have larger variations at a fixed neutron-skin in ^{208}Pb nucleus. This result is in concordance with the large uncertainties in the high density behaviour of the symmetry energy for the Skyrme type energy density functionals [114].

Here, we would like to investigate the correlations of different neutron stars properties with the neutron skin thickness in heavy nucleus which is strongly correlated to the slope of symmetry energy. The various neutron star properties considered are the core-crust transition density, radius for the neutron stars with canonical mass, the tidal polarizability parameter and the threshold mass required for the enhanced cooling through direct Urca process. Some of these neutron stars properties at a fixed neutron-skin thickness differ significantly for two different families of the models.

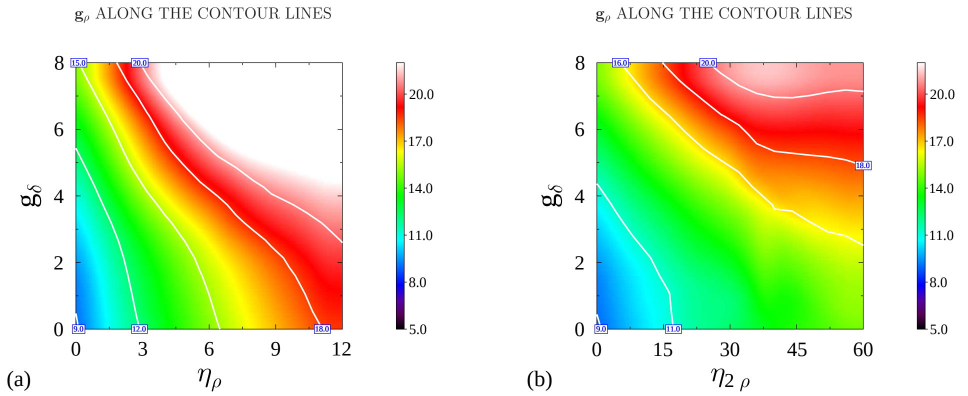

Figure 4.1: Colour coded contours in the $g_\delta - \eta_\rho$(left panel) and $g_\delta - \eta_{2\rho}$(right panel) planes corresponding to the F_ρ and $F_{2\rho}$ families, respectively. The value of g_ρ are colour coded according to the scale one the right side.

4.2 Model parameters

Two different families of the extended RMF models, named hereafter as F_ρ and $F_{2\rho}$, are obtained. These families differ from each other in the choice for the cross-coupling term in the isovector part of the Lagrangian density. The isovector part of the Lagrangian density for the $F_\rho(F_{2\rho})$ family is governed by the coupling parameters g_ρ, g_δ and $\eta_\rho(\eta_{2\rho})$. The parameters g_ρ and g_δ denote the strengths for the coupling of the ρ and δ mesons to the nucleons, respectively. The parameter η_ρ and $\eta_{2\rho}$ denote the strength of the $\sigma - \rho$ and $\omega - \rho$ cross-couplings as can be seen from Eq. (2.45). The remaining parameters which correspond to the isoscalar part of the Lagrangian density and the mass of the σ, ω and ρ mesons are kept fixed to that of the BKA22 model [101]. The BKA22 model has been identified to satisfy various constraints related to symmetric nuclear matter, pure neutron matter, symmetry energy, and its derivatives [115].

The different parameterizations of $F_\rho(F_{2\rho})$ families are obtained by varying appropriately the values of g_ρ, g_δ and $\eta_\rho(\eta_{2\rho})$. For a given value of g_δ and $\eta_\rho(\eta_{2\rho})$, the value of g_ρ is always adjusted to yield appropriate binding energy for the ^{208}Pb nucleus.

Table 4.1: The parameters of the isovector part of the Lagrangian density for some representative sets for the F_ρ and $F_{2\rho}$ families of models. In the bottom part, the values for the symmetry energy coefficient at the saturation density J_0, symmetry energy slope parameter L_0, effective mass for the protons and neutrons and their differences are also presented. All these quantities are in MeV.

	F_ρ		$F_{2\rho}$	
Parameter	SET1	SET2	SET3	SET4
η_ρ	4.0	4.0	0.0	0.0
$\eta_{2\rho}$	0.0	0.0	17.5	17.5
g_δ	0.0	8.0	0.0	8.0
g_ρ	13.033	21.863	11.051	18.556
J_0	33.3	30.9	33.0	30.2
L_0	79.0	62.5	65.0	23.3
M_p^*	570.1	630.9	577.8	652.4
M_n^*	570.1	495.4	577.8	515.8
ΔM_{pn}^*	0.0	135.5	0.0	136.6

Table 4.2: The values of the total binding energy (E) in MeV, charge radii (r_c), neutron radii (r_n) and neutron-skin thickness $\Delta r_{\rm np}$ in fm for a few asymmetric spherical nuclei obtained for SET1 - SET4 parameters. Experimental values of their binding energy and charge radii are also presented.

		F_ρ		$F_{2\rho}$		
Nucleus	Property	SET1	SET2	SET3	SET4	Expt.
^{48}Ca	E	-415.75	-415.40	-415.81	-415.61	-416.00
	r_c	3.468	3.484	3.465	3.477	3.477
	r_n	3.575	3.544	3.574	3.535	–
	$\Delta r_{\rm np}$	0.201	0.153	0.202	0.151	–
^{132}Sn	E	-1102.49	-1100.37	-1102.69	-1100.99	-1102.84
	r_c	4.736	4.759	4.727	4.731	4.709
	r_n	4.952	4.901	4.934	4.873	–
	$\Delta r_{\rm np}$	0.284	0.210	0.286	0.210	–
^{208}Pb	E	-1637.07	-1637.08	-1637.06	-1637.05	-1636.43
	r_c	5.545	5.566	5.535	5.538	5.501
	r_n	5.706	5.659	5.699	5.631	–
	$\Delta r_{\rm np}$	0.219	0.151	0.221	0.151	–

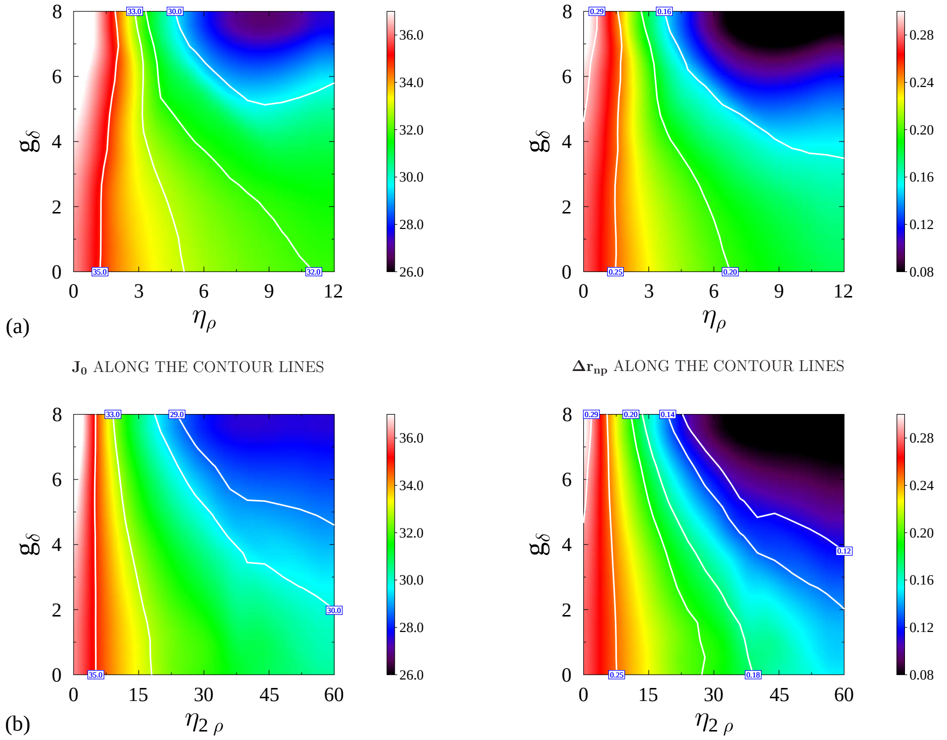

Figure 4.2: Same as Fig. 4.1, but, for the symmetry energy at the saturation density ($J_0 = S(\rho_0)$) (left panel) and the neutron-skin thickness $\Delta r_{\rm np}$ in the ^{208}Pb nucleus (right panel) fixed along the contour. The values of J_0 are in MeV.

Once the values of g_δ, g_ρ and η_ρ or $\eta_{2\rho}$ are known, the properties of the nuclear matter and the finite nuclei can be computed. We vary the values of g_δ over a wide range from 0 to 8. The values of η_ρ and $\eta_{2\rho}$ are varied in the range of $0 - 12$ and $0 - 60$, respectively. For $\eta_\rho > 12$, the stable solutions of the field equations for the mesons could not be obtained. We have constructed 22 different parameterizations of the F_ρ and 41 different parameterizations of the $F_{2\rho}$ families.

The Fig. 4.1 displays the relationship between the various parameters of the isovector channel for the F_ρ and $F_{2\rho}$ families of the models. It can be readily seen that the value of g_ρ, required to reproduce the binding energy for the ^{208}Pb nucleus, increases with g_δ, η_ρ and $\eta_{2\rho}$. In other words,the equation of state at least for the densities relevant for the finite nuclei becomes softer with the increase in the g_δ, η_ρ and $\eta_{2\rho}$, which is compensated by increasing the value of g_ρ to reproduce the binding energy

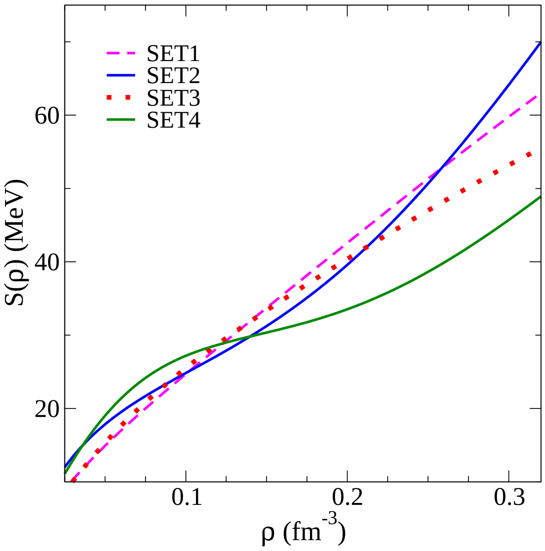

Figure 4.3: The density dependence of symmetry energy $S(\rho)$ for some representative cases of F_ρ and $F_{2\rho}$ families of the models. The labels SET1 and SET2 correspond to the two different parameterizations for the F_ρ family, whereas, the SET3 and SET4 correspond to the $F_{2\rho}$ family. The SET1 and SET3 are associated with $\Delta r_{\rm np} = 0.22$fm and the SET2 and SET4 yield $\Delta r_{\rm np} = 0.15$fm (see also Tables 4.1 and 4.2).

for the ^{208}Pb nucleus. In the left panel of Fig. 4.2, the relationship of the parameters g_δ and $\eta_\rho(\eta_{2\rho})$ with the symmetry energy coefficient at the saturation density ($J_0 = S(\rho_0)$) for the $F_\rho(F_2\rho)$ is displayed in terms of the contour plots. Similarly, the results for the $\Delta r_{\rm np}$ in the ^{208}Pb nucleus are plotted in the right panel of Fig. 4.2. In general, the values of J_0 and $\Delta r_{\rm np}$ decreases with increasing g_δ, η_ρ or $\eta_{2\rho}$. The $F_{2\rho}$ model yields larger variations in $\Delta r_{\rm np}$. The large values for η_ρ are not favored, as a result the F_ρ family can yield very small values of $\Delta r_{\rm np}$ only with the inclusion of the δ mesons. In Table 4.1 the values of the parameters for four representative sets corresponding to the F_ρ and $F_{2\rho}$ models are listed. The SET1 and SET2 belong to the F_ρ family, while, SET3 and SET4 are for the $F_{2\rho}$ family. The SET1 and SET3 do not include the contributions from the δ mesons ($g_\delta = 0$). The SET2 and SET4 correspond to the highest value of the δ-nucleon coupling strength ($g_\delta = 8$), otherwise, they are very much similar to the SET1 and SET3, respectively. These different sets are so chosen that the comparison of the properties of the neutron stars resulting from them would give us a crude estimate about the effects of δ meson as well as the $\sigma - \rho$ and $\omega - \rho$ cross-couplings. In the bottom part of Table 4.1, the values of the symmetry energy coefficient at the saturation density $J_0 = S(\rho_0)$), symmetry energy slope parameter ($L_0 = \left(3\rho\frac{\partial S(\rho)}{\partial \rho}\right)_{\rho_0}$), proton and neutron effective masses and their differences are also presented. The effective masses are obtained at the maximum asymmetry, i.e., the pure neutron matter. In Table 4.2, we present some bulk properties of a few asymmetric spherical nuclei. The various bulk properties for these nuclei are relatively better reproduced for the SET1 and SET3 parameters which corresponds to $\Delta r_{\mathrm{np}} \sim 0.22$fm in the ^{208}Pb nucleus, since, this value of Δr_{np} is almost the same as that of the base model BKA22. It may be noted that the $\Delta r_{\mathrm{np}} = 0.22$ fm for the SET1 and SET3, but, they belong to different families. Similarly, SET2 and SET4 represent different families, with $\Delta r_{\mathrm{np}} = 0.15$ fm.

Let us now take a look at the density dependence of the symmetry energy for the different parameterizations of the F_ρ and $F_{2\rho}$ families corresponding to equal values of Δr_{np}. In Fig. 4.3, we display the variations of symmetry energy as a function of density for different parameterizations as indicated by SET1, SET2, SET3 and SET4. The high density behaviour for the symmetry energy is stiffer for the F_ρ family as can be easily verified by comparing the results for the SET1 and SET2 with those for the SET3 and SET4, respectively. Further, by comparing the results for the SET1 with SET2 or those for SET3 with SET4, it can be concluded that the inclusion of the δ mesons softens the symmetry energy at low densities while makes it stiffer at higher densities. The results depicted in Fig. 4.3 provide evidences a priori about the possibilities of the differences in the properties of neutron stars at a fixed Δr_{np} across the different families of the models, due to the differences in the high density behaviour of the symmetry energy.

4.3 Neutron-skin thickness and Neutron Stars properties

The neutron skin thickness Δr_{np} is defined as the difference between the neutron and proton root mean square radii of a nucleus. Hence, it is expected that the Δr_{np} should be sensitive to the pressure difference between protons and neutrons in a nucleus, which is further related to the slope of symmetry energy. Recently, many studies establish this connection [27, 65, 116]. On the other hand, the density dependence of symmetry energy also plays a crucial role in determining the bulk properties of highly asymmetric dense objects like neutron stars. Therefore, the symmetry energy dependence of the neutron star properties can be explored through analyzing their dependence on the neutron skin thickness. We wish to study the differences in the properties of neutron stars for the F_ρ and $F_{2\rho}$ families of the models at fixed values for the neutron skin thickness Δr_{np} in the ^{208}Pb nucleus. In particular, attention is given to the study of such differences at $\Delta r_{\text{np}} = 0.15$fm in ^{208}Pb nucleus. This value of Δr_{np} is consistent with $0.156^{+0.025}_{-0.021}$ fm [117] and 0.168 ± 0.022 fm [98] as extracted from the experimental data on the dipole polarizability for ^{208}Pb nucleus. A very recent measurement of coherent pion photo-production [118] also corresponds to $\Delta r_{\text{np}} = 0.15 \pm 0.03$ fm in ^{208}Pb nucleus. However, these measurements do not conclusively yet rule out the larger values for Δr_{np}, since, the Lead Radius Experiment (PREX) [71, 119, 120] has recently measured $\Delta r_{\text{np}} = 0.33^{+0.16}_{-0.18}$ fm in ^{208}Pb nucleus via parity-violating electron scattering which provides the first purely electroweak, almost model independent estimate. The PREX experiment measures the parity-violating asymmetry A_{PV} which is strongly correlated with the neutron rms radius R_n of ^{208}Pb. The follow-up measurement PREX II aims to measure R_n of ^{208}Pb more precisely with 1% accuracy. Combining the results with the well-known charge radii of these nuclei will provide a measurement of the neutron skin

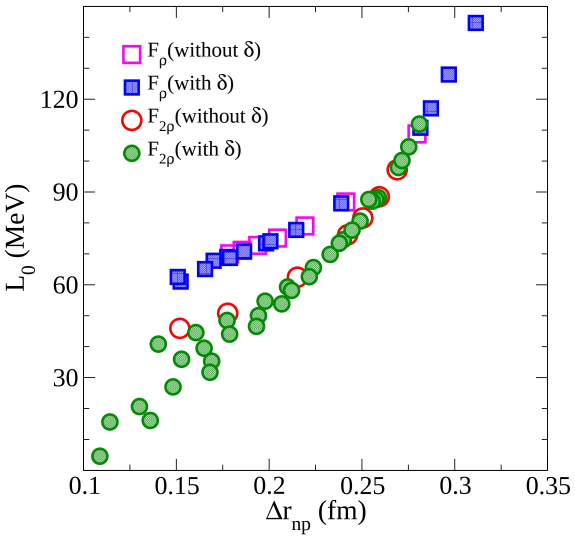

Figure 4.4: The variations of symmetry energy slope parameter L_0 with neutron-skin thickness Δr_{np} in the ^{208}Pb nucleus for the F_ρ and $F_{2\rho}$ families of models. The solid and hollow symbols represent the results obtained with ($g_\delta \neq 0$) and with ($g_\delta = 0$), respectively.

of ^{208}Pb with 0.06 fm accuracy [121–123]. This measurement will be free from many of the strong interaction uncertainties present in the other measurements. As the correlation between the neutron skin thickness in heavy nucleus and the slope of symmetry energy at saturation density is well-established, such accurate measurement of Δr_{np} will provide a tighter bound on the density dependence of symmetry energy.

We shall give quantitative estimates about the extent to which the various properties of the neutron stars might vary across the different families of the models for a plausible value of neutron-skin thickness. The various properties for the neutron stars considered are the core-crust transition density, radius, red-shift, the threshold mass required for the enhance cooling through the direct Urca process and the tidal polarizability parameter. The comparison of results for the F_ρ and $F_{2\rho}$ families of the models would enable us to understand the role of different cross-coupling terms. We shall also assess the effects of the δ mesons by comparing the results obtained with and without its inclusion in the same family of the models.

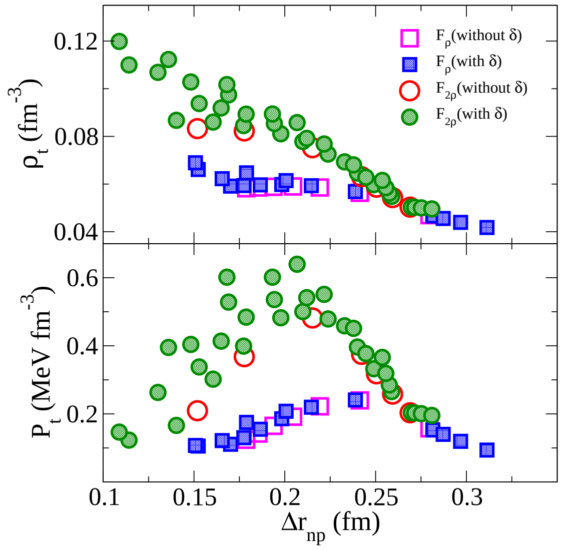

Figure 4.5: The variation of core-crust transition density and the corresponding pressure with the neutron-skin thickness $\Delta r_{\rm np}$ in ^{208}Pb nucleus for the F_ρ and $F_{2\rho}$ families of the extended RMF models.

The values of the neutron-skin thickness in a heavy nucleus, according to the Droplet Model [124], are strongly correlated with the symmetry energy slope parameter L_0. The dependence of L_0 on $\Delta r_{\rm np}$ in ^{208}Pb for the F_ρ and $F_{2\rho}$ families of the models are displayed in Fig. 4.4. It may be pointed out that the similar values of $\Delta r_{\rm np}$ can be obtained within a given family by varying appropriately the values of coupling parameters g_δ and η_ρ or $\eta_{2\rho}$(see also the right panel of Fig. 4.2). The solid and the hollow symbols represent the results obtained with and without the contributions from the δ mesons, respectively. The values of $\Delta r_{\rm np}$ are well correlated with L_0 within a given family of the models irrespective of the contributions from the δ mesons. However, the values of L_0 for the two families of the models differ significantly at smaller $\Delta r_{\rm np}$. This difference gradually disappears as $\Delta r_{\rm np}$ increases.

The values of core-crust transition density ρ_t and the corresponding pressure P_t as a function of $\Delta r_{\rm np}$ obtained for F_ρ and $F_{2\rho}$ families of models are plotted in Fig. 4.5. The values of ρ_t are obtained using a method based on the relativistic random-phase approximation [89, 125–127]. This method uses the fact that the uniform

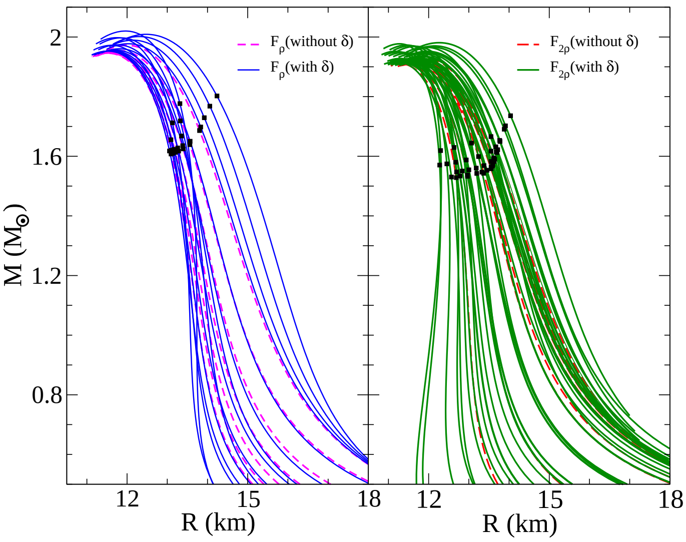

Figure 4.6: The mass-radius relationship for the F_ρ and $F_{2\rho}$ families of the models. The solid squares represent the masses and the corresponding radii for the neutron stars with the central density to be $3\rho_0$.

matter in its ground state at sufficiently low densities becomes unstable to small density fluctuations. The values of ρ_t are correlated with the $\Delta r_{\rm np}$ within a same family irrespective of the contributions from the δ mesons. But, this correlation seems to be some what model dependent— the values of ρ_t for both the families of models at a fixed $\Delta r_{\rm np}$ are not the same. In particular, the ρ_t is significantly larger for the $F_{2\rho}$ family at smaller $\Delta r_{\rm np}$. The transition pressure P_t is not very well correlated with the $\Delta r_{\rm np}$. Initially, the P_t increases with $\Delta r_{\rm np}$ and it decreases for higher values of $\Delta r_{\rm np}$.

Once, the core-crust transition density is determined, the EoS for various density ranges as required for the computation of the properties of the neutron stars can be constructed. The EoS data for the density $\rho \sim 4.8 \times 10^{-9} - 2.6 \times 10^{-4}{\rm fm}^{-3}$ corresponding to the outer crust region are taken from Ref. [128]. The EoS for the inner crust is obtained by assuming a polytropic form $P(\epsilon) = a + b\epsilon^{4/3}$, where P and ϵ are the pressure and energy density respectively. The constants a and b are determined in such a way that the EoS for the inner crust matches with that for the inner edge of the outer crust at one end and with the edge of the core at the other end. The EoSs for the core region, $\rho > \rho_t$, are obtained within the RMF model by using the different parameterizations of the F_ρ and $F_{2\rho}$ families. The core region is assumed to be composed of neutrons, protons, electrons and muons. The chemical potentials for various particle species at a given baryon density are obtained by imposing the β-equilibrium and charge neutrality conditions. We use these EoSs to compute the properties of static neutron stars by integrating the Tolman-Oppenheimer-Volkoff (TOV) equations [129]. In Fig. 4.6 we display the mass-radius relationship for the sequences of static neutron stars obtained for the F_ρ and $F_{2\rho}$ families of models. The solid and the dashed lines depict the results obtained with and without the inclusion of the contributions from the δ mesons, respectively. The solid squares represent the masses and the corresponding radii for the neutron stars with the central density to be $3\rho_0$. The different EoSs obtained for a given family of the models differ mainly in the high density behaviour of the symmetry energy. This leads to the variations in the mass-radius relationship for the neutron stars within the same family of the models.The maximum mass $M_{\rm max} = 1.95 - 2.02 M_\odot$ and $1.91 - 1.98 M_\odot$ and the radii $R_{1.4} = 13.3 - 15.4$km and $12.3 - 14.9$km for the F_ρ and $F_{2\rho}$ families, respectively. The value of $M_{\rm max}$ for the F_ρ family is consistent with the recent mass measurements $M = 1.97 \pm 0.04 M_\odot$ for PSR J1614-2230 [18] and $M = 2.01 \pm 0.04 M_\odot$ for PSR J0348+0432 [19], but, the values for $R_{1.4}$ is marginally away from the $R_{1.4} = 10.7 - 13.1$km as extracted in Ref. [95]. For the $F_{2\rho}$ family, values for $M_{\rm max}$ are barely consistent with the recent measurements, but, $R_{1.4}$ is consistent with the ones extracted in Ref. [95]. The inclusion of the δ mesons yields higher values for the maximum mass for the neutron stars within a family. A more realistic estimation for the effects of δ mesons on the maximum mass of the neutron stars requires the inclusion of various exotic degrees of freedom. Since, the density at the center of the neutron star with the maximum mass for our EoSs is significantly larger than $3\rho_0$.

We now compare the various properties of the neutron stars at fixed values of $\Delta r_{\rm np}$

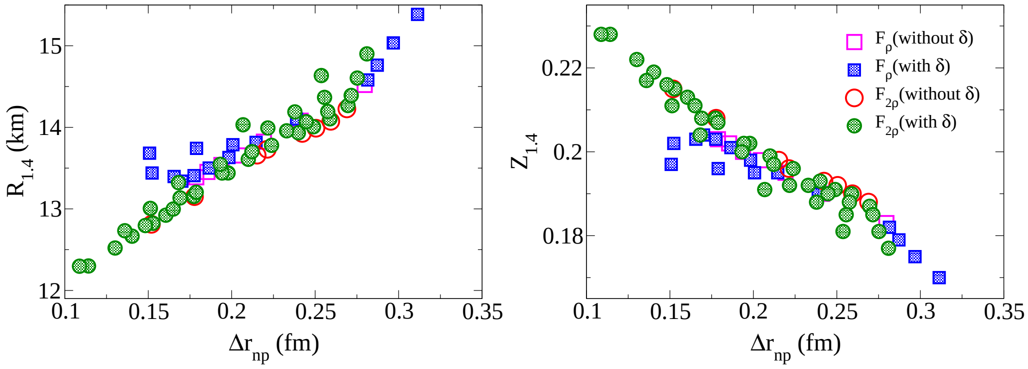

Figure 4.7: Plots for the radius $R_{1.4}$ for the neutron stars with the canonical mass $1.4M_\odot$ (left panel) and the corresponding red shift (right panel) as a function of $\Delta r_{\rm np}$ in the ^{208}Pb nucleus obtained for the F_ρ and $F_{2\rho}$ families of models.

obtained for the F_ρ and $F_{2\rho}$ families. Before embarking on our discussion, it may be reminded that the dependence of the various neutron star properties on the neutron-skin thickness are merely due to the fact that different models differ only in the density dependence of the symmetry energy. The EoS for the symmetric nuclear matter is taken to be the same for all the models, since, our goal is to study the diversities in the properties of the neutron stars arising purely due to the differences in the density dependence of the symmetry energy within the extended RMF model. In Fig. 4.7 the radii and red shifts for the neutron stars with mass $1.4M_\odot$ are plotted against the $\Delta r_{\rm np}$. The spread in $R_{1.4}$ and $Z_{1.4}$ for several cases corresponding to the similar $\Delta r_{\rm np}$ within the same family is smaller. The values of $R_{1.4}$ and $Z_{1.4}$ obtained for two different families differ noticeably at the smaller values of $\Delta r_{\rm np}$. For $\Delta r_{\rm np} = 0.15$ fm the maximum differences in the values of $R_{1.4}$ and $Z_{1.4}$ obtained for the two families are ~ 1.0 km and 0.02, respectively. In Fig. 4.8 We display our results for threshold mass the M_{DU} required for the enhanced cooling of neutron stars by means of neutrino emission from the nucleons in the direct Urca process [130]. The values of M_{DU} are quite sensitive to the neutron-skin thickness. The value of M_{DU} for the $F_{2\rho}$ family can vary over the range of $0.8 - 1.9M_\odot$ with $\Delta r_{\rm np}$ decreasing from 0.3fm to 0.1fm. This variation is little smaller for the case of F_ρ family. The value of M_{DU} for both the families differ quite significantly at

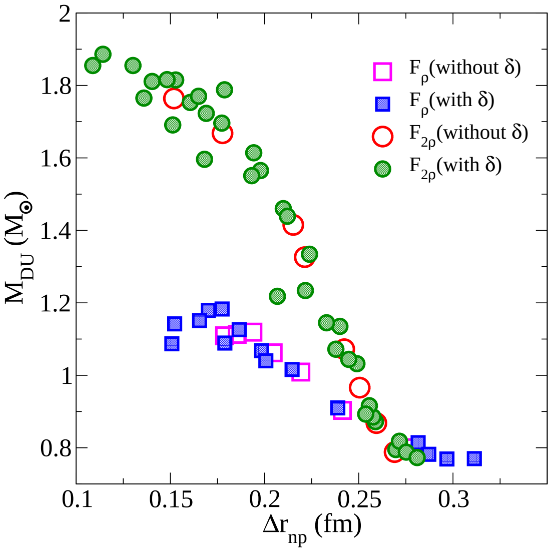

Figure 4.8: The dependence of the threshold neutron star mass M_{DU} on the neutron-skin thickness in ^{208}Pb nucleus. The neutron stars with mass equal to or larger than M_{DU} undergo enhanced cooling through direct Urca process for the cooling.

smaller Δr_{np}. At Δr_{np} =0.15 fm the difference between the values of M_{DU} for both the families is about $0.6M_\odot$ which is quite significant (40%).

Neutron stars are also considered one of the most important potential sources of gravitational wave, the ripples in the fabric of space-time [131–136]. They can emit gravitational waves in many different ways. Presence of mountains on rotating neutron stars, stellar oscillation modes and coalescence of neutron star binary systems are some of the possible reasons for gravitational wave radiation. Very recently, the gravitational wave from inward spiral and merger of a pair of neutron star (GW170817) has been detected for the first time in the ground-based LIGO-Virgo detectors [137]. Such gravitational wave carries the information of the neutron star equation of state through the tidally induced shift in the waveform phase that depends on the tidal polarizability (deformability) parameter λ. This parameter λ measures the quadrupole deformation of the star in response to the perturbing tidal field of the companion. Previously, the precise mass measurement of a massive neutron star was the only well-accepted astrophysical constraint on the neutron star

EoS. But now the detection of GW170817 offer another new window to deepen our understanding about the poorly known EoS of neutron star matter as it places a stringent limit on the tidal polarizability parameter λ which depends on the neutron star EoS through the radius of star R and the tidal Love number k_2 [138–141]. Therefore, the study of the link between various EoS components and the tidal polarizability parameter of a neutron star will indeed provide new insights into the EoS of dense nuclear matter.

We now consider our results for the tidal polarizability parameter λ defined as [138–141],

$$Q_{ij} = -\lambda \mathcal{E}_{ij}, \tag{4.1}$$

where, Q_{ij} is the induced quadrupole moment of a star in binary due to the static external tidal field of the companion star $\mathcal{E}_{ij}$. The parameter λ can be expressed in terms of the dimensionless quadrupolar tidal Love number k_2 as,

$$\lambda = \frac{2}{3G} k_2 R^5, \tag{4.2}$$

where, R is the radius of a isolated neutron star, i.e., long before merger. The value of k_2 depends on the stellar structure. The tidal Love number k_2 can be calculated using the following expression,

$$\begin{aligned} k_2 = {} & \frac{8C^5}{5} (1-2C)^2 \left[2 + 2C\left(y_R - 1\right) - y_R\right] \times \\ & \Big\{ 2C\left(6 - 3y_R + 3C(5y_R - 8)\right) + 4C^3 \left[13 - 11y_R + C(3y_R - 2) + 2C^2(1 + y_R)\right] \\ & \quad + 3(1-2C)^2 \left[2 - y_R + 2C(y_R - 1)\right] \log\left(1 - 2C\right) \Big\}^{-1}, \end{aligned} \tag{4.3}$$

where, C ($\equiv M/R$) is the compactness parameter of the star, and y_R ($\equiv y(R)$) can be obtained by solving the following differential equation,

$$r\frac{dy(r)}{dr} + y(r)^2 + y(r)F(r) + r^2Q(r) = 0 \ , \tag{4.4}$$

with

$$F(r) = \frac{r - 4\pi r^3\left(\epsilon(r) - p(r)\right)}{r - 2M(r)} \ , \tag{4.5}$$

$$\begin{aligned} Q(r) &= \frac{4\pi r\left(5\epsilon(r) + 9p(r) + \frac{\epsilon(r)+p(r)}{\partial p(r)/\partial\epsilon(r)} - \frac{6}{4\pi r^2}\right)}{r - 2M(r)} \\ &- 4\left[\frac{M(r) + 4\pi r^3 p(r)}{r^2\left(1 - 2M(r)/r\right)}\right]^2 \ . \end{aligned} \tag{4.6}$$

For a given EoS, Eq. (4.4) can be integrated together with the TOV equations with the boundary conditions $y(0) = 2$, $p(0) = P_c$ and $M(0) = 0$.

The values of λ for the neutron stars with masses $\sim 1M_\odot$ are sensitive to the behaviour of the symmetry energy at supra-nuclear densities [23]. In Fig. 4.9, we plot the values of λ as a function of neutron star mass obtained for different parameterizations for the F_ρ and $F_{2\rho}$ families. The value of $\Delta r_{\rm np}$ is equal to 0.15 fm for all of these cases. The differences in the tidal polarizability at low mass neutron star for the two different families is very small. But the difference increases as the mass increases due to different high density behaviour of the symmetry energy for different families of models. The values of λ for the neutron star with canonical mass vary over a wide range of 2.7×10^{36} to 4.3×10^{36} $\mathrm{cm^2gs^2}$. The value of λ at $1.4M_\odot$ obtained for the F_ρ family is about 1.5 times larger than that for the $F_{2\rho}$ family. The inclusion of δ mesons slightly lowers the value of tidal polarizability of neutron star with mass $1.4M_\odot$. On passing, it can be mentioned that the detection of gravitational wave signal coming from neutron star neutron star merger will certainly help in probing the uncertainties in the behaviour of symmetry energy.

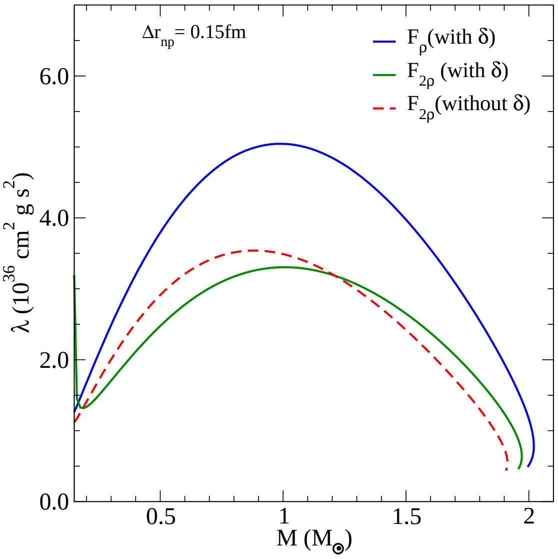

Figure 4.9: Variations in the tidal polarizability parameter λ with the neutron star mass for the different parameterizations of F_ρ and $F_{2\rho}$ families corresponding to neutron-skin thickness $\Delta r_{\rm np} = 0.15$ fm in the ^{208}Pb nucleus.

Table 4.3: Properties of neutron stars and the neutron-skin thickness in the ^{208}Pb nucleus obtained for SET1 -SET4 parameters. The values of tidal polarizability parameter $\lambda_{1.4}$, listed in the last row, correspond to the neutron star with mass $1.4M_\odot$.

	F_ρ		$F_{2\rho}$	
Properties	SET1	SET2	SET3	SET4
$\Delta r_{\rm np}$ (fm)	0.22	0.15	0.22	0.15
ρ_{DU} (fm)$^{-3}$	0.297	0.282	0.401	0.505
ρ_t(fm)$^{-3}$	0.058	0.069	0.073	0.107
P_t (MeV fm^{-3})	0.222	0.107	0.474	0.509
$R_{1.4}$(km)	13.08	12.96	13.00	12.37
$R_{\rm max}$(km)	11.40	11.68	11.29	11.28
$M_{DU}(M_\odot)$	1.01	1.09	1.33	1.69
$\lambda_{1.4}$ (10^{36} cm^{2}g s^2)	3.41	4.33	2.87	2.88

Finally, we have collected in Table 4.3 the results for the various properties of the neutron stars obtained for a few representative cases corresponding to the F_ρ and $F_{2\rho}$ families. The values of neutron-skin thickness for the ^{208}Pb nucleus are also listed. The comparison of the results obtained for the SET1 with those for SET3 or SET2 with SET4 readily gives a crude estimate about the variation in the properties of the neutron stars across the different families of models at a fixed neutron-skin thickness. Similarly, the idea about the effects of δ mesons within the same family can be obtained by comparing the results for SET1 with SET2 or SET3 with SET4. It may be easily verified from Table 4.3 and Figs. 4.7 - 4.9 that the values of core-crust transition density $\rho_t, R_{1.4}$, M_{DU} and the tidal polarizability parameter λ for both the families of the models can differ significantly at a fixed value of $\Delta r_{\rm np}$. Thus, instead of the $\sigma - \rho$ and $\omega - \rho$ cross-couplings as included separately in the different families of the models, a linear combinations of these cross-couplings in a single model would allow one to adjust the properties of the neutron stars over a wide range at a fixed value of the neutron skin thickness in a heavy nucleus, like, ^{208}Pb. Furthermore, the presence of δ mesons enable ones to obtain the models with smaller value of neutron-skin thickness as can be seen from the right panel of Fig. 4.2.

4.4 Conclusions

We have studied the differences in the various properties of the neutron stars arising mainly due to the uncertainties in the density content of the nuclear symmetry energy in the extended RMF model. With this aim, two different families of the extended RMF model, namely, F_ρ and $F_{2\rho}$ are obtained. The F_ρ family includes $\sigma - \rho$ cross-coupling, while, the $F_{2\rho}$ family includes $\omega - \rho$ cross-coupling. Both the families of models include the contributions from the δ meson in addition to several linear and non-linear interaction terms already present in the commonly used RMF models. Both the families have several parameterizations which give large variations in neutron skin thickness of ^{208}Pb without significantly affecting the other bulk properties of the nuclei.

We compare the various properties of neutron stars obtained for two different families of RMF models, F_ρ and $F_{2\rho}$. Most of these properties of the neutron stars at a fixed $\Delta r_{\rm np}$ are noticeably different for two different families of the models. These differences are pronounced at smaller values of $\Delta r_{\rm np}$ which can be attributed to the differences in the density dependence of the symmetry energy resulting due to different cross-coupling terms. For $\Delta r_{\rm np} = 0.15$fm in the ^{208}Pb nucleus, consistent with the current experimental data on dipole polarizability , the red-shift and the radius of neutron stars with mass $1.4M_\odot$ differs by about 10% for the two families of models. Such differences are quite significant ($\sim 40\%$) for the tidal polarizability parameter for the neutron stars with mass $1.4M_\odot$ and the threshold mass required for the direct Urca process to occur in the neutron stars. The values of the core-crust transition density also differs reasonably across the different families of the models. We may thus say that the simultaneous inclusion of the $\sigma - \rho$ and $\omega - \rho$ cross-couplings in the extended RMF model would enhance its flexibility to accommodate the variations in the properties of the neutron stars at a given neutron-skin thickness.

CHAPTER 5

Correlations of EoS parameters with neutron star radii

5.1 Introduction

The equation of state of highly asymmetric dense nuclear matter plays a key role in determining the global properties of neutron star. The behavior of the EoS for asymmetric nuclear matter is mainly governed by the nuclear matter incompressibility, symmetry energy and their slopes around the saturation density. In this chapter, the correlations of the neutron star radii with the key parameters governing the EoS of asymmetric nuclear matter are examined. It was previously found that the core-crust transition pressure is well correlated with the linear combination of the slope and the curvature of the symmetry energy [70]. In view of this, we can expect that the neutron star radii may also be strongly correlated with the linear combination of these EoS parameters, rather than each parameter individually, since, all of these nuclear parameters together determine the EoS of asymmetric nuclear matter. Therefore, we also investigate elaborately the correlations of neutron star radii with some selected linear combinations of these EoS parameters.

These EoS parameters are evaluated at the nuclear saturation density, using a representative set of RMF models, a set of Skyrme-type models, and one microscopic calculation using Brueckner-Hartree-Fock (BHF) with the Argonne V_{18} force, and a three body force of Urbana type [142], and a variational approach, in particular the Akmal-Pandharipande-Ravenhall (APR) EoS [143]. All models describe 2 $M_{\odot}$ stars. We demonstrate that the neutron star radii over a wide range of masses (0.6-1.8$M_{\odot}$) are strongly correlated with the linear combination of the slopes of nuclear matter incompressibility and symmetry energy coefficients.

5.2 Nuclear models

We use a representative set of RMF models, a set of Skyrme-type models, and two microscopic calculations for our correlation study. The RMF models can be classified broadly into two categories: (1) models with nonlinear self and/or mixed interaction terms and constant coupling strengths and (2) models with only linear interaction terms but density-dependent coupling strengths. The type I models used in the present calculations are BSR2, BSR3, BSR6 [101, 102], FSU2 [144], GM1 [3], NL3 [79], NL3$\sigma\rho$4, NL3$\sigma\rho$6 [145], NL3$\omega\rho$02 [71], NL3$\omega\rho$03 [89], TM1 [108], and TM1-2 [146]. The type II models are DD2 [147], DDHδ [148], DDHδMod [70], DDME1 [149], DDME2 [150], and TW [109]. The Skyrme models we use in this work are SKa, SKb [151], SkI2, SkI3, SkI4, SkI5 [152], SkI6 [153], Sly2, Sly9 [154], Sly230a [155], Sly4 [85], SkMP [156], SKOp [157], KDE0V1 [158], SK255, SK272 [159], Rs [160], BSk20, BSk21 [161], BSk22, BSk23, BSk24, BSk25, and BSk26 [162]. The microscopic calculations include the BHF EoS from [142, 163], and the APR EoS is taken from [70, 86, 143]. The values of the EoS parameters at saturation density show a wide variation across the models. The symmetric nuclear matter properties for these models are presented in Table 5.1. We shall mainly focus on the correlations between the neutron star radii and the various key parameters of

Table 5.1: EOS parameters calculated at saturation density for our representative sets of RMF, Skyrme, and microscopic calculations. The EOS parameters are the saturation density ρ_0 (in fm^{-3}), the binding energy per nucleon e_0, the nuclear matter incompressibility coefficient K_0, its skewness Q_0, the slope M_0, the symmetry energy coefficient J_0, its slope L_0, and the curvature parameter $K_{\rm sym,0}$ (all in MeV).

Model	ρ_0 (fm $^{-3}$)	e_0 (MeV)	K_0 (MeV)	Q_0 (MeV)	M_0 (MeV)	J_0 (MeV)	L_0 (MeV)	$K_{sym,0}$ (MeV)
BSR2	0.149	-16.03	240.0	-52.1	2829	31.4	62.2	-3.4
BSR3	0.150	-16.09	230.6	-119.4	2648	32.6	70.5	-7.8
BSR6	0.149	-16.13	235.9	-11.4	2820	35.4	85.6	-47.8
FSU2	0.150	-16.28	237.8	-156.1	2698	37.6	112.7	25.4
GM1	0.153	-16.30	300.1	-215.1	3387	32.5	93.9	18.0
NL3	0.148	-16.25	271.6	205.5	3464	37.4	118.5	100.9
NL3$\sigma\rho$4	0.148	-16.25	271.6	205.5	3464	33.0	68.3	-26.8
NL3$\sigma\rho$6	0.148	-16.25	271.6	205.5	3464	31.5	55.4	25.0
NL3$\omega\rho$02	0.148	-16.25	271.6	205.5	3464	33.1	68.2	-53.1
NL3$\omega\rho$03	0.148	-16.25	271.6	205.5	3464	31.7	55.3	-7.5
TM1	0.145	-16.26	281.2	-286.3	3088	36.9	110.8	33.6
TM1-2	0.145	-16.26	281.2	-199.3	3175	36.9	111.4	41.9
DD2	0.149	-16.02	242.2	167.4	3076	31.7	55.0	-93.4
DDHδ	0.153	-16.25	240.2	-539.8	2343	25.6	48.6	80.7
DDHδMod	0.153	-16.25	240.2	-539.8	2343	31.9	57.5	80.3
DDME1	0.152	-16.23	243.9	316.2	3249	33.1	55.4	-101.3
DDME2	0.152	-16.14	251.3	479.0	3493	32.3	51.3	-87.5
TW	0.153	-16.25	240.2	-539.8	2343	32.8	55.3	-124.8
SKa	0.155	-15.99	263.2	-300.3	2858	32.91	74.62	-78.46
SKb	0.155	-16.00	263.0	-300.3	2856	23.88	47.6	-78.5
SkI2	0.1575	-15.77	241.0	-340.0	2552	33.4	104.3	70.7
SkI3	0.1577	-15.98	258.2	-303.7	2795	34.83	100.5	73.0
SkI4	0.160	-15.95	247.95	-329.0	2646	29.50	60.39	-40.56
SkI5	0.156	-15.85	255.8	-302.1	2768	36.64	129.3	159.5
SkI6	0.159	-15.89	248.17	-327.8	2650	29.90	59.24	-46.77
Sly2	0.161	-15.99	229.92	-370.3	2389	32.00	47.46	-115.13
Sly230a	0.160	-15.99	229.90	-364.2	2394	31.99	44.30	-98.3
Sly4	0.159	-15.97	230.0	-362.9	2397	32.04	46.00	-119.8
Sly9	0.151	-15.80	229.84	-355.6	2402	31.98	54.86	-81.42
SkMP	0.157	-15.56	230.87	-342.7	2428	29.89	70.31	-49.82
SKOp	0.160	-15.75	222.36	-390.8	2277	31.95	68.94	-78.82
KDE0V1	0.165	-16.23	227.54	-384.9	2346	34.58	54.69	-127.12
SK255	0.157	-16.33	254.96	-350.2	2709	37.4	95.0	-58.3
SK272	0.155	-16.28	271.55	-305.2	2953	37.4	91.7	-67.8
Rs	0.158	-15.53	236.7	-348.3	2492	30.58	85.7	-9.1
BSk20	0.160	-16.08	241.4	-282.1	2615	30.0	37.4	-136.5
BSk21	0.158	-16.05	245.8	-274.1	2676	30.0	46.6	-37.2
BSk22	0.1578	-16.09	245.9	-275.4	2675	32.0	68.5	13.0
BSk23	0.1578	-16.07	245.7	-274.9	2674	31.0	57.8	-11.3
BSk24	0.1578	-16.05	245.5	-274.4	2672	30.0	46.4	-37.6
BSk25	0.1587	-16.03	236.0	-316.3	2516	29.0	36.9	-28.5
BSk26	0.1589	-16.06	240.8	-282.8	2607	30.0	37.5	-135.6
APR	0.161	-15.86	225.7	-362.6	2346	32.8	59.6	-123.3
BHF	0.160	-16.00	214.0	-881.0	1687	31.9	53.0	-98.1

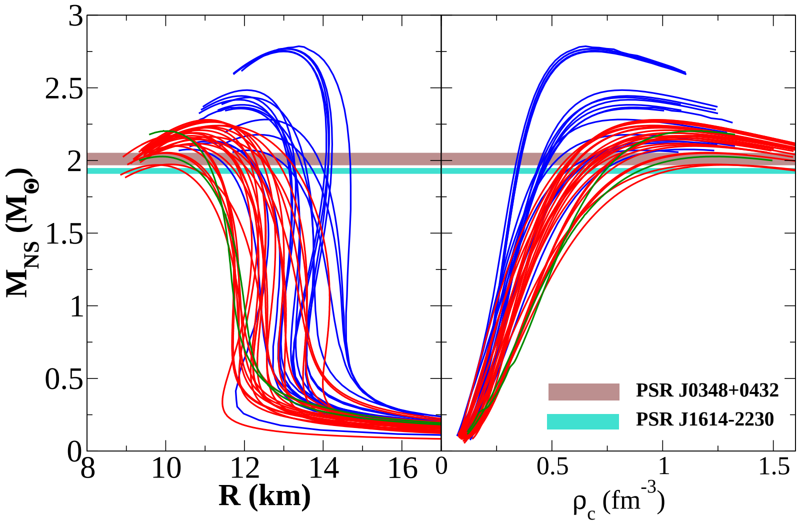

Figure 5.1: Neutron star mass in $M_\odot$ as a function of the radius in km (left) and central density in fm^{-3} (right) for a representative set of RMF (blue) and Skyrme (red) models, and microscopic (green) calculations.

the EoSs: K_0, Q_0, M_0, J_0, L_0, $K_{sym,0}$, and $K_{\tau,0}$, which are evaluated at saturation density.

5.3 Neutron star EoSs and Mass-radius results

It was shown in Ref. [33] that non-unified EoSs may introduce a large uncertainty on the determination of low-mass star radii, i.e. $M_{\rm NS} \lesssim 1.4M_\odot$, mainly if the behaviours of the symmetry energy slope for the EoSs of the inner crust and core are very different. For the RMF models, the EoSs for β-equilibrated matter are built according to the following procedure. The EoS for the outer crust region is taken from the work of Baym-Pethick-Sutherland [72]. For the inner crust region, we use the EoS including the pasta phases, if they exist, obtained within a Thomas Fermi calculation [164] up to the crust-core transition density, ρ_t. At the crust-core transition, the inner crust EoS is matched to the corresponding homogeneous EoS. The fraction of the particles at a given density is determined imposing β-equilibrium and charge neutrality. The model used for the outer crust is not the same as the one

Table 5.2: Maximum masses, $M_{\mathrm{NS}}^{\mathrm{max}}$, and radii, R_x, of neutron stars, for the RMF, Skyrme, and microscopic calculations used in this study. R_x denotes neutron star radii (in km) for a mass x (in $M_\odot$).

Model	$M_{\mathrm{NS}}^{\mathrm{max}}$ ($M_\odot$)	$R_{0.6}$ (km)	$R_{0.8}$ (km)	$R_{1.0}$ (km)	$R_{1.2}$ (km)	$R_{1.4}$ (km)	$R_{1.6}$ (km)	$R_{1.8}$ (km)
BSR2	2.38	13.20	13.19	13.26	13.33	13.38	13.39	13.36
BSR3	2.36	13.34	13.30	13.34	13.39	13.41	13.41	13.34
BSR6	2.43	14.07	13.86	13.80	13.77	13.76	13.73	13.66
FSU2	2.07	14.56	14.36	14.23	14.11	13.97	13.78	13.48
GM1	2.36	13.56	13.62	13.70	13.74	13.76	13.72	13.62
NL3	2.79	14.66	14.58	14.59	14.62	14.66	14.69	14.70
NL3$\sigma\rho$4	2.77	13.22	13.31	13.48	13.65	13.82	13.96	14.07
NL3$\sigma\rho$6	2.77	13.59	13.60	13.70	13.84	13.97	14.08	14.17
NL3$\omega\rho$02	2.75	13.58	13.56	13.66	13.78	13.91	14.01	14.09
NL3$\omega\rho$03	2.75	13.24	13.29	13.44	13.61	13.77	13.90	14.00
TM1	2.18	14.64	14.52	14.47	14.41	14.32	14.18	13.97
TM1-2	2.28	14.66	14.54	14.51	14.47	14.41	14.31	14.16
DD2	2.42	12.91	12.91	12.99	13.08	13.15	13.19	13.18
DDH$_\delta$	2.13	11.94	12.18	12.39	12.52	12.60	12.60	12.47
DDH$_\delta$Mod	2.12	12.73	12.77	12.83	12.89	12.89	12.81	12.62
DDME1	2.44	12.97	12.94	13.00	13.09	13.16	13.21	13.21
DDME2	2.48	12.86	12.88	12.99	13.10	13.21	13.28	13.30
TW	2.08	12.64	12.49	12.42	12.37	12.29	12.15	11.91
SKa	2.21	13.13	13.04	13.01	12.97	12.89	12.76	12.55
SKb	2.19	11.67	11.88	12.05	12.15	12.19	12.15	12.02
SkI2	2.16	13.50	13.56	13.58	13.55	13.46	13.28	12.98
SkI3	2.24	13.56	13.57	13.59	13.59	13.53	13.41	13.19
SkI4	2.17	12.16	12.24	12.31	12.36	12.35	12.28	12.11
SkI5	2.24	14.03	14.12	14.16	14.15	14.05	13.88	13.60
SkI6	2.19	12.33	12.37	12.44	12.48	12.47	12.40	12.24
Sly2	2.05	12.07	11.96	11.91	11.86	11.77	11.61	11.33
Sly230a	2.10	11.92	11.86	11.86	11.86	11.81	11.71	11.50
Sly4	2.05	11.97	11.86	11.82	11.77	11.69	11.53	11.25
Sly9	2.16	12.66	12.56	12.54	12.51	12.45	12.33	12.12
SkMP	2.11	12.57	12.58	12.58	12.56	12.48	12.32	12.05
SKOp	1.97	12.66	12.51	12.41	12.28	12.11	11.84	11.39
KDE0V1	1.97	12.26	12.03	11.90	11.77	11.61	11.36	10.95
SK255	2.14	13.80	13.57	13.42	13.29	13.12	12.90	12.58
SK272	2.23	13.85	13.63	13.51	13.41	13.29	13.13	12.88
Rs	2.12	13.02	13.05	13.05	13.01	12.91	12.73	12.42
BSk20	2.17	11.71	11.69	11.71	11.73	11.71	11.64	11.48
BSk21	2.28	12.22	12.28	12.39	12.47	12.53	12.53	12.46
BSk22	2.26	12.87	12.89	12.95	12.99	13.00	12.95	12.82
BSk23	2.27	12.57	12.61	12.69	12.76	12.79	12.76	12.66
BSk24	2.28	12.23	12.29	12.40	12.48	12.53	12.54	12.47
BSk25	2.22	11.88	11.99	12.13	12.25	12.33	12.36	12.30
BSk26	2.17	11.74	11.71	11.74	11.76	11.74	11.67	11.51
APR	2.20	12.17	11.88	11.75	11.67	11.60	11.49	11.33
BHF	2.03	12.29	12.11	12.00	11.90	11.76	11.55	11.20

used for the inner crust and the core regions. However, the use of different EoSs for the outer crust has been shown to barely affect the radius of a star for masses above $1M_{\odot}$ [33]. For the Skyrme models, the same functional is used for the crust and the core. In the crust, a compressible liquid-drop model (CLDM) and a variational approach, detailed in [33, 165], are employed to describe the nuclei. Finally, for the BHF and APR EoSs, the outer and inner crusts are described by the EoSs [166] and [74], respectively.

The mass M_{NS} and radius R of static neutron stars are obtained by solving the Tolman-Oppenheimer-Volkoff equations [129], using all of these 44 EoSs. The mass-radius relations are plotted in Fig. 5.1 (left panel), where the horizontal strips indicate the masses of the two heaviest neutron stars observed so far: PSR J0348+0432 [19] and PSR J1614-2230 [18, 167]. For the BSk models, the $M-R$ relations obtained with EoSs based on a simplified CLDM used in this work are close to the ones calculated with a full microscopic model in [49, 168], see in discussion in [33]. To facilitate our discussion, we also display the mass as a function of central density in the right panel of the same figure. The EoSs give rise to different neutron star properties. The spread in the maximum mass is $\sim 0.8M_{\odot}$, and the spread in the radius of neutron star with canonical mass ($1.4M_{\odot}$) is $\sim$ 3.1 km. In Table 5.2, we provide the maximum masses together with the radii for different neutron star masses, calculated for all the models used in this study.

The values of the EoS parameters and neutron star radii, obtained for these models, will be used to study the correlations between these observables, where the correlation between two observables are quantified by Pearson's correlation coefficient [169].

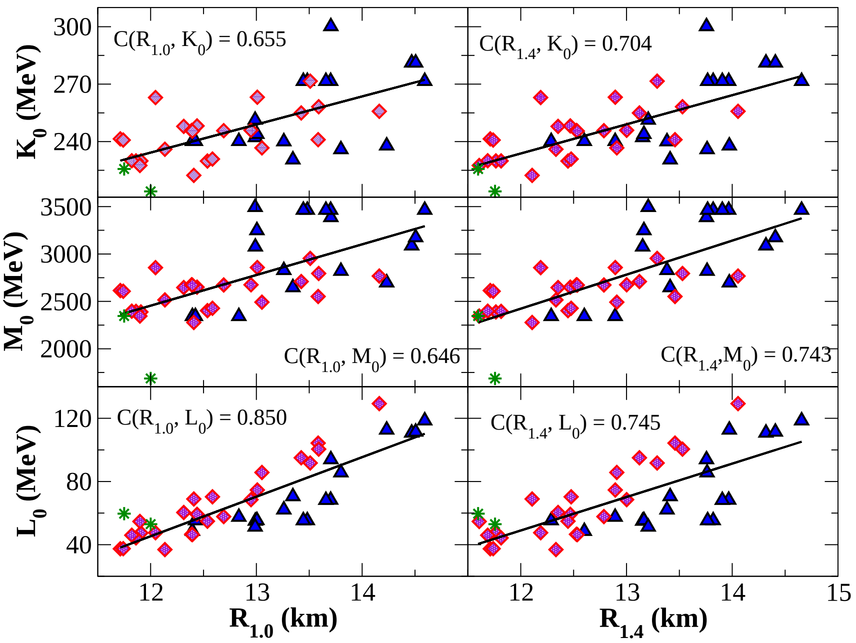

Figure 5.2: Radii $R_{1.0}$ (left) and $R_{1.4}$ (right) of a 1.0 and $1.4M_\odot$ neutron star versus the EoS parameters K_0, M_0 and L_0, obtained using our sets of RMF (blue triangles) and Skyrme (red diamonds) models, together with the BHF and the APR (green stars) calculations.

5.4 Correlation results and Discussion

In Fig. 5.2, we plot the radii of $1.0M_\odot$ and $1.4M_\odot$ stars, $R_{1.0}$ and $R_{1.4}$, versus some of these EoS parameters for our representative sets of RMF (blue triangles) and Skyrme (red diamonds) models, together with the BHF and the APR (green stars) calculations. The solid lines in the figures are obtained by linear regression and the correlation coefficients are indicated for each case considered. The correlations between the neutron star radius and the isoscalar parameters K_0 and M_0 increase with the increase of the neutron star mass, however, they are not significantly strong to make a meaningful prediction. The $R_{1.4}$-L_0 correlation is weaker than the $R_{1.0}$-L_0 correlation, which is opposite to the trend observed for the cases of K_0 and M_0. In Table 5.3, we list all the correlation coefficients between the EoS parameters K_0, M_0, Q_0, J_0, L_0, $K_{sym,0}$ and $K_{\tau,0}$, and the radii of neutron stars with different masses.

Table 5.3: Correlation coefficients between the neutron star radii and the different EoS parameters obtained for a representative set of RMF, Skyrme and microscopic calculations. The EoS parameters are the nuclear matter incompressibility coefficient K_0, its skewness Q_0, and slope M_0, the symmetry energy coefficient J_0, its slope L_0, and curvature $K_{\mathrm{sym},0}$, and the parameter $K_{\tau,0}$, calculated at the saturation density. R_x denotes the neutron star radius for a given mass x in units of $M_\odot$.

	K_0	Q_0	M_0	J_0	L_0	$K_{sym,0}$	$K_{\tau,0}$
$R_{0.6}$	0.565	0.383	0.548	0.815	0.887	0.581	-0.809
$R_{0.8}$	0.617	0.416	0.597	0.743	0.881	0.658	-0.775
$R_{1.0}$	0.655	0.461	0.646	0.680	0.850	0.698	-0.743
$R_{1.2}$	0.684	0.514	0.695	0.621	0.803	0.714	-0.716
$R_{1.4}$	0.704	0.571	0.743	0.562	0.745	0.711	-0.689
$R_{1.6}$	0.718	0.628	0.787	0.502	0.674	0.691	-0.661
$R_{1.8}$	0.725	0.686	0.828	0.438	0.590	0.653	-0.630

The study of the correlations clearly indicates that the radius of low-mass neutron stars is more sensitive to the isovector EoS parameters (J_0 and L_0), but, as the mass of the neutron star increases, the sensitivity to the isoscalar parameters (K_0 and M_0) tend to dominate. A similar conclusion was drawn in Ref. [33], where the behaviour of the radius of stars with mass $M_{\mathrm{NS}} = 1.0,\ 1.4,\ 1.8 M_\odot$ for 33 models, including 9 RMF models and 24 Skyrme forces, were plotted as a function of K_0 and L_0. The correlation coefficient $C(R_{1.0}, L_0)$ was 0.87, while $C(R_{1.8}, L_0)$ was 0.64. The value of $C(R_{1.0}, K_0)$ was 0.63, whereas the values of $C(R_{1.4}, K_0)$ and $C(R_{1.8}, K_0)$ were found to be ~ 0.66. These values are quite in agreement with the values we are finding in this work, especially for the correlation coefficients of the low-mass neutron star radii.

Next we look into the correlations of neutron star radii with selected combinations of isoscalar and isovector EoS parameters. In Fig. 5.3, we plot the neutron star radii for $M_{\mathrm{NS}} = 1.0\ M_\odot$ (left) and $1.4\ M_\odot$ (right) as a function of the linear combinations, $K_0 + \alpha L_0$ (top), and $M_0 + \beta L_0$ (bottom). We can see that the neutron star radii are better correlated with these combinations, than with the each of the parameter separately, as seen in Fig. 5.2. Further, the strongest correlations occur between the

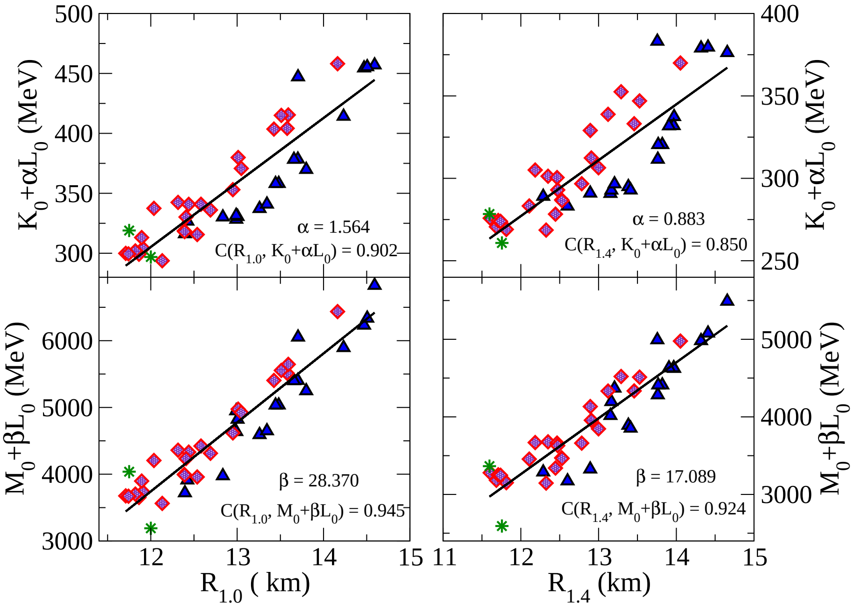

Figure 5.3: Neutron star radii $R_{1.0}$ (left) and $R_{1.4}$ (right) versus the linear correlations $K_0 + \alpha L_0$ (top) and $M_0 + \beta L_0$ (bottom), using a set of RMF (blue triangles), Skyrme (red diamonds), and BHF+APR (green stars) calculations.

neutron star radii and the linear combination $M_0 + \beta L_0$. In Table 5.4, we list again all the correlation coefficients of neutron star radii with $K_0 + \alpha L_0$ and $M_0 + \beta L_0$, for different neutron star masses. The values of α and β, also listed, are obtained in such a way that the correlations of these quantities with the neutron star radii are maximum.

Table 5.4: The correlation coefficients of neutron star radii with $K_0 + \alpha L_0$ and $M_0 + \beta L_0$, along with the values of α and β.

	$K_0 + \alpha L_0$		$M_0 + \beta L_0$	
	α	Corr. Coeff.	β	Corr. Coeff.
$R_{0.6}$	2.970	0.905	43.115	0.936
$R_{0.8}$	2.111	0.914	35.575	0.949
$R_{1.0}$	1.564	0.902	28.370	0.945
$R_{1.2}$	1.177	0.879	22.189	0.935
$R_{1.4}$	0.883	0.850	17.089	0.924
$R_{1.6}$	0.643	0.817	12.781	0.913
$R_{1.8}$	0.432	0.782	8.970	0.903

In the top panel of Fig. 5.4, we show the variation of the correlation coefficients of

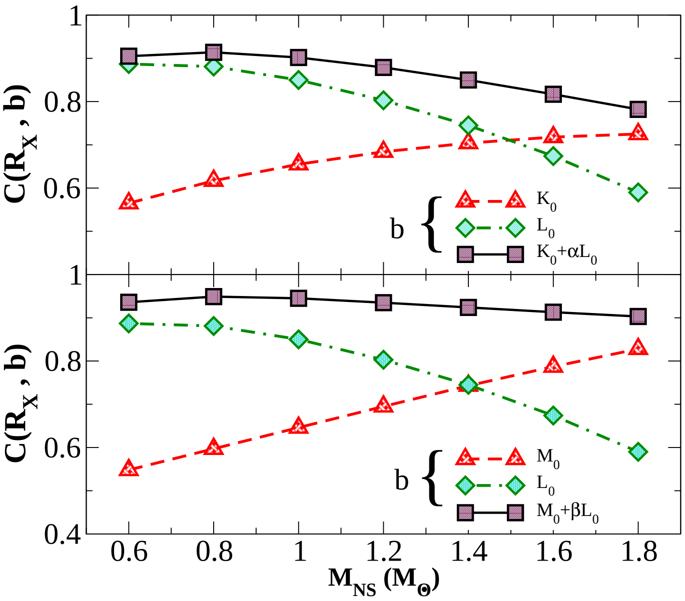

Figure 5.4: Correlation coefficients between the neutron star radii and several EoS parameters as a function of the neutron star mass. The EoS parameters 'b' denote K_0, L_0, and the linear combination $K_0 + \alpha L_0$ in the top panel, and M_0, L_0, and $M_0 + \beta L_0$ in the bottom panel.

neutron star radii with K_0, L_0, and $K_0 + \alpha L_0$, as a function of the mass of the star. The correlation of neutron star radii with $K_0 + \alpha L_0$ is better than those with K_0 and L_0 individually. However, for $M_{\rm NS} \gtrsim 1.0 M_\odot$, the correlations of neutron star radii decrease gradually with the increase of the neutron star mass, even considering $K_0 + \alpha L_0$. In the bottom panel of Fig. 5.4, we repeat the same exercise for M_0, L_0, and $M_0 + \beta L_0$. Again, contrary to the individual parameters M_0 and L_0, the neutron star radii are strongly correlated with $M_0 + \beta L_0$ over a wide range of neutron star masses (0.6 - $1.8 M_\odot$).

In order to interpret the correlations obtained, we consider the dependence of the pressure on the isoscalar coefficients, K_0, M_0, Q_0, and on the slope of the symmetry energy, L_0. Taking the expansions given in (1.3) and (1.6), the pressure is given by

$$P = \frac{\rho_0 x^2}{3} \left[\frac{K_0}{3}(x-1) + \frac{Q_0}{18}(x-1)^2 + L_0 \delta^2 \right] , \tag{5.1}$$

with $x = \rho/\rho_0$, or expressing Q_0 in terms of M_0 and K_0, by

$$P = \frac{\rho_0 x^2}{3}\left[K_0(x-1)\left(1-\frac{2x}{3}\right)+\frac{M_0}{18}(x-1)^2+L_0\delta^2\right]. \tag{5.2}$$

These two equations and the empirical relation $R \propto P^{1/4}$, identified in Ref. [7, 20], where R is the star radius and P the pressure, calculated for some fiducial density, $\sim 1-2\rho_0$, allow an interpretation of the above correlations of R with $K_0+\alpha L_0$ and $M_0+\beta L_0$.

In the following, we present some arguments that explain the correlations: a) if $\rho = \rho_0$, only the L_0 term survives and this may explain why the radius of low-mass neutron stars is well correlated with L_0; b) from eq. (5.2), it is seen that, for $\rho = 1.5\rho_0$, the pressure depends only on M_0 and L_0. This behavior explains that the correlation of M_0 with the star radius shown in Fig. 5.2 is better for $R_{1.4}$ than for $R_{1.0}$, and also that the correlation of R with $M_0+\beta L_0$ is so strong; c) the contribution of the K_0 term in (5.1) is more important than the Q_0 term for $x-1<1$, which explains the correlation of R with $K_0+\alpha L_0$; d) d) the asymmetry parameter δ monotonically decreases from its maximum value ~ 0.95, obtained at densities of the order of $\rho_0/2$ to $0.65<\delta<0.85$ at $2\rho_0$. If the term in K_0 is neglected in eq. (5.2), the pressure satisfies $P \propto M_0+\frac{18\delta^2}{(x-1)^2}L_0 = M_0+\beta' L_0$. Taking for β' the upper and lower value of β in Table 5.4, we get, respectively, $x = 1.45$ and $x = 1.99$, above and just below the value $x = 1.5$, when the relation is exact. Therefore, it seems the relation is being applied within the valid range of density. On the other hand, from eq. (5.1) and neglecting the term in Q_0, the relation $P \propto K_0+\frac{3\delta^2}{(x-1)}L_0 = K_0+\alpha' L_0$, is obtained. We now take for α' the upper and lower values of α from Table 5.4, and we get, respectively, $x = 1.49$ and $x = 4.40$. The last value is already out of the validity of the approximation, and even for $x = 2$, this approximation is not very good. This might be the plausible reason that only the low-mass neutron star radii are strongly correlated with $K_0+\alpha L_0$.

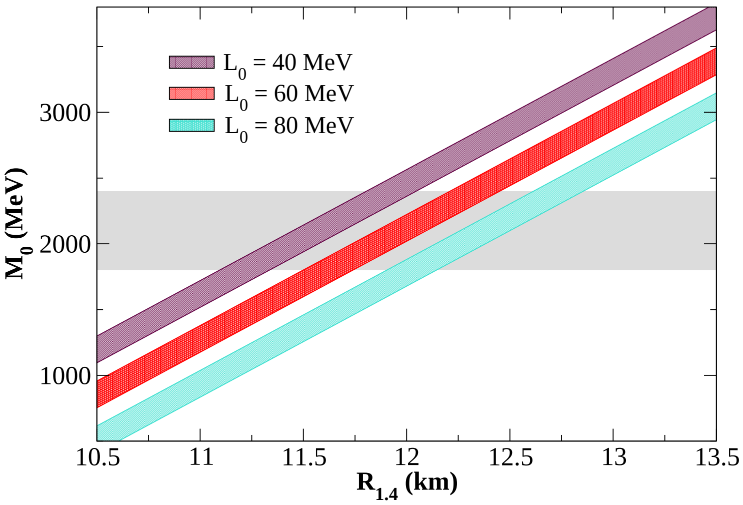

Figure 5.5: M_0 as a function of $R_{1.4}$ for $L_0 = 40$, 60 and 80 MeV, as obtained from the multiple linear regression. The gray shaded region indicates the constraint on M_0 derived in Ref. [170].

The knowledge of the slopes of nuclear matter incompressibility and symmetry energy at saturation density can constrain the neutron star radii as these radii are strongly correlated with $M_0 + \beta L_0$. An overall variation in L_0 = 20-80 MeV is obtained from the analysis of the giant dipole resonance of ^{208}Pb [171, 172], the giant quadrupole resonance in ^{208}Pb [100], the pygmy dipole resonance in ^{68}Ni and ^{132}Sn [173], and nuclear ground state properties, using the standard Skyrme Hartree-Fock approach [174]. A fit of the EoS for asymmetric nuclear matter, or pure neutron matter [65, 85], or the binding energies of large number of deformed nuclei [175, 176] within different mean field models, constrains the value of L_0 in the range of $40-70$ MeV. The combined results of nuclear structure and heavy ion collisions lead to the central value of $L_0 = 70$ MeV [116]. We adopt L_0 = 40-80 MeV, which has a good overlap with these investigations. The value of M_0 = 1800-2400 MeV [170] at the saturation density seems to be consistent with its value at $\rho = 0.1$ fm^{-3}, deduced from the energies of the isoscalar giant monopole resonance in the ^{132}Sn and ^{208}Pb nuclei [30, 31]. In Fig. 5.5, we plot the incompressibility slope parameter M_0 as a function of $R_{1.4}$, for different values of the symmetry energy slope $L_0 = 40$, 60 and 80 MeV. The gray shaded region corresponds to the constraint on M_0 as obtained in Ref. [170]. These values of M_0 and L_0 suggest that $R_{1.4}$ should be in the range of 11.09-12.86 km, which is consistent with the results of the Ref. [177]. Let us remark that if we had only taken the RMF models, the above correlations would have been slightly stronger, as expected, because all models in the study would have had a similar underlying framework, and larger radii would have been obtained for a 1.4 $M_\odot$ star, namely $R_{1.4}$ would have come out in the range of 11.82-13.25 km. Indeed Fig. 5.1 shows that, on average, RMF models lead to larger radii than the other types of calculations.

5.5 Conclusions

In conclusion, we have studied the possible existing correlations between neutron star radii at different masses and the nuclear coefficients of the nuclear matter EoSs, calculated at the saturation density. The neutron star radii are obtained using unified EoSs, fully for the Skyrme models, and partially for inner-crust-core EoSs for the RMF models, except for the two microscopic EoSs. All EoSs are consistent with the existence of $2M_\odot$ neutron stars. The radii of the low-mass neutron stars are better correlated with the symmetry energy coefficient J_0 and its slope L_0. As the neutron star mass increases, the correlations of the radii with the nuclear matter incompressibility K_0 and its slope M_0 grow stronger. Our investigation reveals that the neutron star radii are better correlated with the linear combinations $K_0 + \alpha L_0$ and $M_0 + \beta L_0$ than with the individual EoS parameters. In particular, noticeable improvement is seen in the correlations of the radii with these linear combinations, for $1.4M_\odot$ neutron stars. The correlations of the radii with $M_0 + \beta L_0$ are stronger, and almost independent of the neutron star mass, in the range 0.6-1.8$M_\odot$. A plausible interpretation for the existence of such correlations is traced back to the correlations between the pressure and similar linear combinations of the EoS parameters in the relevant density range. The values of M_0 and L_0, as currently deduced from finite nuclei data, constrain $R_{1.4}$ in the range 11.09-12.86 km.

CHAPTER 6

Warm asymmetric dilute matter and critical parameters

6.1 Introduction

Core-collapse supernovae (CCSN) [178–181] are one of the most energetic events in the Universe. Matter can reach temperatures up to $\sim$ 20 MeV and the density at bounce of the collapsing core goes up to 1.5 - 2.0 times the nuclear saturation density. During the collapse, matter does not have enough time to reach β-equilibrium conditions [182], because the event timescale is believed to be of the order of seconds, and usually a fixed proton fraction of $y_p \sim 0.3$ [181] is considered for the calculation of the EoS. For a recent review on the relevant thermodynamics and composition for the equation of state for CCSN, compact stars and compact stars mergers, one can refer to [183] and references therein. At densities below nuclear saturation, light [147, 184–188] and heavy clusters [164, 189–194] can form, and they can modify the neutrino transport, which will affect the cooling of the proto-neutron star [195, 196], as neutrinos play a considerable role in the development of the shock wave during the collapse [197, 198]. The determination of the region of densities, proton fractions and temperatures where these instabilities exist is, therefore, very important for core-collapse simulations.

Critical properties of hot asymmetric and symmetric nuclear matter may be studied with heavy ion collisions, in particular, with nuclear reactions that involve the formation of compound nuclei or multifragmentation. These data will be important to constrain the CCSN EoS. As shown in Ref. [199], the expected range of densities and temperatures for CCSN matter just before bounce lie in the typical (ρ,T) space, $\rho \sim 0.05\rho_0 - 0.4\rho_0$ and $T \sim 3 - 8$ MeV, for nuclear multifragmentation reactions.

In Refs. [200], the authors used several methods to determine the core-crust transition, including a Thomas Fermi calculation of the inner crust and the thermodynamical and dynamical spinodals, and they showed that for finite temperature and fixed proton fractions (CCSN conditions), the thermodynamical method gave quite similar results to more demanding calculations, like the Thomas-Fermi calculation. In Ref. [201], the authors also used this method together with other two to calculate the core-crust transition and pressure at zero temperature, and using two of the families that are also going to be used in this work. They observed that this calculation gives a good estimation of the transition, like the authors of Ref. [70] also found.

In this work, the critical parameters for hot asymmetric nuclear matter for six different families of RMF models are studied using the thermodynamical method. These six families of models have been built from three different appropriately calibrated base models. An extra term that couples the ρ-meson either to the σ or ω-meson is added to each of the base models to yield wide variations in the symmetry energy slope L_0. The effect of L_0 on the critical temperature, density and proton fraction is then explored. We also compare our findings with experimental results from references [202–208] for the critical temperature, and the theoretical study of Ref. [209].

6.2 Results

In this section, we first briefly describe the different families of the RMF models used for the current study. Next, we present our results for the spinodal instabilities and critical points in hot asymmetric matter at different temperatures. The effect of the symmetry energy slope parameter, L_0, on this quantities will be addressed as well.

6.2.1 Models

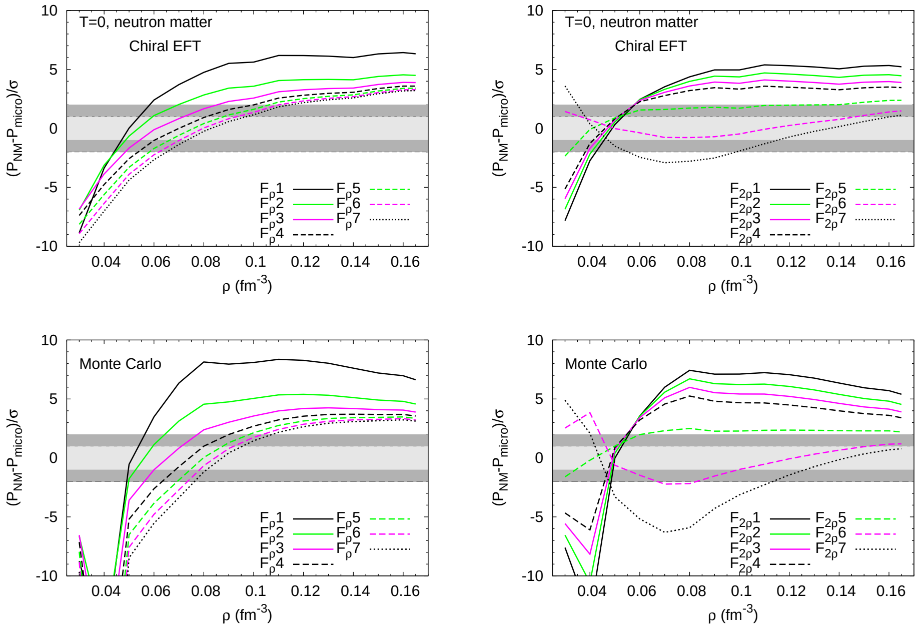

Figure 6.1: Difference between the neutron matter pressure for the F_ρ (left panels) and $F_{2\rho}$ (right panels) families and the average pressure obtained from a chiral EFT [210] (top) and Monte Carlo [211] (bottom) calculations, in units of the pressure uncertainty at each density, $\sigma = \Delta P$. The gray bands represent the calculation uncertainty (light) and twice this uncertainty (dark).

In this work, we are going to consider six different families of RMF models, namely, NL3$\omega\rho$ [89], TM1$\omega\rho$ [145], $F_{2\rho}$ [38, 101], NL3$\sigma\rho$ [145], TM1$\sigma\rho$ [145], and F_ρ [38]. The NL3$\omega\rho$ and NL3$\sigma\rho$ (TM1$\omega\rho$ and TM1$\sigma\rho$) families are obtained from the base model NL3 [79] (TM1 [108, 212]). The F_ρ and $F_{2\rho}$ families are obtained from the base model BKA22 [101]. The families NL3$\omega\rho$, TM1$\omega\rho$ and F$_{2\rho}$ include a quartic order cross-coupling $\omega^2\rho^2$ term ($\eta_{2\rho} \neq 0$), whereas the NL3$\sigma\rho$ and TM1$\sigma\rho$ families have a quartic order cross coupling $\sigma^2\rho^2$ term ($\eta_{1\rho} \neq 0$). On the other hand, a cubic order cross-coupling $\sigma\rho^2$ term ($\eta_\rho \neq 0$) is included in the F$_\rho$ family. The strengths of the cross-couplings ($\eta_{2\rho}, \eta_{1\rho}$, and η_ρ), and that of the coupling of the ρ-mesons to the nucleons (g_ρ), are appropriately adjusted to vary the slope of symmetry energy over a wide range without compromising the properties of the finite nuclei significantly. The cross-couplings $\eta_{2\rho}$ or $\eta_{1\rho}$ or η_ρ is increased (decreased) and accordingly g_ρ is also increased (decreased) in such a way that either the binding energy of ^{208}Pb nucleus is close the the experimental value or the symmetry energy at density 0.1 fm^{-3} is exactly the same as that for the base model. Different combinations of the coupling strengths yield different behaviours for the density dependence of the symmetry energy. The variants of NL3 and TM1 models are obtained by varying $\eta_{2\rho}$ or $\eta_{1\rho}$ and adjusting g_ρ in such a way that the symmetry energy at $\rho = 0.1$ fm^{-3} is equal to the one obtained for the base models [71, 89]. The variants of BKA22 model (i.e. F$_{2\rho}$ and F$_\rho$ families) are obtained by varying $\eta_{2\rho}$ or η_ρ and adjusting g_ρ to reproduce the binding energy of the ^{208}Pb nucleus. All the families of models considered are consistent with the observational constraints imposed by the measured mass ($\sim 2M_\odot$) of the pulsars J1614-2230 [18,167] and J0348+0432 [19], see e.g. [25] and references there in. Besides these observational constrains, there are also experimental results and first-principle calculations that can allow to set limits on the stellar matter EoS. In Table 6.1, we present some bulk properties of ^{208}Pb nucleus as well as the neutron star maximum mass and corresponding radius obtained for the models with extreme values of L_0 from each families.

In addition to these six families of models, we also consider as reference two extra models with density dependent couplings: DD2 [147] and DDME2 [150]. In Ref. [33], it was shown that these two models satisfy a well accepted set of laboratorial, theoretical and observational constraints. We are, therefore, interested in comparing

Table 6.1: The values of the binding energy per particle (B/A), charge radii (r_c), neutron radii (r_n) and neutron skin thickness (Δr_{np}) for ^{208}Pb nucleus along with the maximum mass (M_{max}) of neutron star and corresponding radius (R_{max}) obtained for some selected models.

Model	B/A (MeV)	r_c (fm)	r_n (fm)	Δr_{np} (fm)	M_{max} ($\mathrm{M}_\odot$)	R_{max} (km)
$F_\rho 1$	-7.871	5.529	5.751	0.280	1.99	11.77
$F_\rho 7$	-7.871	5.559	5.680	0.179	1.97	11.33
$F_{2\rho} 1$	-7.871	5.529	5.740	0.269	1.95	11.61
$F_{2\rho} 7$	-7.870	5.555	5.649	0.152	1.93	11.06
NL3	-7.878	5.518	5.740	0.280	2.78	13.29
NL3$\sigma\rho$6	-7.913	5.535	5.662	0.185	2.77	13.14
NL3$\omega\rho$6	-7.921	5.530	5.667	0.195	2.76	12.99
TM1	-7.877	5.541	5.753	0.270	2.18	12.49
TM1$\sigma\rho$6	-7.923	5.558	5.686	0.186	2.15	12.02
TM1$\omega\rho$6	-7.791	5.552	5.689	0.195	2.13	11.97

the behaviour of these models at finite temperature with the behaviour of the six families of models we are going to analyse.

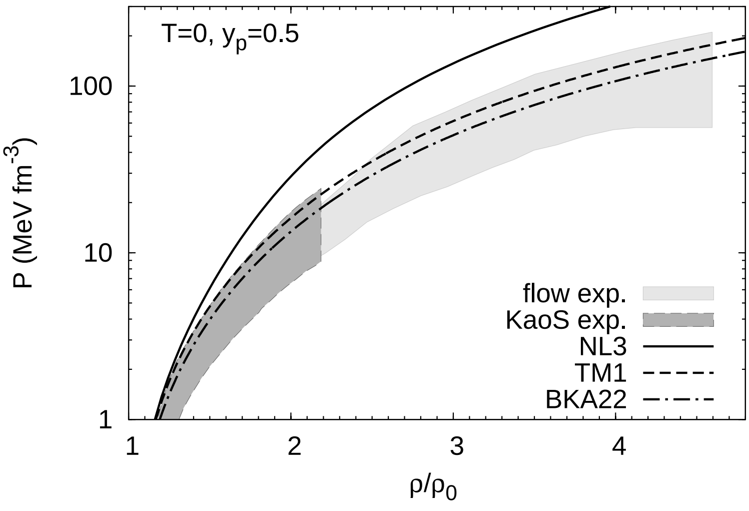

Figure 6.2: Symmetric matter pressure as a function of the density for the NL3 (solid), TM1 (dashed) , and BKA22 (dash-dotted) models. The colored bands are the experimental results obtained from collective flow data in heavy-ion collisions [47] (light gray) and from the KaoS experiment [48, 213] (dark gray).

In Fig. 6.1, we compare the neutron matter pressure of the F$_\rho$ and $F_{2\rho}$ families with microscopic calculations based on nuclear interactions derived from chiral effective field theory (EFT) [210], and quantum Monte Carlo techniques with realistic two-

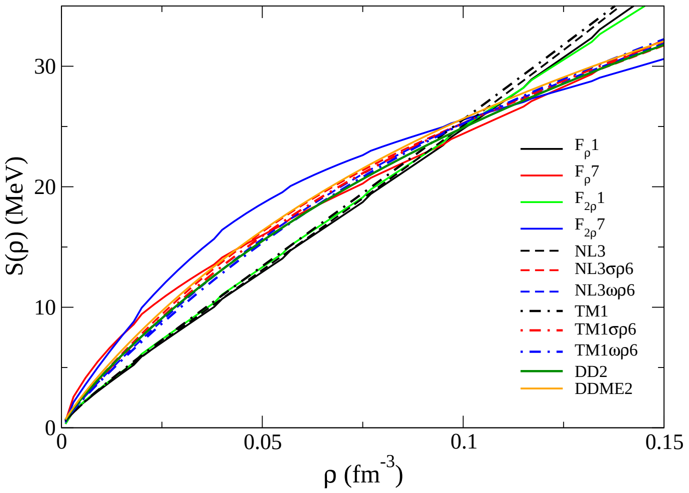

Figure 6.3: Symmetry energy as a function of baryon density for the F$_\rho$1, F$_\rho$7, F$_{2\rho}$1, F$_{2\rho}$7 (solid), NL3, NL3$\sigma\rho$6, NL3$\omega\rho$6 (dashed), and TM1, TM1$\sigma\rho$6, TM1$\omega\rho$6 (dash-dotted) models. The DD2 (green) and DDME2 (orange) models are also represented for comparison.

and three-nucleon interactions [211]. We show the difference from the neutron matter pressure of each model to the microscopic results, normalized to the pressure uncertainty of the microscopic calculations, $\sigma = \Delta P$, at each density. These uncertainties are represented by light gray bands, and they indicate that the points that lie inside those bands are within the data limits. Also shown are dark gray bands that denote twice the calculation uncertainties, 2σ. We observe that only F$_{2\rho}$5 and F$_{2\rho}$6 lie in the bands' limits. All the other models fail to satisfy these constrains. Similarly, for other families, it was shown in Ref. [145] that only 4 models, NL3$\omega\rho$6, NL3$\sigma\rho$6, TM1$\omega\rho$6, and TM1$\sigma\rho$6, passed these microscopic constrains.

In Fig. 6.2, we show the EoSs for symmetric nuclear matter for the three base models considered, together with the experimental results from collective flow data in heavy-ion collisions [47], and from the KaoS experiment [48, 213]. The models of the NL3 family do not satisfy these constraints but the EoSs for the other models lie within the experimental bounds. However, the modelling of flow in transport simulations is a complex process and, therefore, these constraints should be considered with care. Consequently, we will also include the models of the NL3 family in the present study.

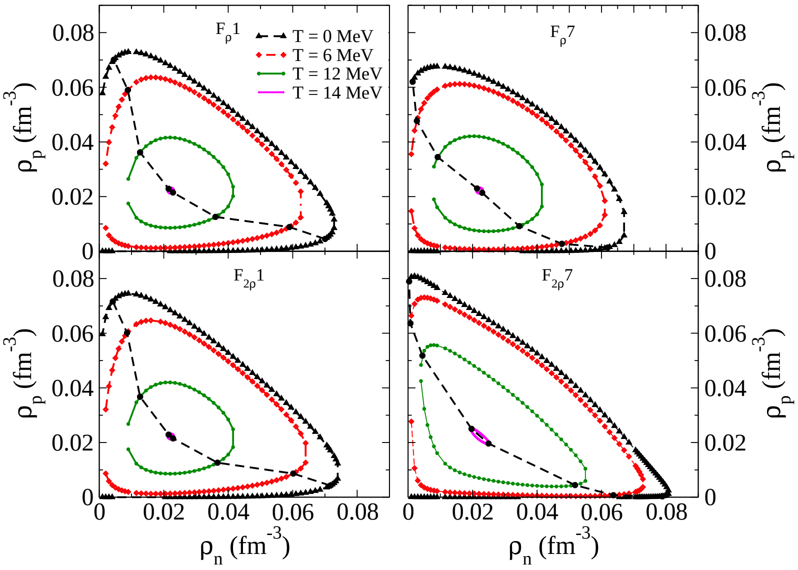

Figure 6.4: Spinodal sections on the (ρ_n, ρ_p) plane for $F_\rho 1$ (top left), $F_\rho 7$ (top right), $F_{2\rho}1$ (bottom left) and $F_{2\rho}7$ (bottom right) models at $T = 0, 6, 12$ and 14 MeV.

We will be discussing the effect of the density dependence of symmetry energy on the extension of the instability. To facilitate our discussions, we show in Fig. 6.3 the behaviour of symmetry energy at sub-saturation densities for the models with extreme values of the slope L_0. The models with the largest L_0 have all a very similar behavior, showing an almost linear increase of the symmetry energy with the density, typical of models that do not have non-linear terms involving the ρ-meson. With respect to the models with the smallest L_0, the NL3x6 and TM1x6 models have a similar behavior and $L_0 \sim 55$ MeV, showing a larger symmetry energy below $\rho = 0.1$ fm^{-3} than the models with large L_0. $F_{2\rho}7$ has a more extreme behavior due to its lower L_0, $L_0 = 45$ MeV. The symmetry energy curves for the models corresponding to extreme values of L_0 cross each other at $\rho \sim 0.1$ fm^{-3}, except for the F_ρ family. The $F_\rho 7$ crosses $F_\rho 1$ at a smaller density.

6.2.2 Spinodal sections and Critical points

The spinodal sections and critical points for the models discussed above are obtained by the thermodynamical method presented in section 2.3.3.

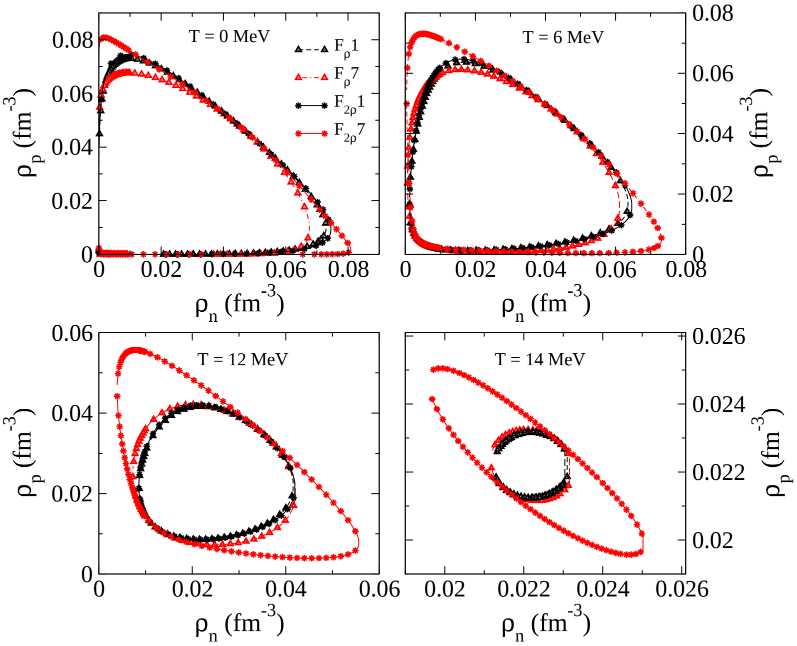

Figure 6.5: Spinodal sections on the (ρ_n, ρ_p) plane for $F_\rho 1$, $F_\rho 7$, $F_{2\rho}1$ and $F_{2\rho}7$ models at $T = 0$ (top left), 6 (top right), 12 (bottom left) and 14 (bottom right) MeV.

We will start with the analysis of the effects of temperature on the spinodal sections obtained for the models with extreme values of L_0, in particular the largest and the lowest of each family. In Figs. 6.4 and 6.5, we plot the spinodal sections of members 1 and 7 of the F_ρ and $F_{2\rho}$ families for $T = 0$, 6, 12 and 14 MeV, and, in Fig. 6.4, we also represent the line of critical points by a dashed line. At these points, which are common to both the binodal and the spinodal, the direction of the instability is parallel to the tangent at the spinodal, and the pressure is maximum. Some conclusions are in order: a) the behavior with temperature is similar to the one obtained in [93], the larger the temperature the smaller the spinodal section and matter is more symmetric inside the spinodal. Eventually, at the critical temperature, the section is reduced to a point and, for larger temperatures, homogeneous matter is always stable; b) the spinodal sections of models $F_\rho 1$ and $F_{2\rho}1$, left panels of Fig. 6.4, are very similar, as expected, because, these two models have very similar properties (see also Fig. 6.3): they are the models with the largest slope L_0 and the strength of the cross-couplings is very small; c) the same is not true for the members with the smallest values of L_0, $F_\rho 7$ and $F_{2\rho}7$. The spinodal of the $F_{2\rho}7$ model

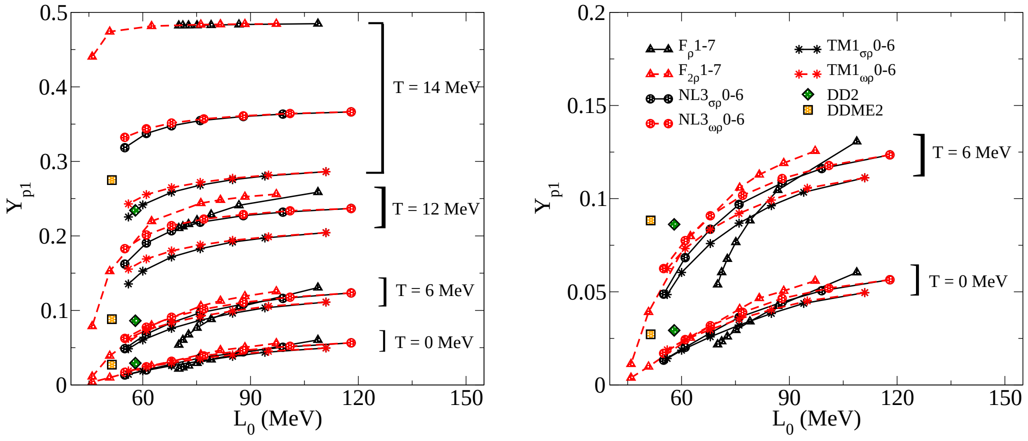

Figure 6.6: Critical proton fraction, Y_{pc}, as a function of L_0 for several temperatures, and for all the models considered in this study. The right panel shows the results for $T = 0$ and 6 MeV only.

Table 6.2: Critical temperatures, and their correspondent critical densities and pressures for all the models considered in this work. The proton fraction is 0.5.

Model	T_c (MeV)	ρ_c (fm^{-3})	P_c (MeVfm^{-3})
DD2	13.73	0.0452	0.1785
DD-ME2	13.12	0.0445	0.1556
$F_{x\rho}$	14.01	0.0444	0.1802
NL3	14.55	0.0463	0.1999
TM1	15.62	0.0486	0.2365

becomes larger, extending to larger asymmetries and densities. This same behavior was obtained with the NL3 and TM1 families, and has been discussed in [145, 214], but for dynamical spinodals. The F_ρ family shows a different behavior, and the spinodal of the model with the smallest L_0, $F_\rho 7$, is smaller than $F_\rho 1$. This may be attributed to the different behavior of the symmetry energy for this model, as can be seen from Fig. 6.3. In Fig. 6.5, where we compare the four models at different temperatures, it is clear that $F_{2\rho}7$ is the one for which the spinodal section extends to a larger range of densities and asymmetries. This behavior is expected since this is the model with the smallest L_0.

We now consider the variations of the critical density and proton fraction with the temperature and the symmetry energy slope parameter. Before embarking on this, we would like to discuss briefly the results for the critical temperature, the

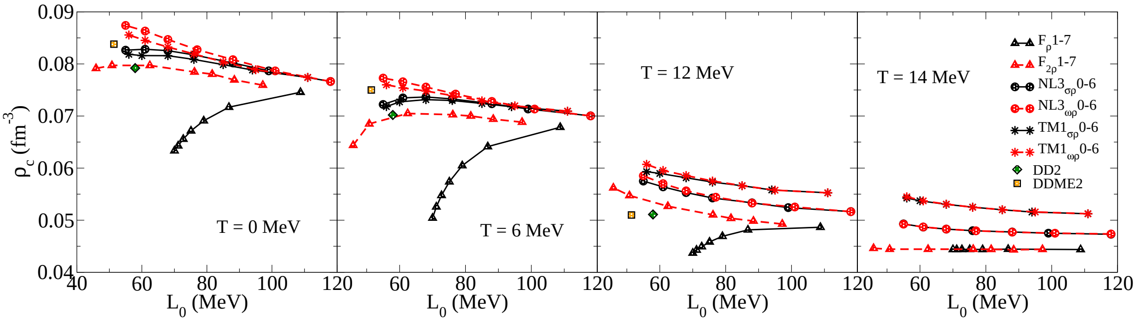

Figure 6.7: Critical density, ρ_c, as a function of L_0, for several temperatures, and for all the models considered in this study.

temperature at which the instability region melts.

The critical temperature is totally defined by the isoscalar properties of the model and, therefore, it is the same for models that only differ on the isovector properties: the critical temperatures for NL3$x\rho$,TM1$x\rho$ and $F_{x\rho}$ are the same as those for the corresponding base models NL3, TM1, BKA22, respectively. The values of the critical temperature, density and pressure for the base models, as well as for the DD2 and DDME2 models, are given in Table 6.2. For the BKA22 model, the critical temperature is very close to 14 MeV, while for the TM1 model, the critical temperature is above 15 MeV, and for NL3, T_c = 14.55 MeV. The TM1 and NL3 T_c values fall inside the interval of temperatures $14.2 \leq T_c \leq 16.1$ MeV, obtained in [209] from a set of RMF models with non-linear σ terms that have an effective mass at saturation that reproduces finite nuclei spin-orbit splittings, and an incompressibility in the range 250$\leq K_0 \leq$ 315 MeV, as proposed in [215], and the critical temperature for the BKA22 model lies very close to the bottom limit. While the incompressibilities for TM1 and NL3, 281 and 272 MeV, respectively, lie inside the range considered [209], for the BKA22 models, it is 220 MeV, and, therefore, it is outside that interval. However, the critical temperatures predicted by the models in the present study are far from the value $T_c = 17.9 \pm 0.4$ MeV obtained in [204] from the analysis of six different sets of experimental data from heavy-ion reactions. Let us stress that three of the models considered (DD2, DDME2 and NL3$\omega\rho$6) went through a set of laboratorial and theoretical constraints for neutron matter, besides predicting star masses above $2\,M_\odot$, as identified in [33], and they predict critical temperatures below 14.55 MeV, even below 14 MeV. Besides these three models, also models NL3$\sigma\rho$6, TM1$\omega\rho$6, TM1$\sigma\rho$6 , $F_{2\rho}$6 satisfy most of these constraints: TM1 models have an incompressibility outside the range considered in [33], but well inside the range proposed in [215], and $F_{2\rho}$6 predicts a maximum neutron star mass just below $2M_\odot$. In [204], the authors have performed a quite complete compilation of theoretical predictions for the critical temperature, and, in fact, the RMF models that predict a critical temperature close to $T_c = 17.9 \pm 0.4$ MeV do not satisfy most of the laboratorial constraints at saturation density or below. Thus, one conclusion that can be drawn is that the theoretical critical temperature predicted by the models fitted to the ground state properties of finite nuclei and nuclear matter, and satisfying the $2M_\odot$ constraint, does not agree with the experimentally extracted value of the critical temperature.

The critical points give us an indication of the phase space region where non-homogeneous matter is expected. The critical densities for neutron rich matter and respective proton fraction for $T = 0, 6, 12$ and 14 MeV are given in Table 6.3, and displayed as a function of L_0 in Figs. 6.6 and 6.7. The largest temperature considered, 14 MeV, is very close to the critical temperature of the F_ρ and $F_{2\rho}$ models. Above the critical temperature, the models do not present instabilities and the formation of clusters is not expected. We first discuss the critical proton fraction. This quantity tells us that matter at the critical density with smaller proton fractions is stable against clusterization at the temperature considered. In the left panel of Fig. 6.6, the critical proton fractions are given for all the temperatures considered. This allows us to see the dependence of the critical proton fraction on the temperature. The right panel of Fig. 6.6 shows the same but more extensively for $T = 0$ and 6 MeV. There is a clear dependence of the critical proton fraction on the slope L_0 (see right panel of Fig. 6.6 for more details). The critical proton fraction increases when

L_0 increases: this behavior is valid for all the temperatures considered. However, it should be pointed out that the smaller the L_0, the softer is the increase of the Y_{pc} with temperature, for temperatures well below the critical temperature, and this results in a much wider range of critical protons fractions at finite temperature than at $T = 0$. For instance, the critical proton fractions for the $F_{2\rho}7(F_\rho 1)$ associated with smaller (larger) values of L_0 are 0.0039 (0.0604), 0.0112 (0.1307), and 0.0788 (0.2587) at temperature T = 0, 6, and 12 MeV, respectively.

We also notice that the spread in the values of the critical proton fraction, at a given L_0, among the various models considered, increases with temperature. For a given L_0, the spread of values is not larger than ~ 0.01 at $T = 0$ MeV. At $T = 6$ (12) MeV the critical proton fractions spread over at least ~ 0.03 (~ 0.1), for a fixed L_0. The largest temperature considered is almost coincident with, or close to, the critical temperature of the models under study. It is striking that there can be a difference of ~ 0.25 between the proton fractions of these models. Taking as reference $L_0 \sim 56$ MeV, a value within the constraints imposed by experiments, Y_{pc} varies between 0.018 and 0.023 for $T = 0$ MeV, 0.048 and 0.065 for $T = 6$ MeV, 0.136 and 0.186 for $T = 12$ MeV, and between 0.225 and 0.478 for $T = 14$ MeV. These trends indicate that the models which are calibrated using bulk ground state properties of the finite nuclei do not constrain very well the values of the critical proton fractions at finite temperatures. In fact, it should be pointed out that the large spread on the critical proton fraction close to 14 MeV results from the fact that for some models, BKA22 (base model for F_ρ and $F_{2\rho}$ families), this temperature is very close to the critical temperature, while for the TM1 models, the critical temperature is above 15 MeV, and for NL3, $T_c = 14.55$ MeV. Temperatures of the order 5 - 12 MeV occur in core collapse supernova matter. We may, therefore, expect a different evolution of the supernova when different models are considered as the underlying model of the simulation. In the neutrino trapped phase, a typical proton fraction is 0.3, and we conclude from the left panel of Fig. 6.6 that while for NL3, F_ρ, and

Table 6.3: Critical densities, ρ_c, and proton fractions, Y_{pc}, for different temperatures, and for all the models considered. The slope parameter L_0 and temperature T are in MeV. The critical density ρ_c is in fm^{-3}.

		$T=0$		$T=6$		$T=12$		$T=14$	
Model	L_0	ρ_c	Y_{pc}	ρ_c	Y_{pc}	ρ_c	Y_{pc}	ρ_c	Y_{pc}
DD2	57.94	0.0792	0.0293	0.0702	0.0862	0.0511	0.2343	-	-
DD-ME2	51.4	0.0838	0.0272	0.0750	0.0883	0.0510	0.2749	-	-
$F_\rho 1$	108.77	0.0746	0.0604	0.0678	0.1307	0.0486	0.2587	0.0444	0.4848
$F_\rho 2$	86.77	0.0717	0.0424	0.0641	0.1046	0.0481	0.2410	0.0444	0.4836
$F_\rho 3$	79.02	0.0691	0.0341	0.0605	0.0883	0.0469	0.2287	0.0444	0.4829
$F_\rho 4$	75.10	0.0672	0.0294	0.0574	0.0766	0.0458	0.2210	0.0444	0.4825
$F_\rho 5$	72.74	0.0656	0.0260	0.0548	0.0676	0.0449	0.2159	0.0444	0.4824
$F_\rho 6$	71.16	0.0643	0.0234	0.0526	0.0605	0.0443	0.2127	0.0444	0.4823
$F_\rho 7$	70.02	0.0633	0.0217	0.0504	0.0539	0.0437	0.2105	0.0444	0.4823
$F_{2\rho} 1$	97.19	0.0759	0.0559	0.0688	0.1256	0.0493	0.2560	0.0444	0.4845
$F_{2\rho} 2$	88.44	0.0769	0.0505	0.0694	0.1191	0.0498	0.2525	0.0443	0.4842
$F_{2\rho} 3$	81.62	0.0780	0.0466	0.0700	0.1129	0.0504	0.2483	0.0444	0.4839
$F_{2\rho} 4$	76.17	0.0785	0.0408	0.0703	0.1059	0.0510	0.2440	0.0444	0.4835
$F_{2\rho} 5$	62.45	0.0797	0.0253	0.0705	0.0799	0.0527	0.2198	0.0444	0.4815
$F_{2\rho} 6$	50.80	0.0797	0.0098	0.0685	0.0391	0.0547	0.1527	0.0444	0.4741
$F_{2\rho} 7$	45.91	0.0791	0.0039	0.0644	0.0112	0.0562	0.0788	0.0446	0.4405
NL3	118.00	0.0766	0.0565	0.0700	0.1235	0.0517	0.2369	0.0473	0.3664
NL3$\sigma\rho$1	99.00	0.0787	0.0506	0.0713	0.1162	0.0524	0.2319	0.0475	0.3634
NL3$\sigma\rho$2	88.00	0.0802	0.0445	0.0724	0.1085	0.0533	0.2272	0.0477	0.3602
NL3$\sigma\rho$3	76.00	0.0817	0.0363	0.0733	0.0969	0.0543	0.2183	0.0480	0.3548
NL3$\sigma\rho$4	68.00	0.0825	0.0279	0.0737	0.0836	0.0553	0.2069	0.0483	0.3478
NL3$\sigma\rho$5	61.00	0.0828	0.0202	0.0735	0.0683	0.0564	0.1905	0.0487	0.3375
NL3$\sigma\rho$6	55.00	0.0826	0.0133	0.0722	0.0487	0.0575	0.1622	0.0493	0.3184
NL3$\omega\rho$1	101.00	0.0787	0.0519	0.0713	0.1178	0.0525	0.2337	0.0475	0.3642
NL3$\omega\rho$2	88.00	0.0808	0.0464	0.0728	0.1108	0.0533	0.2287	0.0477	0.3611
NL3$\omega\rho$3	77.00	0.0827	0.0390	0.0742	0.1017	0.0544	0.2226	0.0480	0.3570
NL3$\omega\rho$4	68.00	0.0847	0.0318	0.0756	0.0908	0.0556	0.2138	0.0483	0.3515
NL3$\omega\rho$5	61.00	0.0863	0.0244	0.0766	0.0775	0.0570	0.2013	0.0487	0.3437
NL3$\omega\rho$6	55.00	0.0874	0.0170	0.0773	0.0625	0.0585	0.1829	0.0492	0.3323
TM1	111.00	0.0774	0.0496	0.0709	0.1112	0.0553	0.2044	0.0512	0.2862
TM1$\sigma\rho$1	94.00	0.0788	0.0438	0.0718	0.1034	0.0558	0.1972	0.0516	0.2803
TM1$\sigma\rho$2	85.00	0.0799	0.0384	0.0724	0.0962	0.0566	0.1917	0.0520	0.2754
TM1$\sigma\rho$3	76.00	0.0809	0.0321	0.0730	0.0868	0.0573	0.1828	0.0525	0.2681
TM1$\sigma\rho$4	68.00	0.0815	0.0258	0.0732	0.0759	0.0581	0.1717	0.0530	0.2585
TM1$\sigma\rho$5	60.00	0.0818	0.0186	0.0727	0.0604	0.0590	0.1528	0.0537	0.2417
TM1$\sigma\rho$6	56.00	0.0817	0.0142	0.0718	0.0485	0.0593	0.1356	0.0543	0.2254
TM1$\omega\rho$1	95.00	0.0789	0.0451	0.0720	0.1056	0.0558	0.1988	0.0516	0.2817
TM1$\omega\rho$2	85.00	0.0804	0.0404	0.0729	0.0993	0.0566	0.1941	0.0520	0.2773
TM1$\omega\rho$3	76.00	0.0819	0.0354	0.0739	0.0921	0.0575	0.1878	0.0525	0.2718
TM1$\omega\rho$4	68.00	0.0832	0.0297	0.0748	0.0834	0.0586	0.1799	0.0531	0.2648
TM1$\omega\rho$5	61.00	0.0845	0.0243	0.0754	0.0732	0.0595	0.1691	0.0537	0.2554
TM1$\omega\rho$6	56.00	0.0856	0.0189	0.0760	0.0624	0.0607	0.1555	0.0545	0.2430

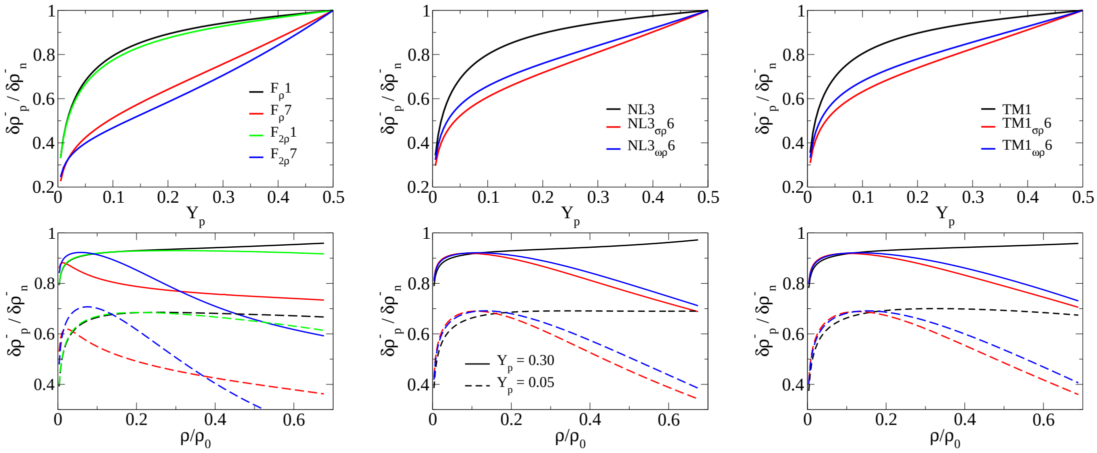

Figure 6.8: The fluctuations $\delta\rho_p^- / \delta\rho_n^-$ at $T = 0$ MeV as a function of the proton fraction Y_P (top panels) with $\rho = 0.06$ fm^{-3}, and as a function of ρ/ρ_0 (bottom panels), with $Y_p = 0.30$ (solid), and 0.05 (dashed). The calculations shown are for the models F_ρ and $F_{2\rho}$ (left), $NL3\omega\rho$ and $NL3\sigma\rho$ (middle) and $TM1\omega\rho$ and $TM1\sigma\rho$ (right panels).

$F_{2\rho}$, matter at $T = 14$ MeV is not clusterized, for TM1, nonhomogeneous matter still occurs under these conditions. As a reference we also include the critical proton fractions and the critical densities of the models DD2 and DDME2 in Figs. 6.6 and 6.7, since these models satisfy many well established properties. They both have a critical temperature below 14 MeV. At $T = 0$, they show a proton fraction above the predicted one by the model with a similar symmetry energy of the six families studied. This difference grows as the temperature increases, because these models have a lower critical temperature than all the others.

Let us now discuss how the critical density, ρ_c, changes with L_0 and T. In Fig. 6.7, the critical densities are plotted for the different models and temperatures considered. The model F_ρ stands out because it is the only one that presents a critical density that increases when L_0 increases, for all temperatures. The density dependence of the symmetry energy in this model is determined by the term $\sigma\rho^2$, while all the others have a term $\sigma^2\rho^2$ or $\omega^2\rho^2$. Models $F_{2\rho}$, NL3$\sigma\rho$ and TM1$\sigma\rho$ also show this trend for the lowest temperatures considered, 0 and 6 MeV, and $L_0 \lesssim 60$ MeV. In all other cases, ρ_c decreases when L_0 increases. The critical densities of models DD2

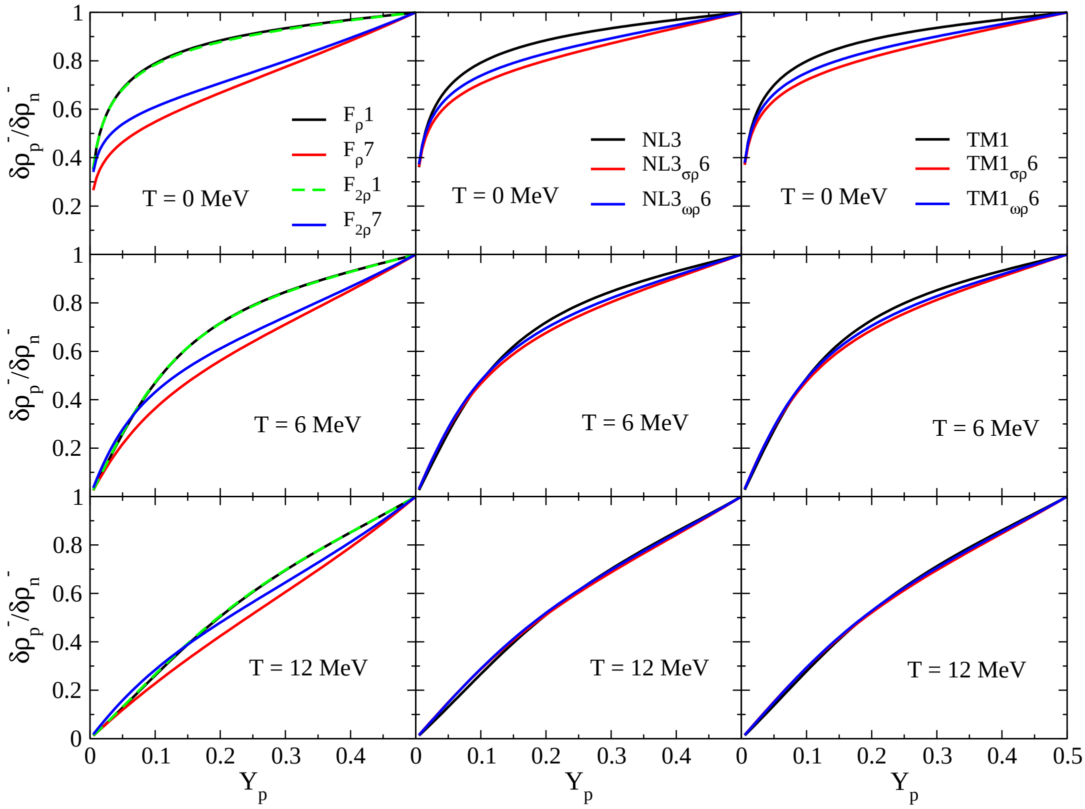

Figure 6.9: The fluctuations $\delta\rho_p^-/\delta\rho_n^-$ as a function of the proton fraction, Y_P, for a fixed baryon density of $\rho = 0.04$ fm^{-3} at $T = 0$ MeV (top), $T = 6$ MeV (middle), and $T = 12$ MeV (bottom panels), for the $\mathrm{F}_{x\rho}$ (left), NL3$x\rho$ (middle), and TM1$x\rho$ (right) families.

and DDME2 agree with the other models. Taking again $L_0 = 56$ MeV as reference, ρ_c decreases with T, from 0.080-0.087 fm^{-3} at $T = 0$, to 0.044-0.054 fm^{-3} at $T = 14$ MeV, while the spread of ρ_c increases slightly with temperature, from 0.006 fm^{-3} at $T = 0$ MeV to 0.01 fm^{-3} at $T = 14$ MeV. This quantity seems, therefore, to be more constrained than the critical proton fraction.

We address next the distillation effect [93, 216], that is, the different isospin content of each phase, with the gas being more neutron-rich and the liquid phase with a proton fraction close to symmetric matter. This is possible from the analysis of the instability direction given by $\delta\rho_p^-/\delta\rho_n^-$. This quantity, calculated at $T = 0$, has been plotted in Fig. 6.8 as a function of the proton fraction, Y_P, for $\rho = 0.06$ fm^{-3} in the top panels, and as a function of the density divided by the nuclear saturation density, ρ/ρ_0, in the bottom panels, and two different values of Y_p (0.30 and 0.05) for

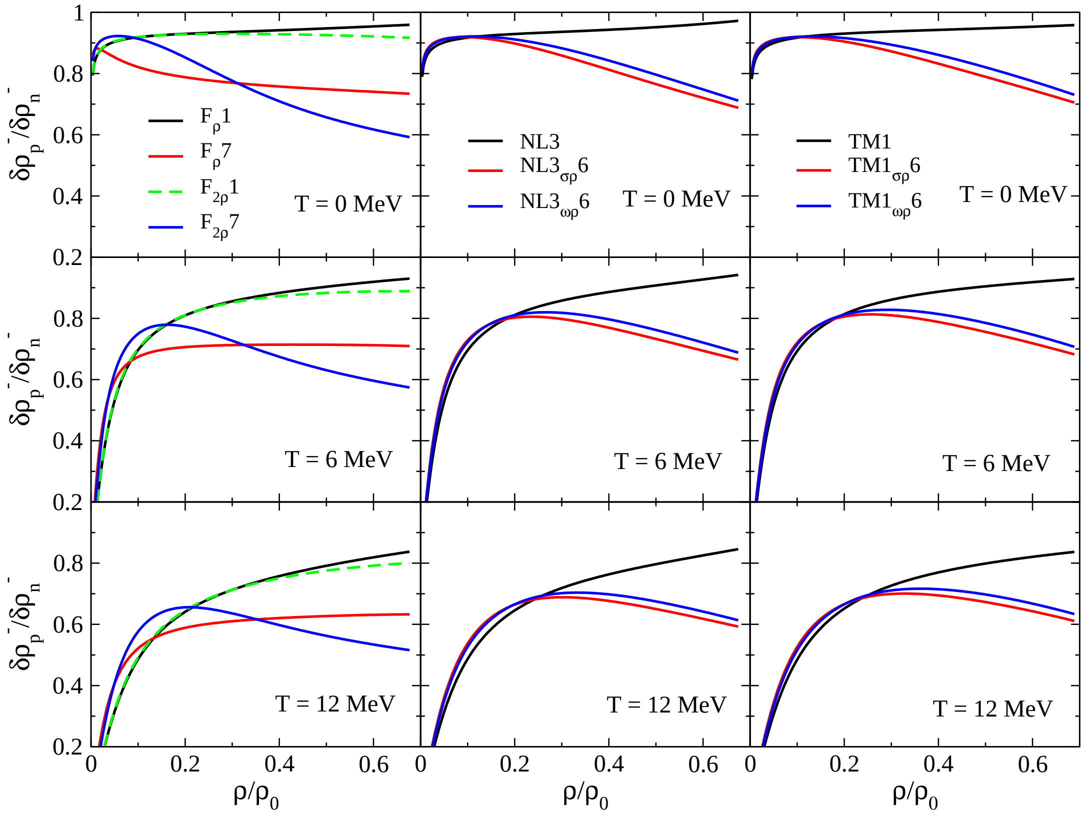

Figure 6.10: The fluctuations $\delta\rho_p^-/\delta\rho_n^-$ as a function of ρ/ρ_0, for a fixed proton fraction of $Y_p = 0.3$, at $T = 0$ MeV (top), $T = 6$ MeV (middle), and $T = 12$ MeV (bottom panels), for the $F_{x\rho}$ (left), NL3$x\rho$ (middle), and TM1$x\rho$ (right) families.

the models F_ρ and $F_{2\rho}$ (left), NL3$\omega\rho$ and NL3$\sigma\rho$ (middle) and TM1$\omega\rho$ and TM1$\sigma\rho$ (right panels). The two proton fractions considered are of the order of the proton fractions expected in cold catalyzed stellar matter. It is seen that the distillation effect is present in all models, the direction of instability favors a more isospin symmetric dense matter and a more asymmetric gas phase. However, there is a clear difference between models with a large L_0 and a small L_0: the distillation effect is much stronger for the first ones, and for a fixed proton fraction, the distillation effect increases with density, while for the second ones, after a maximum attained at ~ 0.02 fm^{-3}, the ratio $\delta\rho_p^-/\delta\rho_n^-$ decreases as the density increases. A similar behavior was obtained for density dependent models in [93]. While $F_{2\rho}7$ has a behavior very similar to NL3$x\rho$7 and TM1$x\rho$7 models, with $x = \sigma$ or ω, once more the $F_\rho 7$ shows a particular behavior, showing a smaller (larger) distillation effect for $\rho <$ (>)0.04

fm^{-3} than the other models with a similar L_0. Below saturation density, models with a smaller L_0 have larger symmetry energies that disfavor a strong distillation effect.

In Figs. 6.9 and 6.10, the quantities $\delta\rho_p^-/\delta\rho_n^-$ are plotted for different temperatures. We have considered the density 0.04 fm^{-3} in the set of plots of Fig. 6.9 because this is the density that corresponds to clusterized matter at all temperatures. It is evident that the dependence of the distillation effects on the symmetry energy slope parameter gets washed out with the temperature, and for $T = 6$ MeV, the differences are already small, although there are still noticeable differences for the $F_{x\rho}$ families.

In Fig. 6.10, the proton fraction has been fixed to a typical value that occurs in trapped neutrino matter, $y_p = 0.3$, and the dependence of $\delta\rho_p^-/\delta\rho_n^-$ on the density is shown for different temperatures. Models of the TM1 and NL3 families are different above densities $\rho \sim 0.03 - 0.04$ fm^{-3}, with the models with smaller slopes L_0 showing a decrease of the ratios, with a larger effect on the models with a $\sigma^2\rho^2$ non-linear term. Models of the $F_{x\rho}$ families show larger differences at all temperatures, with the small L_0 models having larger $\delta\rho_p^-/\delta\rho_n^-$ values below $\rho \sim 0.02$ fm^{-3}. The $F_\rho 7$ model differs again from all the other models with a similar L_0, showing a $\delta\rho_p^-/\delta\rho_n^-$ that increases monotonically with ρ at finite T.

6.3 Conclusions

In the present study, we have analysed the extension of the nonhomogeneous nuclear matter in the density, isospin and temperature directions, as predicted by six different families of the RMF models, together with two density-dependent models. The six families of models have been built from three different base models, whose parameters are fitted to the ground state properties of nuclei. An extra term that couples the ρ-meson either to the σ or ω-meson is appropriately added to each of the base models to yield the variation in the symmetry energy slope L_0 approximately between 50 and 100 MeV [38, 71, 89]. The thermodynamical spinodal sections are determined by the loci in phase space where the curvature matrix of the free energy is zero. These spinodal sections and lines of critical points are obtained for temperatures below the critical temperature above which there is a smooth transition from a gas to a liquid phase. The critical proton fractions and densities for a given temperature give us an indication whether clusterized matter could occur under some particular conditions. In particular, the clusterized matter is not expected at densities larger and proton fractions smaller than the corresponding critical values.

It is shown that for a given symmetry energy slope parameter L_0, the models that include a non-linear $\sigma - \rho$ cross-coupling predict smaller critical densities and proton fractions. The effect is specially strong for the F_ρ family, which includes a $\sigma\rho^2$ cross-coupling term. The critical density is more constrained. In fact, considering a slope $L_0 = 56$ MeV, the spread on the critical density increases from 0.006 fm^{-3} at $T = 0$ to $\sim$ 0.01 fm^{-3} at $T = 14$ MeV. The critical proton fraction at zero temperature increases when the slope L_0 increases, and for a given value L_0, it is almost independent of the model considered. This is not the case at finite temperature, where a spread on the proton fraction of 0.25 for $T = 14$ MeV is found, when all the different models are considered. This large spread on the critical proton fraction close to 14 MeV can be attributed to the different critical temperatures of the models under study. Since the models considered predict different critical temperatures associated with symmetric matter, the critical proton fractions at temperatures above 10 MeV may show a large spread.

We have also analysed the behavior of the distillation effect with temperature. In particular, previous results, concerning a smaller effect within models with a smaller slope L_0, were confirmed. Although the temperature washes out some of the differences between the models, mainly among the models of the same family, some differences remain, the stronger ones among models belonging to the $F_{x\rho}$ families.

It is observed that the F_ρ family, which includes a cubic cross-coupling term of the type $\sigma\rho^2$, behaves differently as compared to the other families of models in which quartic cross-coupling terms of the type $\sigma^2\rho^2$ or $\omega^2\rho^2$ are considered. Five of the six the families contain at least one model that satisfies the constrains coming from microscopic calculations for pure neutron matter at sub-saturation densities (see Fig. 6.1 and Ref. [145]), the F_ρ family being the only one that does not satisfy this constrain.

Seemingly, these results favour the inclusion of quartic order cross-coupling terms over the cubic order term, though a cubic term should also be included from "naturalness" arguments [37, 80, 217]. Therefore, a more careful calibration should be undertaken, which takes into account constrains from nuclear ground state properties, as well as constraints coming from microscopic calculations for neutron matter.

CHAPTER 7

Summary and Conclusions

In this thesis, we have studied the dependence of various crustal and bulk properties of neutron stars on different key parameters of nuclear matter EoS in detail. In chapter 1, we have given a general introduction to the neutron star and nuclear matter equation of state. Chapter 2 deals with the theoretical models for neutron stars and nuclear matter equation of state. We have presented the derivation of stellar structure equations and discussed how mass and radius of a neutron star can be obtained by solving these equations. Two widely used phenomenological nuclear models, relativistic mean field and Skyrme Hartree Fock, to describe neutron star matter EoS have been briefly reviewed. The methods used to calculate the core-crust transition densities and instabilities in the hot asymmetric nuclear matter have also been discussed.

We have examined the dependence of core-crust transition properties of the neutron star with symmetry energy parameters in chapter 3. In doing this, we have employed three different families of the systematically varied extended RMF model. These three different families of the extended RMF model correspond to different strength for the ω-meson self-coupling. Each of the families contains seven parameterizations of RMF model having wide variations in their symmetry energy behavior.

We have found a strong correlation between core-crust transition density ρ_t and the symmetry energy slope parameter L_0 at the saturation density, which is in agreement with that obtained in the earlier investigations. Moreover, a good correlation between the transition density ρ_t and the symmetry energy at the saturation density has also been observed, but, it seems to be model dependent. The link between the transition pressure P_t and L_0 is rather poor. The P_t does not show appreciable correlations with the symmetry energy elements J_0 and L_0 at the saturation density. We have noticed that P_t is better correlated with the curvature parameter $K_{\rm sym}(\rho)$ alone or with the linear combination of $L(\rho)$ and $K_{\rm sym}(\rho)$ at some sub-saturation density $\rho = 0.09$ fm^{-3}. However, such correlations show some degree of model dependence.

We have also investigated the dependence of core-crust transition properties on various symmetry energy elements using a single model. In this analysis, we have found that the transition density is strongly correlated with the values of the symmetry energy $S(\rho)$ calculated at the saturation density as well as those at $\rho = 0.1$ fm^{-3}. The transition pressure P_t is found to be correlated in a model independent manner only with the $S(\rho)$ at the $\rho = 0.1$fm^{-3}. Its correlation with the $S(\rho)$ at the saturation density is highly model dependent.

In chapter 4, the variations in the properties of neutron-stars due to the uncertainties in the density dependence of symmetry energy have been studied using two different families of the RMF models. Both the families of models include the contributions from the δ-mesons and cross-coupling of ρ-mesons with σ or ω-mesons in addition to several linear and non-linear interaction terms already present in the conventional RMF models. One of the families, F_ρ, include $\sigma - \rho$ cross-coupling, while, the other one, $F_{2\rho}$, includes $\omega - \rho$ cross-couplings. The several parameterizations for each of the families of the models are so obtained that they yield wide variations for the neutron-skin in the ^{208}Pb nucleus without affecting much the other bulk properties of the nuclei. we have studied the differences in the properties of neutron stars at fixed neutron skin thickness in ^{208}Pb, which are resulting from the differences in symmetry energy behavior across the models. The properties of neutron-stars considered are the core-crust transition density, mass, radius, redshifts, threshold mass required for the enhanced cooling through direct Urca process and the tidal polarizability parameter.

The properties of the neutron-stars at a fixed neutron-skin $\Delta r_{\rm np}$ in the ^{208}Pb nucleus are noticeably different for two different families of the models. These differences are pronounced at smaller values of $\Delta r_{\rm np}$. At $\Delta r_{\rm np} = 0.15$ fm, consistent with the experimental data on dipole polarizability, we get significant differences in the properties of neutron stars for the two families of models. The redshift and radius of canonical neutron star $(1.4 M_\odot)$ differ by about 10%. For the case of tidal polarizability and threshold mass required for the direct Urca process, these differences are about 40%. The core-crust transition properties also show reasonable differences across the different families of the models. These results thus indicate that the simultaneous inclusion of the $\sigma - \rho$ and $\omega - \rho$ cross-couplings terms in the isovector part of the effective Lagrangian density for the RMF model would enhance the flexibility of the model to accommodate the variations in the properties of the neutron-stars at a given neutron-skin thickness.

In chapter 5, we have studied the correlations of neutron star radii with several key parameters which govern the EoS of asymmetric nuclear matter. For this purpose, we have considered 18 RMF models, 24 Skyrme-type effective force and two microscopic models, all consistent with the current existing constraints coming from the neutron star mass measurement. For all the phenomenological models, both relativistic and non-relativistic, we have built unified EoSs for the inner-crust-core region to reduce the uncertainty in the radius due to inconsistent matchings between the core and the crust. We have shown that the radii of the low mass neutron stars are better correlated with the symmetry energy coefficient and its slope. As the neutron star mass increases, the correlations of radii with the iso-scalar parameters become stronger. For a given neutron star mass, the radii are somewhat strongly correlated with the slopes of the incompressibility and the symmetry energy coefficients relative to those with the incompressibility and the symmetry energy coefficients themselves. We also looked into the correlations of neutron star radii with the linear combination of K_0 and M_0 with L_0. The radii are better correlated with the linear combinations $K_0 + \alpha L_0$ and $M_0 + \beta L_0$ than those with the individual EoS parameters. In particular, noticeable improvement is seen in the correlations of radii with these linear combinations for the neutron star masses $\sim 1.4M_\odot$. Further, the correlations of radii with $M_0 + \beta L_0$ are stronger and practically independent of neutron star mass in the range 0.6-1.8$M_\odot$. The existence of these strong correlations can be linked to the empirical relation between the radius of neutron star and pressure P at a nucleonic density between 1-2 saturation density, and the dependence of P on EoS parameters K_0, M_0 and L_0. The range of values of M_0 and L_0 as deduced from the finite nuclei data lead to radii of a $1.4M_\odot$ neutron star to be in the range of 11.09-12.86 km.

In chapter 6, we have analyzed the spinodal instabilities and critical parameters of hot asymmetric nuclear matter using six different families of relativistic mean field models and two density dependent models. In particular, the sensitivity of the spinodal section and critical parameters on the density dependence of symmetry energy have been studied. We have considered six families of models constructed from three different base models whose parameters have been fitted to the groundstate properties of finite nuclei. The density dependence of the symmetry energy was varied by adding an extra non-linear cross-coupling term that couples the ρ-meson to the ω or the σ meson. Models with a symmetry energy slope between ~ 50 and 100 MeV have been generated.

As the temperature increases, the instability region decreases and matter become more symmetric inside the spinodal region. At a fixed temperature, the spinodal sections are also sensitive to the density dependence of symmetry energy of the model considered. We have noticed that at $T = 0$ the critical proton fraction increases when the slope L increases, and that form a given value L it almost does not depend on the model considered. However, this is not the case for finite temperature, and a spread on the proton fraction of 0.25 for $T = 14$ MeV was found when all set of models are considered, which implies the equation of state at finite temperature is not sufficiently constrained. . However, the critical density is found to be more constrained. At slope $L = 56$ MeV, the spread on the critical density increases from 0.006 fm^{-3} at $T = 0$ to $\sim$ 0.01 fm^{-3} at $T = 14$ MeV. These critical parameters are more sensitive to L_0 at relatively low temperature, which tend to wash out with increasing temperature. We have also discussed the behaviors of the distillation effect with temperature for some selected models under study. It is found that the models having smaller value of symmetry energy slope L_0 disfavor strong distillation effect. The dependency of distillation effects on the parameter L_0 decreases with increasing temperature, but the differences still noticeable for $F_{x\rho}$ families.

Bibliography

[1] N. K. Glendenning, *Compact stars: Nuclear physics, particle physics, and general relativity* (1997).

[2] P. Haensel, A. Y. Potekhin, D. G. Yakovlev, *Neutron stars 1: Equation of state and structure*, vol. 326 (Springer, New York, USA, 2007).

[3] N. K. Glendenning, S. A. Moszkowski, *Phys. Rev. Lett.* **67**, 2414 (1991).

[4] N. K. Glendenning, J. Schaffner-Bielich, *Phys. Rev. Lett.* **81**, 4564 (1998).

[5] B. D. Lackey, M. Nayyar, B. J. Owen, *Phys. Rev. D* **73**, 024021 (2006).

[6] H. J. Schulze, A. Polls, A. Ramos, I. Vidana, *Phys. Rev. C* **73**, 058801 (2006).

[7] J. M. Lattimer, M. Prakesh, *Phys. Rep.* **442**, 109 (2007).

[8] J. Schaffner-Bielich, A. Gal, *Phys. Rev.* **C62**, 034311 (2000).

[9] N. Chamel, P. Haensel, J. L. Zdunik, A. F. Fantina, *Int. J. Mod. Phys. E* **22**, 1330018 (2013).

[10] K. Kim, H. K. Lee, M. Rho, *Phys. Rev.* **C84**, 035810 (2011).

[11] S. Weissenborn, I. Sagert, G. Pagliara, M. Hempel, J. Schaffner-Bielich, *Astrophys. J.* **740**, L14 (2011).

[12] L. Bonanno, A. Sedrakian, *Astron. Astrophys.* **539**, A16 (2012).

[13] S. Weissenborn, D. Chatterjee, J. Schaffner-Bielich, *Phys. Rev. C* **85**, 065802 (2012).

[14] H. Chen, M. Baldo, G. F. Burgio, H. J. Schulze, *Phys. Rev.* **D86**, 045006 (2012).

[15] S. Schramm, V. Dexheimer, R. Negreiros, T. Schrhoff, J. Steinheimer, *Exciting Interdisciplinary Physics: Quarks and Gluons / Atomic Nuclei / Relativity and Cosmology / Biological Systems* (2013, arXiv:1202.5113 [astro-ph.SR]), pp. 323–332.

[16] D. L. Whittenbury, J. D. Carroll, A. W. Thomas, K. Tsushima, J. R. Stone (2012, arXiv:1204.2614 [nucl-th]).

[17] A. Sulaksono, B. K. Agrawal, *Nucl. Phys.* **A895**, 44 (2012).

[18] P. B. Demorest, T. Pennucci, S. M. Ransom, M. S. E. Roberts, J. W. T. Hessels, *Nature* **467**, 1081 (2010).

[19] J. Antoniadis, *et. al*, *Science* **340**, 448 (2013).

[20] J. M. Lattimer, M. Prakash, *Astrophys. J.* **550**, 426 (2001).

[21] J. M. Lattimer, M. Prakash, *Science* **304**, 536 (2004).

[22] F. J. Fattoyev, J. Piekarewicz, *Phys. Rev.* **C82**, 025810 (2010).

[23] F. J. Fattoyev, J. Carvajal, W. G. Newton, B.-A. Li, *Phys. Rev. C* **87**, 015806 (2013).

[24] N. Alam, B. K. Agrawal, J. N. De, S. K. Samaddar, G. Colò, *Phys. Rev. C* **90**, 054317 (2014).

[25] N. Alam, *et al.*, *Phys. Rev.* **C94**, 052801 (2016).

[26] L.-W. Chen, C. M. Ko, B.-A. Li, *Phys. Rev. C* **72**, 064309 (2005).

[27] M. Centelles, X. Roca-Maza, X. Viñas, M. Warda, *Phys. Rev. Lett.* **102**, 122502 (2009).

[28] I. Vidaña, C. Providência, A. Polls, A. Rios, *Phys. Rev. C* **80**, 045806 (2009).

[29] X. Roca-Maza, M. Centelles, X. Vinas, M. Warda, *Phys. Rev. Lett.* **106**, 252501 (2011).

[30] E. Khan, J. Margueron, I. Vidaña, *Phys. Rev. Lett.* **109**, 092501 (2012).

[31] E. Khan, J. Margueron, *Phys. Rev. C* **88**, 034319 (2013).

[32] F. J. Fattoyev, W. Newton, B.-A. Li, *Phys. Rev. C* **90**, 022801(R) (2014).

[33] M. Fortin, *et al.*, *Phys. Rev.* **C94**, 035804 (2016).

[34] A. Sulaksono, N. Alam, B. K. Agrawal, *Int. J. Mod. Phys.* **E23**, 1450072 (2014).

[35] R. Furnstahl, B. D. Serot, H.-B. Tang, *Nucl. Phys.* **A598**, 539 (1996).

[36] B. D. Serot, J. D. Walecka, *Int. J. Mod. Phys. E* **6**, 515 (1997).

[37] R. Furnstahl, B. D. Serot, H.-B. Tang, *Nucl. Phys.* **A615**, 441 (1997).

[38] N. Alam, A. Sulaksono, B. K. Agrawal, *Phys. Rev. C* **92**, 015804 (2015).

[39] N. Alam, H. Pais, C. Providência, B. K. Agrawal, *Phys. Rev. C* **95**, 055808 (2017).

[40] J. Chadwick, *Nature* **129**, 312 (1932).

[41] L. Rosenfeld, *Astrophysics and Gravitation, Proc. Solvay Conference on Physics, 16th (Univ. Bruxelles)* p. p. 174 (1974).

[42] W. Baade, F. Zwicky, *Proc. Nat. Acad. Sci.* **20**, 254 (1934).

[43] J. R. Oppenheimer, G. M. Volkoff, *Phys. Rev.* **55**, 374 (1939).

[44] A. Hewish, S. Bell, J. H. D. Pilkington, P. Scott, R. A. Collins, *Nature* **217**, 709 (1968).

[45] J. P. Blaizot, *Phys. Rep.* **64**, 171 (1980).

[46] J. P. Blaizot, J. F. Berger, J. Decharge, M. Girod, *Nucl. Phys.* **A591**, 435 (1995).

[47] P. Danielewicz, W. G. Lynch, R. Lacey, *Science* **298**, 1592 (2002).

[48] C. Fuchs, *Prog. Part. Nucl. Phys.* **56**, 1 (2006).

[49] A. F. Fantina, N. Chamel, J. M. Pearson, S. Goriely, *EPJ Web of Conferences* **66**, 07005 (2014).

[50] B.-A. Li, A. T. Sustich, M. Tilley, B. Zhang, *Nucl. Phys.* **A699**, 493 (2002).

[51] B.-A. Li, G.-C. Yong, W. Zuo, *Phys. Rev. C* **72**, 064611 (2005).

[52] Q. Li, *et al.*, *J. Phys. G: Nucl. Part. Phys.* **31**, 1359 (2005).

[53] G. Ferini, T. Gaitanos, M. Colonna, M. D. Toro, H. H. Wolter, *Phys. Rev. Lett.* **97**, 202301 (2006).

[54] G.-C. Yong, B.-A. Li, L.-W. Chen, *Phys. Lett.* **B650**, 344 (2007).

[55] L.-W. Chen, C. Ko, B.-A. Li, *Nucl. Phys.* **A729**, 809 (2003).

[56] G.-C. Yong, B.-A. Li, L.-W. Chen, X.-C. Zhang, *Phys. Rev. C* **80**, 044608 (2009).

[57] Q. Li, Z. Li, E. Zhao, R. K. Gupta, *Phys. Rev. C* **71**, 054907 (2005).

[58] W. Reisdorf, *et al.*, *Nucl. Phys.* **A781**, 459 (2007).

[59] B.-A. Li, C. B. Das, S. D. Gupta, C. Gale, *Nucl. Phys.* **2004**, 563 (A735).

[60] B.-A. Li, C. B. Das, S. D. Gupta, C. Gale, *Phys. Rev. C* **69**, 011603(R) (2004).

[61] Z. Xiao, B.-A. Li, L.-W. Chen, G.-C. Yong, M. Zhang, *Phys. Rev. Lett.* **102**, 062502 (2009).

[62] Z.-Q. Feng, G.-M. Jin, *Phys. Lett.* **B683**, 140 (2010).

[63] W.-J. Xie, J. Su, L. Zhu, F.-S. Zhang, *Phys. Lett.* **B718**, 1510 (2013).

[64] M. Centelles, X. Roca-Maza, X. Viñas, M. Warda, *Phys. Rev. C* **82**, 054314 (2010).

[65] X. Roca-Maza, X. Vinas, M. Centelles, P. Ring, P. Schuck, *Phys. Rev. C* **84**, 054309 (2011).

[66] F. Coester, S. Cohen, B. Day, C. M. Vincent, *Phys. Rev. C* **1**, 769 (1970).

[67] R. Furnstahl, J. J. Rusnak, B. D. Serot, *Nucl. Phys.* **A632**, 607 (1998).

[68] F. J. Fattoyev, J. Piekarewicz, *Phys. Rev. C* **86**, 015802 (2012).

[69] C. Ducoin, J. Margueron, C. Providência, *Europhysics Letters* **91**, 32001 (2010).

[70] C. Ducoin, J. Margueron, C. Providência, I. Vidaña, *Phys. Rev. C* **83**, 045801 (2011).

[71] C. J. Horowitz, J. Piekarewicz, *Phys. Rev. Lett.* **86**, 5647 (2001).

[72] G. Baym, C. Pethick, P. Sutherland, *Astrophys. J.* **170**, 299 (1971).

[73] G. Baym, H. A. Bethe, C. J. Pethick, *Nucl. Phys.* **A175**, 225 (1971).

[74] J. W. Negele, D. Vautherin, *Nucl. Phy.* **A207**, 298 (1973).

[75] A. Douchin, P. Haensel, *Astron. Astrophys.* **380**, 151 (2001).

[76] J. D. Walecka, *Ann. Phys. (N.Y.)* **83**, 491 (1974).

[77] J. Boguta, A. R. Bodmer, *Nucl. Phys.* **A292**, 413 (1977).

[78] B. D. Serot, J. D. Walecka, *Adv. Nucl. Phys.* **16**, 1 (1986).

[79] G. A. Lalazissis, J. König, P. Ring, *Phys. Rev. C* **55**, 540 (1997).

[80] H. Muller, B. D. Serot, *Nuclear Physics A* **606**, 508 (1996).

[81] R. Furnstahl, C. E. Price, G. E. Walker, *Phys. Rev. C.* **36**, 2590 (1987).

[82] Y. K. Gambhir, P. Ring, A. Thimet, *Ann. Phys.(N.Y.)* **198**, 132 (1990).

[83] T. H. R. Skyrme, *Phil. Mag.* **1**, 1043 (1956).

[84] D. Vautherin, D. M. Brink, *Phys. Rev. C* **5**, 626 (1972).

[85] E. Chabanat, P. Bonche, P. Haensel, J. Meyer, R. Schaeffer, *Nucl. Phys.* **A635**, 231 (1998).

[86] A. W. Steiner, M. Prakash, J. M. Lattimer, P. J. Ellis, *Phys. Rep.* **411**, 325 (2005).

[87] S. Kubis, *Phys. Rev.* **C70**, 065804 (2004).

[88] S. Kubis, *Phys. Rev.* **C76**, 025801 (2007).

[89] J. Carriere, C. Horowitz, J. Piekarewicz, *Astrophys. J.* **593**, 463 (2003).

[90] A. Sulaksono, T. Mart, *Phys. Rev.* **C74**, 045806 (2006).

[91] V. Baran, M. Colonna, M. D. Toro, A. Larionov, *Nuclear Physics A* **632**, 287 (1998).

[92] H. Müller, B. D. Serot, *Phys. Rev. C* **52**, 2072 (1995).

[93] S. S. Avancini, L. Brito, P. Chomaz, D. P. Menezes, C. Providencia, *Phys. Rev.* **C74**, 024317 (2006).

[94] M. Modell, R. C. Reid, *Thermodynamics and Its Applications,* (1983).

[95] J. M. Lattimer, Y. Lim, *Astrophys. J.* **771**, 51 (2013).

[96] R. Furnstahl, *Nucl. Phys.* **A706**, 85 (2002).

[97] M. Warda, X. Viñas, X. Roca-Maza, M. Centelles, *Phys. Rev. C* **80**, 024316 (2009).

[98] J. Piekarewicz, *et al.*, *Phys. Rev. C* **85**, 041302(R) (2012).

[99] B. K. Agrawal, J. N. De, S. K. Samaddar, *Phys. Rev. Lett.* **109**, 262501 (2012).

[100] X. Roca-Maza, *et al.*, *Phys. Rev. C* **87**, 034301 (2013).

[101] B. K. Agrawal, *Phys. Rev. C* **81**, 034323 (2010).

[102] S. K. Dhiman, R. Kumar, B. K. Agrawal, *Phys. Rev. C* **76**, 045801 (2007).

[103] A. Sulaksono, A. Kasmudin, *Phys. Rev.* **C80**, 054317 (2009).

[104] Kasmudin, A. Sulaksono, *Int. J. Mod. Phys.* **E20**, 1271 (2011).

[105] C. C. Moustakidis, T. Niksic, G. A. Lalazissis, D. Vretenar, P. Ring, *Phys. Rev.* **C81**, 065803 (2010).

[106] J. Xu, L.-W. Chen, B.-A. Li, H.-R. Ma, *Astrophys. J.* **697**, 1549 (2009).

[107] B. G. Todd-Rutel, J. Piekarewicz, *Phys. Rev. Lett* **95**, 122501 (2005).

[108] Y. Sugahara, H. Toki, *Nucl. Phys. A* **579**, 557 (1994).

[109] S. Typel, H. H. Wolter, *Nucl. Phys. A* **656**, 331 (1999).

[110] D. Vretenar, G. A. Lalazissis, T. Nikšić, P. Ring, *Eur. Phys. J.* **A 25**, 555 (2005).

[111] T. Bürvenich, D. G. Madland, J. A. Maruhn, P.-G. Reinhard, *Phys. Rev. C* **65**, 044308 (2002).

[112] M. D. Estal, M. Centelles, X. Viñas, S. K. Patra, *Phys. Rev. C* **63**, 024314 (2001).

[113] J. Erler, C. J. Horowitz, W. Nazarewicz, M. Rafalski, P.-G. Reinhard, *Phys. Rev. C* **87**, 044320 (2013).

[114] M. Dutra, *et al.*, *Phys. Rev. C* **85**, 035201 (2012).

[115] M. Dutra, *et al.*, *Phys. Rev. C* **90**, 055203 (2014).

[116] M. B. Tsang, *et al.*, *Phys. Rev. C* **86**, 015803 (2012).

[117] A. Tamii, *et al.*, *Phys. Rev. Lett.* **107**, 062502 (2011).

[118] C. M. Tarbert, D. P. Watts, D. I. Glazier, P. A. *et al*, *Phys. Rev. Lett.* **112**, 242502 (2014).

[119] S. Abrahamyan, et al., *Phys.Rev.Lett.* **108**, 112502 (2012).

[120] T. W. Donnelly, J. Dubach, I. Sick, *Nucl. Phys. A* **503**, 589 (1989).

[121] C. J. Horowitz, K. S. Kumar, R. Michaels, *Eur. Phys. J.* **A50**, 48 (2014).

[122] C. Mondal, *et al.*, *Phys. Rev.* **C93**, 064303 (2016).

[123] *http://hallaweb.jlab.org/parity/prex* (see section Status and Plans for latest updates).

[124] W. D. Myers, W. J. Swiatecki, *Nucl. Phys.* **A336**, 267 (1980).

[125] A. Sulaksono, T. J. Burvenich, P. G. Reinhard, J. A. Maruhn, *Phys. Rev. C* **79**, 044306 (2009).

[126] A. Sulaksono, T. Mart, T. J. Burvenich, J. A. Maruhn, *Phys. Rev. C* **76**, 041301 (2007).

[127] J. Piekarewicz, *Phys. Rev. C* **76**, 064310 (2007).

[128] S. B. Rüster, M. Hampel, J. Schaffner-Bielich, *Phys. Rev. C* **73**, 035804 (2006).

[129] S. Weinberg, *Gravitation and Cosmology* (Wiley, New York, 1972).

[130] J. M. Lattimer, C. J. Pethick, M. Prakash, P. Haensel, *Phys. Rev. Lett.* **66**, 2701 (1991).

[131] J. H. Taylor, J. M. Weisberg, *Astrophys. J.* **253**, 908 (1982).

[132] R. W. P. Drever, *Gravitational Radiation* (1983).

[133] K. Thorne, *THREE HUNDRED YEARS OF GRAVITATION* (1987).

[134] A. Brillet, *et al.* (Virgo Collaboration), *Technical Report No. VIR-0517A-15* (1989).

[135] J. Hough, *et al.*, *MPQ Technical Report No. 147 [GWD/137/JH(89)]* (1989).

[136] C. Cutler, *et al.*, *Phys. Rev. Lett.* **70**, 2984 (1993).

[137] B. Abbott, *et al.*, *Phys. Rev. Lett.* **119**, 161101 (2017).

[138] E. E. Flanagan, T. Hinderer, *Phys. Rev. D* **77**, 021502(R) (2008).

[139] T. Hinderer, *Astrophy. J.* **677**, 1216 (2008).

[140] T. Hinderer, B. D. Lackey, R. N. Lang, J. S. Read, *Phys. Rev. D* **81**, 123016 (2010).

[141] T. Damour, A. Nagar, L. Villain, *Phys Rev. D* **85**, 123007 (2012).

[142] G. Taranto, M. Baldo, G. F. Burgio, *Phys. Rev.* **C87**, 045803 (2013).

[143] A. Akmal, V. Pandharipande, D. Ravenhall, *Phys. Rev. C* **58**, 1804 (1998).

[144] W.-C. Chen, J. Piekarewicz **90**, 044305 (2014).

[145] H. Pais, C. Providência, *Phys. Rev. C* **94**, 015808 (2016).

[146] C. Providência, A. Rabhi, *Phys. Rev. C* **87**, 055801 (2013).

[147] S. Typel, G. Ropke, T. Klahn, D. Blaschke, H. H. Wolter, *Phys. Rev. C* **81**, 015803 (2010).

[148] T. Gaitanos, *et al.*, *Nucl. Phys.* **A732**, 24 (2004).

[149] T. Nikšić, D. Vretenar, P. Finelli, P. Ring, *Phys. Rev. C* **66**, 024306 (2002).

[150] G. A. Lalazissis, T. Nikšić, D. Vretenar, P. Ring, *Phys. Rev. C* **71**, 024312 (2005).

[151] H. Kohler, *Nuclear Physics A* **258**, 301 (1976).

[152] P. G. Reinhard, H. Flocard, *Nucl. Phys.* **A584**, 467 (1995).

[153] W. Nazarewicz, *et al.*, *Phys. Rev. C* **53**, 740 (1996).

[154] E. Chabanat, Ph.D. thesis, University Claude Bernard Lyon-1, Lyon, France (1995).

[155] E. Chabanat, P. Bonche, P. Haensel, J. Meyer, R. Schaeffer, *Nucl. Phys. A* **627**, 710 (1997).

[156] L. Bennour, P. Heenen, P. Bonche, J. Dobaczewski, H. Flocard, *Phys. Rev. C* **40**, 2834 (1989).

[157] P. G. Reinhard, *Nucl. Phys.* **A649**, 305c (1999).

[158] B. K. Agrawal, S. Shlomo, V. K. Au, *Phys. Rev. C* **72**, 014310 (2005).

[159] B. K. Agrawal, S. Shlomo, V. K. Au, *Phys. Rev. C* **68**, 031304(R) (2003).

[160] J. Friedrich, P.-G. Reinhard, *Phys. Rev. C* **33**, 335 (1986).

[161] S. Goriely, N. Chamel, J. M. Pearson, *Phys. Rev. C* **82**, 035804 (2010).

[162] S. Goriely, N. Chamel, J. M. Pearson, *Phys. Rev. C* **88**, 024308 (2013).

[163] D. Davesne, A. Pastore, J. Navarro, *Astron. Astrophys.* **585**, A83 (2016).

[164] F. Grill, H. Pais, C. Providência, I. Vidaña, S. S. Avancini, *Phys. Rev. C* **90**, 045803 (2014).

[165] F. Gulminelli, A. R. Raduta, *Phys. Rev. C* **92**, 055803 (2015).

[166] P. Haensel, J. L. Zdunik, J. Dobaczewski, *Astron. Astrophys.* **222**, 353 (1989).

[167] E. Fonseca, *et al.*, *Astrophys. J.* **832**, 167 (2016).

[168] J. M. Pearson, N. Chamel, A. F. Fantina, S. Goriely, *Eur. Phys. J.* **A50**, 43 (2014).

[169] S. Brandt, *Statistical and Computational Methods in Data Analysis* (Springer, New York, 3rd English edition, 1997).

[170] J. N. De, S. K. Samaddar, B. K. Agrawal, *Phys. Rev.* **C92**, 014304 (2015).

[171] L. Trippa, G. Colò, E. Vigezzi, *Phys. Rev. C* **77**, 061304(R) (2008).

[172] X. Roca-Maza, *et al.*, *Phys. Rev. C* **88**, 024316 (2013).

[173] A. Carbone, *et al.*, *Phys. Rev. C* **81**, 041301(R) (2010).

[174] L.-W. Chen, *Phys. Rev. C* **83**, 044308 (2011).

[175] T. Nikšić, D. Vretenar, P. Ring, *Phys. Rev. C* **78**, 034318 (2008).

[176] P. Zhao, Z. P. Lin, J. M. Yao, J. Meng, *Phys. Rev. C* **82**, 054319 (2010).

[177] A. W. Steiner, J. M. Lattimer, E. F. Brown, *Eur. Phys. J.* **A52**, 18 (2016).

[178] H.-T. Janka, K. Langanke, A. Marek, G. Martínez-Pinedo, B. Müller, *Phys. Rep.* **442**, 38 (2007).

[179] H.-T. Janka, *Ann. Rev. Nucl. Part. Sci.* **62**, 407 (2012).

[180] A. Burrows, *Rev. Mod. Phys.* **85**, 245 (2013).

[181] A. Mezzacappa, *Ann. Rev. Nucl. Part. Sci.* **55**, 467 (2005).

[182] J. Stone, P.-G. Reinhard, *Progress in Particle and Nuclear Physics* **58**, 587 (2007).

[183] M. Oertel, M. Hempel, T. Klähn, S. Typel, *Rev. Mod. Phys.* **89**, 015007 (2017).

[184] C. Horowitz, A. Schwenk, *Nuclear Physics A* **776**, 55 (2006).

[185] S. Heckel, P. P. Schneider, A. Sedrakian, *Phys. Rev. C* **80**, 015805 (2009).

[186] M. Ferreira, C. Providência, *Phys. Rev. C* **85**, 055811 (2012).

[187] S. S. Avancini, C. C. Barros, D. P. Menezes, C. Providência, *Phys. Rev. C* **82**, 025808 (2010).

[188] S. S. Avancini, *et al.*, *Phys. Rev. C* **85**, 035806 (2012).

[189] D. G. Ravenhall, C. J. Pethick, J. R. Wilson, *Phys. Rev. Lett.* **50**, 2066 (1983).

[190] C. J. Horowitz, M. A. Perez-Garcia, J. Piekarewicz, *Phys. Rev.* **C69**, 045804 (2004).

[191] T. Maruyama, T. Tatsumi, D. N. Voskresensky, T. Tanigawa, S. Chiba, *Phys. Rev.* **C72**, 015802 (2005).

[192] G. Watanabe, T. Maruyama, K. Sato, K. Yasuoka, T. Ebisuzaki, *Phys. Rev. Lett.* **94**, 031101 (2005).

[193] H. Pais, J. R. Stone, *Phys. Rev. Lett.* **109**, 151101 (2012).

[194] H. Pais, S. Chiacchiera, C. Providncia, *Phys. Rev.* **C91**, 055801 (2015).

[195] P. Haensel, *Acta Phys. Pol. B* **25**, 373 (1994).

[196] D. Page, S. Reddy, *Phys. Rev. Lett.* **111**, 241102 (2013).

[197] R. Williams, S. Koonin, *Nuclear Physics A* **435**, 844 (1985).

[198] S. Furusawa, H. Nagakura, K. Sumiyoshi, S. Yamada, *Astrophys. J.* **774**, 78 (2013).

[199] N. Buyukcizmeci, *et al.*, *Nuclear Physics A* **907**, 13 (2013).

[200] S. S. Avancini, S. Chiacchiera, D. P. Menezes, C. Providencia, *Phys. Rev.* **C82**, 055807 (2010).

[201] H. Pais, A. Sulaksono, B. K. Agrawal, C. Providncia, *Phys. Rev.* **C93**, 045802 (2016).

[202] J. B. Natowitz, *et al.*, *Phys. Rev. Lett.* **89**, 212701 (2002).

[203] V. A. Karnaukhov, *et al.*, *Phys. Rev.* **C67**, 011601 (2003).

[204] J. B. Elliott, P. T. Lake, L. G. Moretto, L. Phair, *Phys. Rev.* **C87**, 054622 (2013).

[205] V. A. Karnaukhov, *et al.*, *Phys. At. Nucl.* **60**, 1625 (1997).

[206] V. Karnaukhov, *et al.*, *Nuclear Physics A* **734**, 520 (2004).

[207] V. Karnaukhov, *et al.*, *Nuclear Physics A* **780**, 91 (2006).

[208] V. A. Karnaukhov, *et al.*, *Physics of Atomic Nuclei* **71**, 2067 (2009).

[209] O. Loureno, B. M. Santos, M. Dutra, A. Delfino, *Phys. Rev.* **C94**, 045207 (2016).

[210] K. Hebeler, J. M. Lattimer, C. J. Pethick, A. Schwenk, *The Astrophysical Journal* **773**, 11 (2013).

[211] S. Gandolfi, J. Carlson, S. Reddy, *Phys. Rev. C* **85**, 032801 (2012).

[212] K. Sumiyoshi, H. Kuwabara, H. Toki, *Nucl. Phys.* **A581**, 725 (1995).

[213] W. Lynch, *et al.*, *Prog. Part. Nucl. Phys.* **62**, 427 (2009).

[214] H. Pais, A. Santos, L. Brito, C. Providencia, *Phys. Rev.* **C82**, 025801 (2010).

[215] J. R. Stone, N. J. Stone, S. A. Moszkowski, *Phys. Rev.* **C89**, 044316 (2014).

[216] B. Jacquot, S. Ayik, P. Chomaz, M. Colonna, *Phys. Let. B* **383**, 247 (1996).

[217] R. Furnstahl, B. D. Serot, H. B. Tang, *Nucl. Phys. A* **640**, 505 (1998).